8-26-2009

Modeling and control of an automotive fuel cell thermal system

John Nolan

MODELING AND CONTROL OF AN AUTOMOTIVE FUEL CELL THERMAL SYSTEM

JOHN NOLAN

A thesis submitted to the Faculty of the Graduate School of the Rochester Institute of Technology in partial fulfillment of the requirements for the degree of

MASTER OF SCIENCE IN MECHANICAL ENGINEERING

Submitted: August 26, 2009

Department of Mechanical Engineering
Kate Gleason College of Engineering
Rochester Institute of Technology
Rochester, New York 14623

Thesis Committee Approval

Dr. Jason Kolodziej – *Thesis Advisor* _____
Department of Mechanical Engineering

Dr. Edward Hensel – *Department Head* _____
Department of Mechanical Engineering

Dr. Agamemnon Crassidis _____
Department of Mechanical Engineering

Dr. Tuhin Das _____
Department of Mechanical Engineering

Dr. Manish Sinha _____
General Motors Corporation

Abstract

This work develops an 8th order, non-linear thermal model of an automotive Proton Exchange Membrane (PEM) fuel cell system. Subsystem models were developed from first principals where ever possible and validated against data from a physical system. The entire model was then validated against system data from a General Motor's 120kW fuel cell system. The system model was analyzed in both the time and frequency domain. Next, a reduced, 3rd order model was constructed from the full model and then linearized. The performances of all three models were compared and it was found that the 3rd order linear model provided an acceptable representation of the full non-linear model.

Using the models developed in the first section, different control strategies were examined. A proportional-integral (PI) controller was developed as a baseline and compared to a full state feedback Linear Quadratic controller. This controller was augmented to include output variable feedback to improve the steady state performance of the controller. The state feedback controller was found to have faster response and less interaction between the controlled variables than the baseline controller. Because some of the states are unmeasured, an estimator was developed to determine the state values for the full state feedback controller.

Acknowledgements

I would like to thank my advisor, Dr. Jason Kolodjiez for his help with preparing this work. We began working on this project while colleagues at General Motor's Fuel Cell Research and Development Center and continued our collaboration after his move to RIT. He was instrumental in formulating the topic and helping guide my work. I would also like to thank all of my colleagues at GM who provided support and guidance and answered my seemingly endless requests for data. I would also like to thank the leadership at GM Fuel Cells for supporting me in obtaining my masters and for supporting this work.

A special thanks Dr. A Crassidis and Dr. Tuhin Das of RIT and Dr. Manish Sinha of GM for serving on my thesis committee.

Finally, I would like to thank my family and especially my wife, Lisa, for tolerating me during the year and a half I have been working on the project. It has required a lot of sacrifice, and I appreciate the support. Working on this project has been invaluable in my development as an engineer. What I have learned working on this project far exceeds any course work I could have taken and I appreciate their patience while I completed my thesis.

Table of Contents

List of Figures

List of Tables

List of Symbols

γ	Specific Heat Ratio of Air	*[]*
ε	Heat Exchanger Effectiveness	*[]*
λ	Cathode Stoichiometric Ratio	*[]*
η_{cp}	Compressor Efficiency	*[]*
ω_p	Coolant Pump Set Point	*rad/s*
c_p	Coolant Specific Heat	*J/kg*K*
G	Radiator Thermal Conductance	*W/K*
I_s	Stack Current	*A*
k	Bypass Valve Set Point	*%*
$\dot{m}_a$	Cathode Air Mass Flow Rate	*kg/s*
$\dot{m}_{bp}$	Bypass Coolant Mass Flow Rate	*kg/s*
$\dot{m}_{H2}$	Anode Hydrogen Mass Flow Rate	*kg/s*
$\dot{m}_r$	Radiator Coolant Mass Flow Rate	*kg/s*
$\dot{m}_s$	Stack Coolant Mass Flow Rate	*kg/s*
P_r	Compressor Pressure Ratio	*[]*
P_{req}	FCS Power Request	*kW*
$\dot{q}_{bp,s}$	Energy Transfer from Stack to Bypass	*J*
$\dot{q}_{bp,r}$	Energy Transfer from Radiator to Bypass	*J*
$\dot{q}_{r,i}$	Energy Transfer to Radiator	*J*
$\dot{q}_{r,o}$	Energy Transfer from Radiator	*J*
$\dot{q}_s$	Stack Heat Generation	*J*
$T_{a,o}$	Anode Heat Exchanger Coolant Outlet Temperature	*°C*
$T_{air,o}$	Compressor Air Outlet Temperature	*°C*
T_{amb}	Ambient Temperature	*°C*
$T_{c,o}$	Cathode Heat Exchanger Coolant Outlet Temperature	*°C*
$T_{H2,i}$	Anode Hydrogen Inlet Temperature	*°C*
$T_{m,o}$	Fluid Mixer Outlet Temperature	*°C*
$T_{r,i}$	Radiator Coolant Inlet Temperature	*°C*
$T_{r,o}$	Radiator Coolant Outlet Temperature	*°C*
$T_{r,w}$	Radiator Wall Temperature	*°C*
$T_{s,i}$	Stack Coolant Inlet Temperature	*°C*
$T_{s,o}$	Stack Coolant Outlet Temperature	*°C*
ΔT_s	Stack Coolant Temperature Difference	*°C*
V_{avg}	Stack Average Cell Voltage	*V*
v	Vehicle Velocity	*m/s*

Chapter 1 Introduction

As resources become increasingly scarce, government regulatory agencies and the public are demanding non-fossil fuel based transportation solutions. Automakers have responded by electrifying vehicles through the use of hybrid technologies, battery-electric vehicles (BEVs) and fuel cell vehicles. Hybrids, which combine a traditional internal combustion engine with electric motors and storage devices, are popular due to the fact that they return better gas mileage than non-hybrids and do not require any special infrastructure to operate. The downside to hybrids is that they still use fossil fuels and release CO_2. BEVs are emission free, but are hindered by the limited range of their battery packs. They also suffer from long recharge times and are thought to be a solution for intra-city transportation needs. Fuel cells, in contrast, combine the advantages of both BEVs and hybrids. A fuel cell vehicle does not use fossil fuels or release CO2, and can be refueled in the same manner as traditional internal combustion engines, negating the range issues associated with BEVs.

Of all the varieties of fuel cells, the Proton Exchange Membrane (PEM) fuel cell has shown the most promise for automotive applications based on their lower operating temperatures and fast start-up times. However, they are not without their challenges. In addition to requiring an entirely new hydrogen infrastructure to facilitate the refueling of PEM fuel cell vehicles, there are many technical challenges to integrating a fuel cell into an automobile. Along with the high cost of precious metals used as catalysis in the membranes and long-term durability of the fuel cell stack, there are several difficult controls challenges, including the thermal management. Precise thermal management of a PEM fuel cell system is critical for several reasons. If the internal temperature fuel cell stack rises to high, the membrane can suffer mechanical damage. Higher temperatures also result in faster catalyst degradation due to high platinum transport at elevated temperatures resulting in a loss of active area. (1) Additionally, the stack temperature has a large influence on the humidity control of the system. Humidification of the membrane is critical because proton conduction is directly proportional to the water content in the polymer electrolyte. (2) This conduction is the basis of a PEM fuel cell's operation. Without proton conduction, no power is produced and the fuel cell is of little use. However, too much water in the cell can lead to blocking of the electrolyte pores which results in flooding. It is therefore critical that a balance is struck between removing water produced by the reaction and

maintaining proper humidity of the electrolyte. An additional requirement is to minimize the thermal gradient between the inlet and outlet of the fuel cell stack. A large temperature gradient across the stack results in large relative humidity change between the inlet and outlet, which introduces mechanical stress into the membrane.

The two methods used for controlling the temperature of the fuel cell are air cooling and liquid cooling. For cells greater than 5 kW, liquid cooling is the preferred method. While air cooling is simpler, it becomes too hard to ensure the temperature is uniform within the cell. Also, water is a thermodynamically more efficient heat transfer medium than air. (2) There are also additional synergies between an internal combustion engines cooling system and a fuel cell's cooling system which makes liquid cooling the preferred method in automotive applications. In this work, the thermal system for a liquid cooled, automotive PEM fuel cell system (FCS) will be studied.

1.1 Literature Review

Before beginning this work, an extensive survey of the current literature was completed. For the modeling of an automotive style radiator, there are generally two types of models present in the literature. The first type is based on Kay's and London's (3) seminal work on compact heat exchangers. This type of model is generally only concerned with steady state calculations and not with the transient temperature dynamics. For example, Kroger (4) develops a graphical method to characterize the steady state performance of a radiator based on the core characteristics. Eichlseder (5) presents the results of a program developed to optimize the radiator fan size, but again only considers steady state operating conditions. The second type of model is the numerical model, which generally considers the temperature dynamics but are often much too computationally complex to be used for controls purposes. Bromnick (6) presents a model for an intercooler which focuses mainly on wave propagation and pressure effects but also considers the temperature effects as well. Their model is based on the effectiveness-NTU method, which is quasi-steady state. Based on the inlet mass flow rates, the effectiveness is computed and then from that and the inlet conditions, the outlet temperatures are computed. This is only valid for systems with small thermal masses, since it assumes instantaneous results. For a system with more thermal capacitance, this assumption does not hold. Jung and Assanis (7) develop a numerical model to quantify geometry changes on radiator performance. They

divide the heat exchanger into a mesh grid and use finite difference methods to compute the temperature changes throughout the heat exchanger. Thermal resistance is used to compute the heat transfer from the coolant to the heat exchanger wall to the air. While their model is very accurate, due to its high order it is computationally expensive and not well suited for control systems.

The cooling system found in this FCS, which uses a bypass valve and a variable flow coolant pump, has been studied recently for automotive internal combustion (IC) applications. Generally, the goal of this research is to reduce fuel consumption. For a survey of automotive thermal system components, Shah (8) provides a good overview along with recent developments for each component including radiators and charge air coolers. Allen and Lasecki (9) present a good overview of both traditional mechanical and advanced electromechanical coolant systems. They detail both the components of these advanced coolant systems and their benefits to the system. They also consider the need for this type of electromechanical coolant system in future powertrains, including fuel cells. Melzer, et al. (10) modified an existing vehicle's thermal system to include bypass valves in place of a thermostat and replaced the mechanical coolant pump with an electric unit and detailed the performance improvements. While they did not provide details on their control scheme, they did note up to 5% improved fuel economy along with faster warm-up times.

Cortona, et al. (11) present results from research similar to Melzer, however instead of modifying an existing vehicle and measuring the results they constructed a system model, developed their control system and then validated the results with actual hardware. The heat exchanger model developed is of particular interest because it is both low order and captures the temperature dynamics. Using a lumped capacitance assumption, they develop a non-linear, first order model based on the energy in the heat exchanger and the heat transfer between the coolant and the airflow. They also incorporate variable transport delays in their model based on the mass flow rate. The control strategy chosen was independent PI controls for both flow and bypass valve position with gain scheduling. They chose four specific operating regions and had different gains for each region. Cortona, et al. results were similar to Melzer's, in that they found reduced power consumption and a resultant increase in fuel economy along with faster warm-up times.

Cho, et al. (12) applied an electric coolant pump to a heavy duty truck using commercial modeling software, GTCool, and a PID controller for the coolant pump. They found a dramatic reduction in power consumption and were able to reduce radiator sizing 27% with the modified system. In Chanfreau, et al. (13) work on applying an electromechanical thermal system to a minivan as part of a 42V electrical system, they present an interesting control strategy. Using a three dimensional map of fan speed vs. coolant pump speed vs. radiator heat transfer, they designed the controller to minimize electrical power based on the cooling requirements. By including the fan in the controller, they were able to optimize power consumption in the system.

There has been great interest in fuel cells systems over the last decade, and as a result there is an extensive amount of research available in the literature. For the purpose of this research, the principal interests are with models of the fuel cell stack itself, thermal system modeling and the control of fuel cell systems. For an overview of fuel cells relating to automotive applications and the tradeoffs associated with the design of the thermal system, the reader is referred to Fronk, et al. (14). Amphlett, et al. (15) present one of the more widely cited stack models. First, they developed a steady state thermal energy balance for the stack based on the energy of each of the reactant streams, the energy produced from the electrochemical reaction and the heat loss from the stack to the surroundings. Heat transfer coefficients were experimentally determined and a transient model was developed from the steady state model by the addition of a lumped-capacitance accumulation term with good results. Lee and Lalk (16) reported on a modeling scheme devised specifically to assist with evaluating stack parameter changes. Their thermal calculations also use a similar energy balance around the stack, however they discritize the model and solve using finite difference methods. This numerical method is, however, not suited for controls analysis since it results in a higher order model. In contrast, Gurski (17) presents a dynamic stack model using the lumped capacitance assumption and finite difference methods. Gurski also uses Kroger's (4) method for the heat exchanger model used. The main goal of Gurski's work is to quantify the impact of low temperature operation and start-up conditions on efficiency and performance of the FCS. Gurski only controls bypass and fan speed and not the coolant pump.

Much of the research on stack models makes the simplifying assumption of either neglecting the thermal effects on the stack or assuming a constant temperature. Miotti, et al. (18) developed a controls orientated non-linear stack model to compare PI and feed forward control

of the air supply system. However, they neglect the thermal system, focusing only on the anode and cathode gas and humidity dynamics. They also assume the stack is isothermal to simplify the humidity calculations. Xue, et al. (19) developed a detailed model for a single cell stack, using control volumes and a lumped capacitance approach. They account for the effect of diffusion in the membrane, but only model the heat rejected by the exiting reactants and by convection from the fuel cell to the surroundings. While this is useful for looking at the temperature dynamics within one cell, it does not accurately reflect the dynamics of a larger, liquid cooled stack. Another detailed and well conceived cell model is presented by Baschuk and Li (20), but this model also does not accurately represent the temperature dynamics for a larger system.

Friedman, et al. (21) studied the increased power consumption that comes from designing each subsystem independently. They analyzed a FCS and optimized the airflow system considering the thermal system, which resulted in a decrease in parasitic power. However, they assumed a constant stack operating temperature and did not go into detail of their model development. Zhang, et al. (22) present the results of a thermal system model that consists of a fuel cell stack, coolant pump and heat exchanger but no bypass. The stack model from this work follows the well established transient lumped capacitance type, taking into account the heat generated by the chemical reaction in the stack. The heat exchanger model is formed similarly, using an energy balance with an accumulation term. It does not specify how the capacitance of the radiator is determined. The model is validated against data from a fuel cell city bus with good agreement. Most of the lumped capacitance, energy balance stack models specify that the stack thermal capacitance is the sum each of the stacks components mass and specific heat, for example, plates, membranes and end units. In practice, this is difficult to determine and Kolodziej (23) presents an empirical method to determine this value. Using temperature data from a fuel cell stack, an optimization routine is used to estimate the stack volume. This method results in a non-linear, first order model that is well suited to control design.

Many researchers have published work on the topic of control of FCS. Mays, et al. (24) detailed their work on developing a control system for an automotive FCS. Their controller design was done using a system model developed with proprietary internal software and was not detailed in their report. They discuss modeling hardware using frequency response techniques

and the supervisory control structure for the system. They mention using PI loops with feed foreword control along with feedback linearization, but they do not detail any of these methods.

The text by Pukrushpan, et al. (25) is an excellent resource for system modeling techniques and advanced control methods applied to a FCS. The text details the modeling and control of two systems; first, the air flow control of a FCS and second, the gas feed control in a fuel processor. For the first system, they develop a first principals model of the anode and cathode subsystems and of the fuel cell stack, which results in an 8^{th} order non-linear model. They then perform feedback linearization and compare a dynamic feed foreword controller with a state feedback LQR controller for a SISO control problem. For the second system, they again develop a system model for the fuel processor, resulting in a 10^{th} order non-linear model. Next, feedback linearization is again performed and decentralized PI control is compared to full state feedback LQR control for a MIMO control problem. While neither of these problems are concerned with the thermal system, the techniques and methods used are applicable to this author's research.

While not applied to a fuel cell thermal system, Bhut, et al. (26) present results from applying an adaptive control scheme to the radiator fan in an automotive thermal system. Using an on-line ARMA model estimator, model parameters are found and then a pole placement routine selects the controller parameters to achieve the desired closed-loop response. A standard PI controller is used during start-up to allow the adaptive controller's parameters to converge, and then the adaptive controller takes over. They found a 30% reduction in power consumption with this system compared to a traditional belt driven fan, along with the ability for the controller to account for system performance decreases over time. Another application of adaptive control is presented by Wendeker, et al. (27). In this work they apply an adaptive controller to the airflow control. A similar method is used for the adaptive controller, where a regressive model estimator is used to generate model parameters, from which the controller parameters are derived.

Golbert and Lewin (28) applied a non-linear model predictive controller to control power output. The stack model used in this research is the numerical type in which the heat transfer along the length of each plate is calculated based on the temperature between the plate, reactants and coolant. They develop a simplified, Amphlett CSTR type model and validate it against the

original model. This is the model used as the prediction model for the controller. They then formulate a cost function and optimize the cost function to determine the next controller output.

Ahn and Choe (1) presented interesting work that begins by developing a FCS system model. The system mechanization used is similar to that which is used in this research, however, Ahn and Choe lack an intercooler, anode heat exchanger and transport dynamics. They do include a coolant reservoir which is not present in the current system. The stack model used is the same first order, non-linear model mentioned in previous works cited (15) (22) (23). Two controllers are developed and compared in their performance to maintain the stack inlet and outlet temperature at a fixed value. Both a traditional PI controller and a state feedback LQR controller are presented. The full system model is second order, and due to the non-linearity of the stack model, the model is linearized at the operating point. Ahn and Choe found improved temperature control and reduced power consumption of coolant pump.

The basic control problem of this research is to control both the coolant pump and bypass valve to maintain the operating temperature of the fuel cell. Examples of this type of control problem can be found in the literature dealing with both fuel cell and internal combustion (IC) engines. In the case of IC engines, much effort has recently gone into advanced control strategies utilizing an electric water pump and a bypass valve or thermostat. The main goal of this type of development is to decouple the traditional link between engine speed and coolant pump speed found on a conventional belt-driven system. The benefits of an electric system include improved engine cooling performance, downsized components and reduced fuel consumption (10) (11) (13). While the application is different, the methodologies are similar to the fuel cell problem and are worth investigating.

The biggest difference between the IC engine control problem and the fuel cell control problem is that typically the IC engine does not involve set point tracking of the coolant temperature, due to the fact that the temperature set point is constant. As such, simple PI controllers are usually sufficient for the IC engine. The literature on coolant control of the fuel cell shows a greater range of control strategies. Peng et al. first use both static and dynamic feed forward controllers with PID feedback in the control of the air compressor, but found limited robustness and bandwidth with the system due to reliance on the feed forward path. They next implemented a LQR feedback controller with an observer to estimate the unmeasured states (25). This research was focused on the cathode air flow.

Mays et al. present a controller for automotive applications using a commercial software program, but do not provide much detail on the control strategy (24). Pukrushpan et al. provide an excellent description of MIMO control of a non-linear system, including linearization of the non-linear plant, but it is for the control of a reformer feeding the fuel cell (25). Ahn et al. presented in their research a very similar system and control strategy to what is proposed in this author's reaserch, but there are several key differences. They first developed a thermal system model and then compared both a PI controller with a feed forward term and an LQR controller using a linearized model to control both coolant flow and bypass set point (1). However, their system model was not entirely representative of actual thermal systems and while non-linear, was only second order. They included a coolant reservoir, while in a typical pressurized system, the reservoir is just an overflow container and its coolant volume is not circulated. Their control objectives were to control the coolant outlet temperature and the reservoir temperature, which is assumed to be the stack inlet temperature. In the system of concern for this research, there reservoir temperature is not valid, while the temperature difference across the stack is the second control requirement.

1.2 Scope of Work

This work will present an analysis of the thermal systems of a 120 kW automotive PEM fuel cell system. Chapter 2 presents the development of the system model. First, models are developed for each component in the thermal system. Next, the full, non-linear model is validated against data from a physical fuel cell system. A reduced order, non-linear model is developed and compared to the full, non-linear model. Finally, the reduced order, non-linear model is linearized at three operating points and compared back to the full, non-linear model.

Chapter 3 presents an analysis of several different control strategies for the control of the thermal system. Using the Relative Gain Array methodology, independent proportional-integral control is developed using an optimization routine to select the controller gains. Next, a Multi-Input, Multi-Output (MIMO) state feedback controller is developed using the linearized, reduced order model. The gains for the controller were selected using the Linear Quadratic Regulator (LQR) methodology. The state feedback controller was then augmented to include output variable feedback to improve the steady-state performance. Finally, a state estimator was developed to determine the unmeasured states for the state feedback controller. Chapter 4 presents conclusions and recommendations for future work.

Chapter 2 System Modeling

A typical fuel cell system for automotive applications is show in Figure 2-1 below and consists of three main subsystems. (29) The anode subsystem supplies compressed hydrogen from an onboard storage tank to the fuel cell stack. A pressure regulator is used to maintain the pressure inside of the stack. The anode heat exchanger helps warm the incoming hydrogen to the stack operating temperature. The recycle leg on the anode is used to both humidify the incoming hydrogen as well as increase the hydrogen utilization of the system by recirculating unconsumed hydrogen. Finally, there is a vent valve used to purge water and waste gas from the anode.

The cathode subsystem consists of a compressor to supply air to the stack. Air then flows through an intercooler to a water vapor transfer unit to humidify the inlet air stream using the wet cathode exhaust stream. There is also a bypass leg around the humidifier, used for both stack purges and to control inlet humidity. The thermal subsystem, which is the focus of this study, regulates the temperature of the stack.

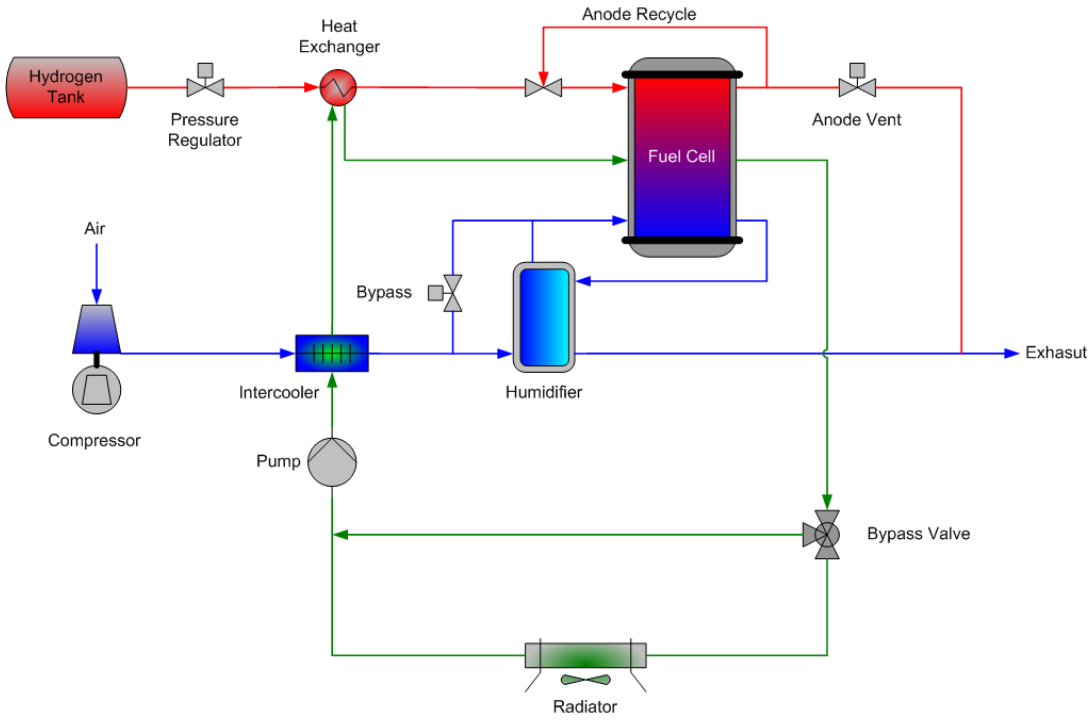

Figure 2-1 Typical Automotive Fuel Cell System Mechanization

The stack used throughout this research is a 440 cell stack with composite bipolar plates and an active area of 360 cm^2. The net power of the system is approximately 120 kW. This system is

typical of those found in automotive applications and is similar to the system found in General Motor's (GM) Equinox FC vehicle. (30) The figure below shows a detailed schematic of the thermal system under consideration, and is representative of a typical automotive fuel cell system.

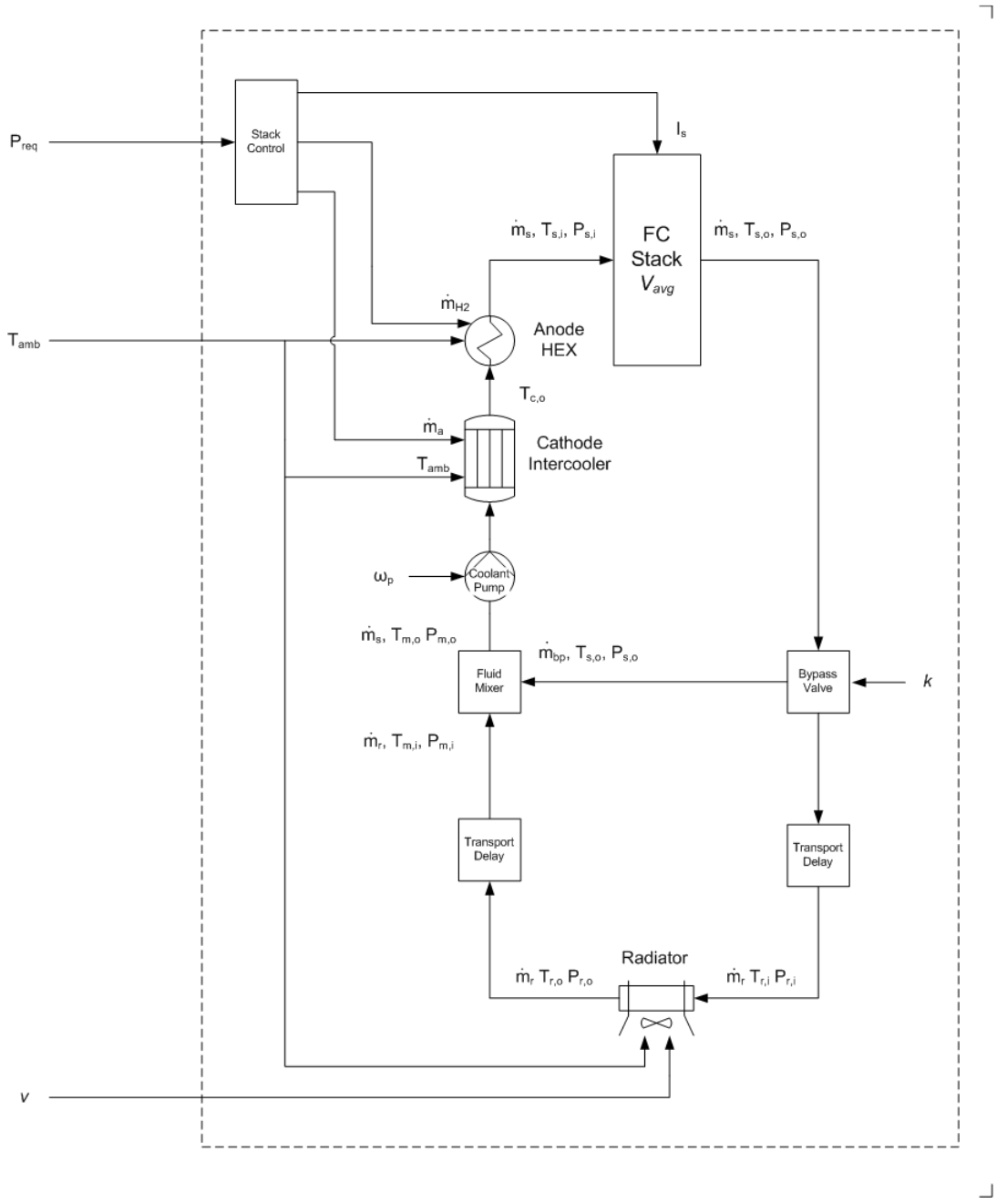

Figure 2-2 Fuel Cell Thermal System Diagram

Included in the diagram is the stack itself, a bypass valve to direct flow either to the heat exchanger or through a bypass leg, a pump and some transport dynamics to account for delays in the system. There are three heat exchangers in the thermal system, the main radiator for dissipating heat to the environment, an intercooler used to cool the incoming cathode air, and a smaller unit used to preheat the incoming hydrogen. The cathode air heat exchanger is needed due to the fact the temperature of the air exiting the compressor can be up to 50 °C above the stack operating temperature. The anode heat exchanger is needed to raise the temperature of the hydrogen, since the temperature is well below the stack operating temperature due to the adiabatic expansion of the gas through the pressure regulator. There are three external inputs that affect the thermal system; the system power request, ambient temperature and vehicle speed. Based on the power request, the stack current, air flow requirement and hydrogen flow requirements can be determined. These values affect the heat produced by the stack and the cooling loads caused by the anode and cathode heat exchangers. The ambient temperature primarily affects the performance of the radiator. Finally, the vehicle speed determines the airflow across the radiator which affects its performance. In the following sections, dynamic models of each component are developed and the model is validated against actual system data. From a system level perspective, Fronk et al (31) present a good overview of the tradeoffs associated with the design of a thermal system for an automotive fuel cell system.

2.1 Stack Model

The fuel cell stack is the main source of heat generation in the system. The stack is also the component whose temperature is being controlled, by the coolant outlet temperature measurement. There are many different stack thermal models, some of which were presented in Chapter 2. For this work, Kolodziej's (23) method is used. This method is similar to Amphlett's, (15) but uses a novel optimization technique to estimate the stack volume. The lumped-parameter method of Kolodziej's method is based on a continuously stirred tank reactor (CSTR) model, which is a non-linear, first order differential equation. Performing an energy balance around the stack:

$$\dot{q}_{store} = \dot{q}_{in} - \dot{q}_{out} + \dot{q}_{gen} \qquad [2.1]$$

where:

$$\dot{q}_{store} = \frac{d}{dt}\left(\rho V C_p T_{s,o}\right) \quad [2.2]$$

$$\dot{q}_{in} = \dot{m}_{s,i} C_p T_{s,i} \quad [2.3]$$

$$\dot{q}_{out} = \dot{m}_{s,o} C_p T_{ss,o} \quad [2.4]$$

Where $\dot{q}_{in}$ and $\dot{q}_{out}$ is the energy carried into and out of the stack by the coolant and $\dot{q}_{store}$ is the accumulation term. The term V in the store term is the effective volume, not the actual volume of the coolant in the stack. In much of the other literature, this storage term is actually a summation of the mass components, including the bipolar plates and end units. In this author's research, the estimated volume will be found to account for all of these masses in addition to the coolant volume. This simplifies the model to a first order equation suitable for mode-based controls applications since it reduces all of the accumulation terms down to a single value. Selecting a control volume around the stack allows the assumption that the mass flow in equals the mass flow out. Additionally, it is assumed that the specific heat of the coolant is constant, which results in Equation [2.5]:

$$\frac{d}{dt}\left(\rho V C_p T_{s,o}\right) = \dot{m}_c C_p \left(T_{s,i} - T_{s,o}\right) + \dot{q}_s \quad [2.5]$$

The generation term results from inefficiency within the stack in generating power due to activation overvoltage and ohmic losses. These losses can be estimated by (2):

$$\dot{q}_s = \left(1.25 - V_{avg}\right) * n * I_s \quad [2.6]$$

where V_{avg} is the average cell voltage, *n* is the number of cells in the stack and I_s is the stack current and 1.25 is the maximum open circuit voltage of the cell without any losses. This is derived from the Gibb's free energy of the reversible reaction between the hydrogen and the air in the cell. However, due to the activation, ohmic and mass transport losses within the membrane, the actual voltage in the cell will be less than the reversible, ideal voltage. That difference manifests itself as heat generated within the cell. This heat needs to be rejected to

keep the cell at a desired temperature. Combining equations yields the first-order, nonlinear stack model:

$$\frac{d}{dt}\left(\rho V C_p T_{s,o)}\right) = \dot{m}_s C_p\left(T_{s,i} - T_{s,o}\right) + \left(1.25 - V_{avg}\right) * n * I_s \qquad [2.7]$$

Talking the coolant density and estimated volume to be constant, Equation [2.7] reduces to:

$$\dot{T}_{s,o} = \frac{\dot{m}_c}{\rho V}\left(T_{s,i} - T_{s,o}\right) + \frac{1}{\rho V C_p}\left(1.25 - V_{avg}\right) * n * I_s \qquad [2.8]$$

To estimate the effective stack volume, an optimization routine was devised. Using coolant data from a fuel cell stack, a sweep of effective volumes was simulated against the actual data and the fit of the data was evaluated using a mean squared error algorithm. The effective volume was varied from 1 to 20 liters. Figures 2-3, 2-4 and 2-5 show the data used for the optimization while Figure 2-6 illustrates the result from the optimization. Transient temperature data was used since the effective volume acts as a thermal capacitance to changes in temperature.

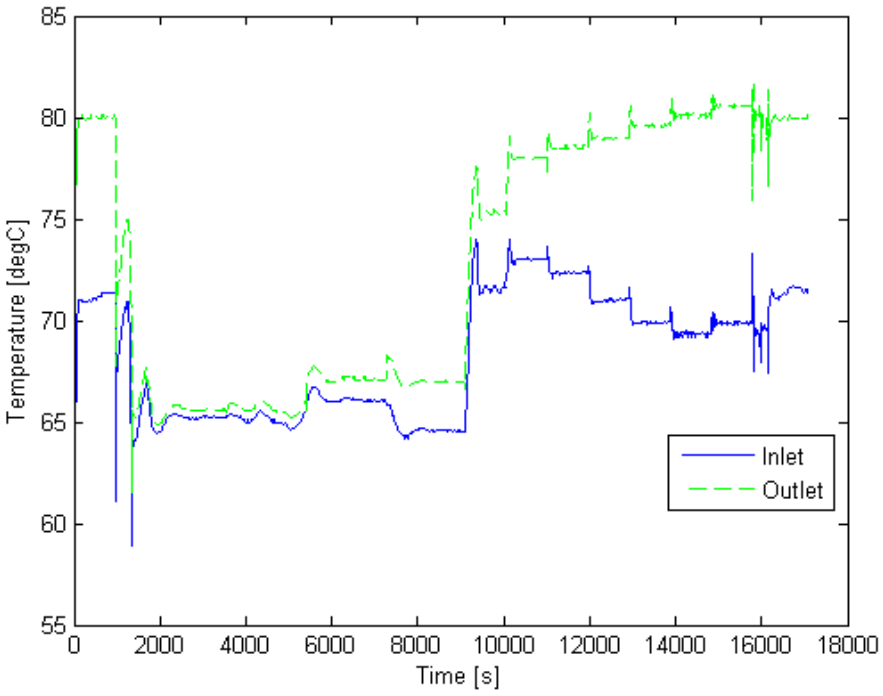

Figure 2-3 Coolant Temperature Data for Volume Optimization

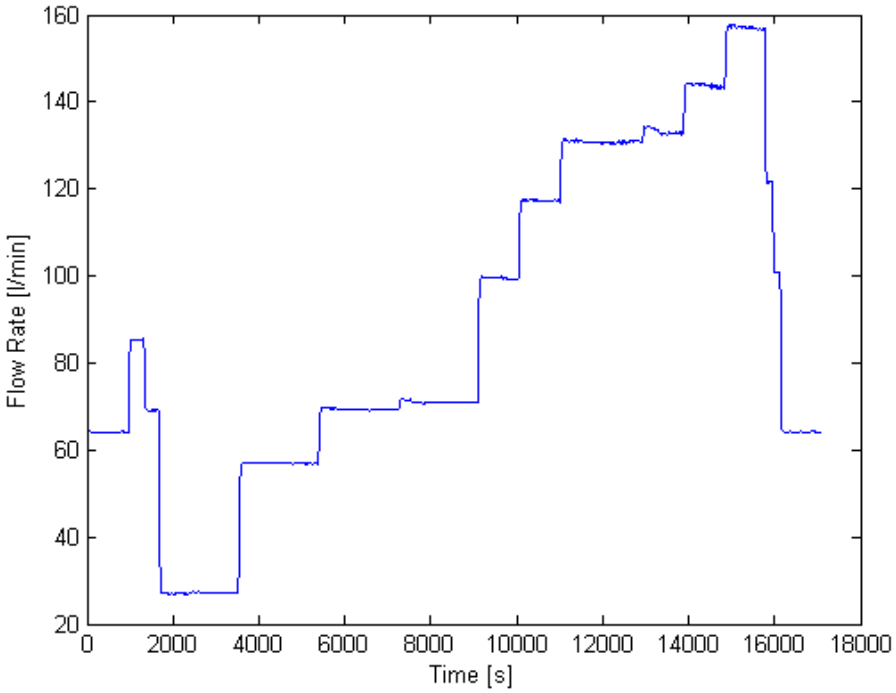

Figure 2-4 Coolant Flow Data for Volume Optimization

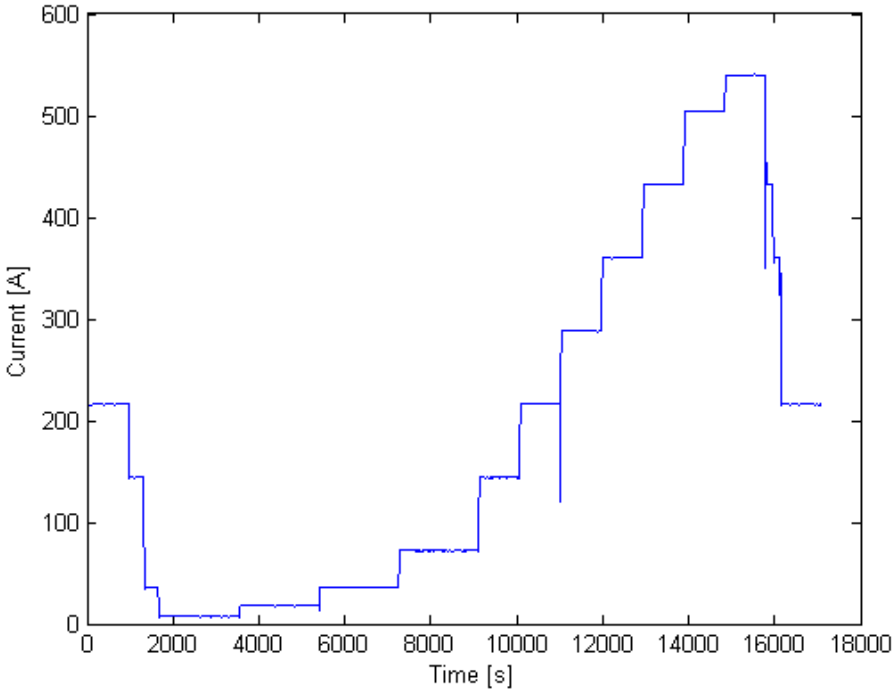

Figure 2-5 Load Profile for Volume Optimization

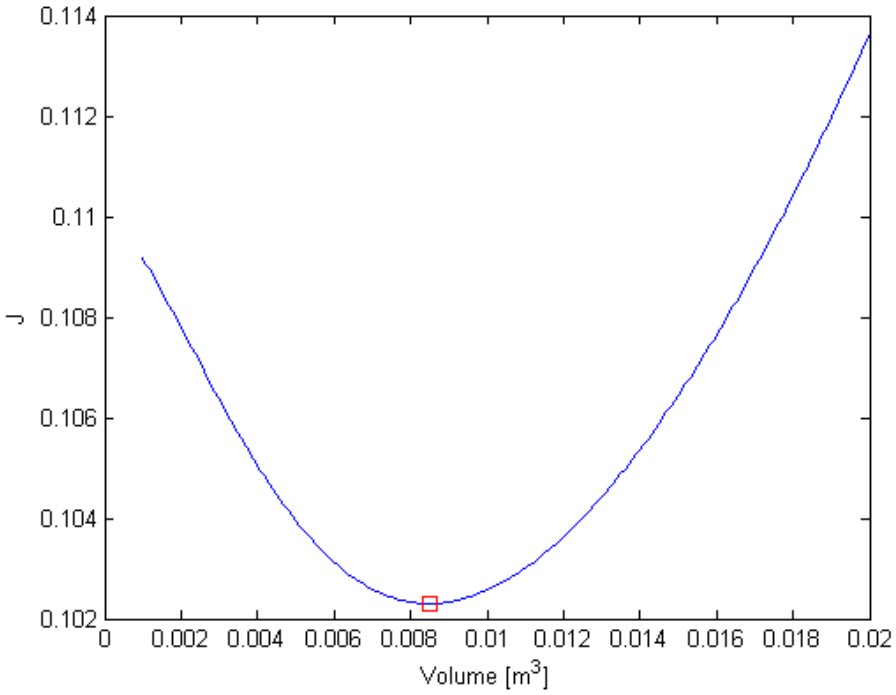

Figure 2-6 Volume Optimization Results

The minimum value of the function was at an effective volume of 8.5 liters, which is larger than the actual coolant volume. This is to be expected since this effective volume takes into consideration the volume of the coolant along with the mass of the bipolar plates and end units. To verify the effective volume, the stack model was simulated against system data. The fit of the model using the effective volume is quite good, as shown in Figure 2-7 which compares the actual and simulated stack outlet temperatures. While there is some steady state error in the simulated temperature, the transient sections of the data match very well, as shown in Figure 2-8. Since the transient response is the focus of the model, the small steady-state error can be accepted. The normalized Root Mean Squared Error, *RMSEn*, is used to evaluate the model fit, with 0 indicating a perfect fit.

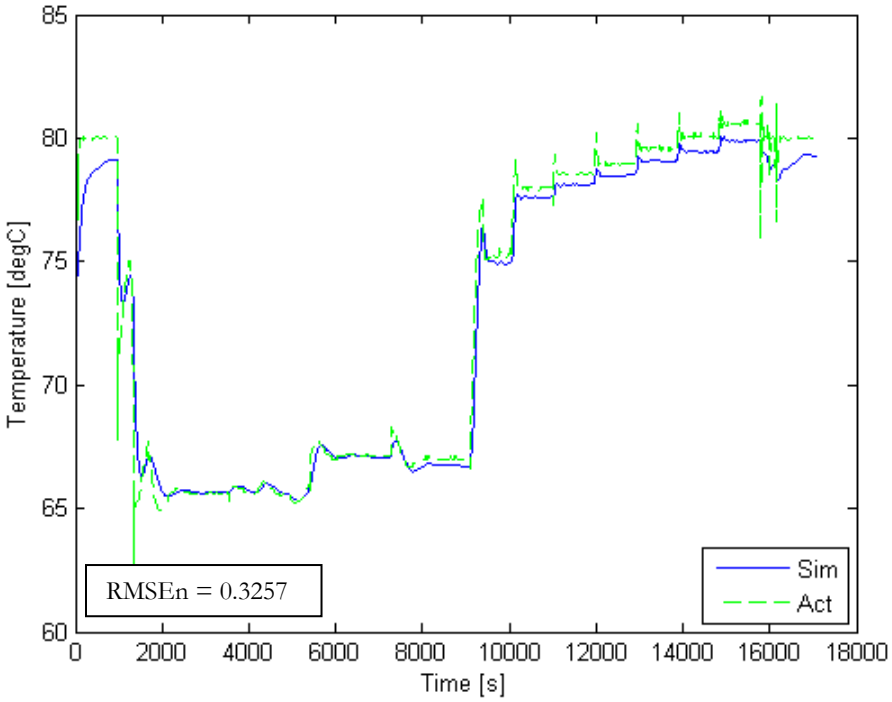

Figure 2-7 Simulated and Actual Stack Coolant Outlet Temperature

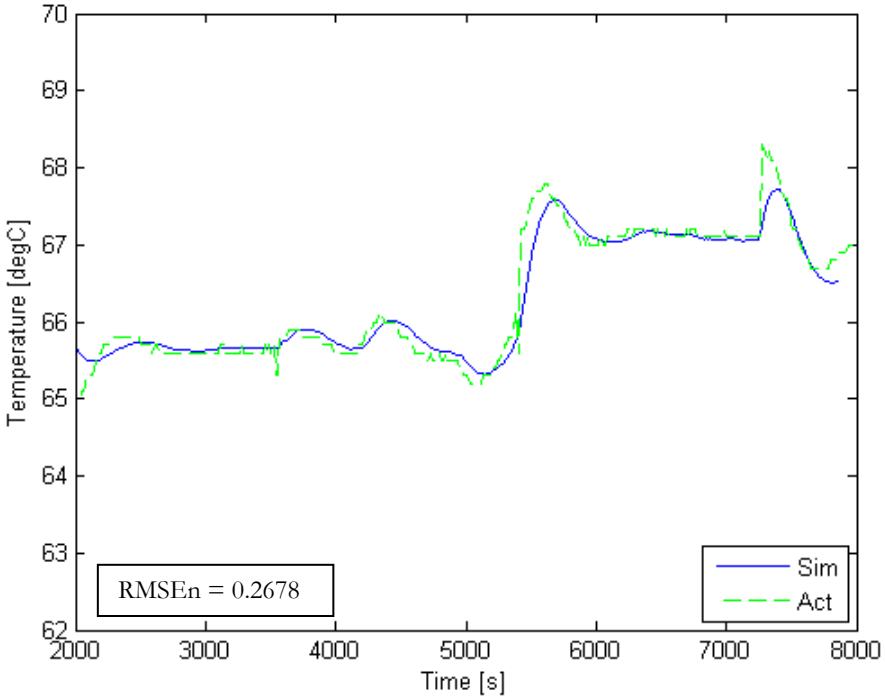

Figure 2-8 Simulated and Actual Stack Coolant Outlet Temperature, Transient

2.2 Bypass Valve

The bypass valve is used to control the flow of coolant between the heat exchanger and the bypass leg. Since the response of the valve is much faster than the temperature dynamics of the system, the dynamic response of the valve is ignored and the valve is considered ideal. The flow through the valve is treated as a linear function of the valve command, with a 0% command, *k*, indicating all flow goes to the heat exchanger and a 100% command indicating all flow is through the bypass. Equations [2.9] and [2.10] model the coolant flow distribution:

$$\dot{m}_{bp} = \dot{m}_s(\frac{k}{100}) \quad [2.9]$$

$$\dot{m}_r = \dot{m}_s(1 - \frac{k}{100}) \quad [2.10]$$

where $\dot{m}_{bp}$ is the flow through the bypass leg and $\dot{m}_r$ is the flow through the radiator.

2.3 Radiator

The radiator used in this system is a standard automotive style heat exchanger. It's main function is to dissipate waste heat to the environment. The model for the radiator is a second order, lumped capacitance model with some experimentally derived factors. The model consists of three parts. The first part describes the steady-state heat transfer between the air and the coolant as a function of ambient temperature, air mass flow, coolant flow and coolant inlet temperature using an experimentally derived Q_{ITD} look-up table. This table estimates the heat transfer based on the inlet temperature difference. The data for this table was obtained from experiential measurements of the GM fuel cell system. The second part of the model is a standard dynamic lumped capacitance model that describes the dynamics between the coolant, the radiator, and the environment. Using an energy balance around the radiator and adding an accumulation term, we have:

$$\dot{q}_{store} = \dot{q}_{in} - \dot{q}_{out} + \dot{q}_{Thermal} \quad [2.11]$$

with

$$\dot{q}_{store} = \frac{d}{dt}\left(\rho V c_p T_{r,o}\right) \quad [2.12]$$

$$\dot{q}_{in} = \dot{m}_{r,i} c_p T_{r,i} \quad [2.13]$$

$$\dot{q}_{out} = \dot{m}_{r,o} c_p T_{r,o} \quad [2.14]$$

Where $\dot{q}_{in}$ and $\dot{q}_{out}$ is the energy carried into and out of the radiator by the coolant and $\dot{q}_{store}$ is the accumulation term. The $\dot{q}_{Thermal}$term describes the heat transfer between the coolant and the thermal mass of the radiator itself.

$$\dot{q}_{Themal} = G(T_{r,w} - T_{r,o}) \quad [2.15]$$

The coefficient G represents the thermal conductance of the radiator and has units of W/K. This parameter is determined experimentally from test data. Combining equations and assuming that the specific heat is constant and selecting a control volume around the radiator yields:

$$\frac{d}{dt}(\rho V c_p T_{r,o}) = \dot{m}_r c_p\left(T_{r,i} - T_{r,o}\right) + G(T_{r,w} - T_{r,o}) \quad [2.16]$$

Defining the heat capacity $C = \rho V c_p$ and taking that term to be a constant further simplifies Equation [2.16] to be:

$$\dot{T}_{r,o} = \frac{\dot{m}_r c_p}{C}\left(T_{r,i} - T_{r,o}\right) + \frac{G}{C}(T_{r,w} - T_{r,o}) \quad [2.17]$$

Equation [2.17] is the final dynamic equation for the coolant outlet temperature of the radiator. The third part represents the heat capacity of the thermal mass of the radiator. It is a function of the heat transfer between the coolant and the environment and the heat transfer between the coolant and the radiator. Taking an energy balance around the mass of the radiator:

$$\dot{q}_r = \dot{q}_{r,i} - \dot{q}_{r,o} \quad [2.18]$$

with

$$\dot{q}_r = \frac{d}{dt}\left(\rho V c_p T_{r,o}\right) \quad [2.19]$$

Here $\dot{q}_{r,i}$ is the heat transfer from the coolant to the radiator and $\dot{q}_{r,o}$ is the heat transfer to the environment from the Q_{ITD} table.

$$\dot{T}_{r,w} = G\left(T_{r,o} - T_{r,w}\right) + cf_{QITD}\left(T_{r,i} - T_{amb}\right) \quad [2.20]$$

Taken together, Equations [2.17] and [2.20] describe the dynamics of the radiator.

2.4 Transport Delays

Due to the length of plumbing between the stack, the bypass valve and the pump to the heat exchanger, it is necessary to include some transport dynamics in the system model to account for the delay in the temperature response. Neglecting any heat loss in the plumbing and only considering the lag of the temperature, a pure time delay can be used. The delay is a function of the plumbing length and the flow of the coolant.

$$\theta = \frac{V}{v} \quad [2.21]$$

Where θ is the delay, V is the volume of the plumbing and v is the volumetric flow rate of the coolant. Using a 1/1 Pade approximation allows us to model this delay in transfer function form (32):

[2.22]

$$G(s) = \frac{1 - \frac{\theta}{2}s}{1 + \frac{\theta}{2}s}$$

In this model, there are two transport delay terms; one for the plumbing from the bypass valve to the radiator and the second from the radiator back to the fluid mixer. It is important to include these delays in the system model because they will have a significant impact on the controller performance, since the delay is not constant. With a fixed volume, low coolant flows will result in a larger delay than high coolant flows. From measurements from the physical system, the piping leading to the radiator has an approximate volume of 0.5 liters. The piping leading from the radiator has an approximate volume of 0.6 liters.

2.5 Fluid Mixer

The fluid mixer is the connector where the bypass leg and the heat exchanger leg join together before going to the pump. Physically, the mixer is nothing more than a T junction, but dynamically it is where the two fluid streams join and mix. To model this component, an energy balance is performed around the component.

$$\dot{q}_{out} = \dot{q}_{bp,s} + \dot{q}_{bp,r} \quad [2.23]$$

$$\dot{q}_{out} = \dot{m}_s c_p T_{m,o} \quad [2.24]$$

$$\dot{q}_{bp,s} = \dot{m}_{by} c_p T_{s,o} \quad [2.25]$$

$$\dot{q}_{bp,r} = \dot{m}_r c_p T_{r,o} \quad [2.26]$$

Taking a control volume around the mixer and assuming specific heat is constant, than Equation [2.23] can be simplified:

$$\dot{m}_{p,i} = \dot{m}_{bp} + \dot{m}_r \quad [2.27]$$

[2.28]

$$T_{m,o} = \frac{\dot{m}_{mp} T_{s,o} + \dot{m}_r T_{r,o}}{\dot{m}_{bp} + \dot{m}_r}$$

Equation [2.28] represents the outlet temperature of the fluid mixer in terms of the temperature and flow of each incoming coolant stream.

2.6 Coolant Pump

The coolant pump provides the flow in the system. A normal pump model would yield the coolant flow rate as a function of the up and down stream pressure of the pump based on the pump's characteristic curve. However, in this analysis, the pressure drops through the system are not modeled, so a different approach is needed. Since this is a closed system, it is possible to take advantage of this fact and base the model on system performance data. The two critical parameters of interest in the pump model are the time rate of change of flow to changes in the pump set point and also the typical flow rate of the pump for various set points. Both of these responses can be obtained by examining data from the actual system. Looking at step response data of the pump, a first order plus dead time characteristic response is observed. In transfer function form, this is represented as:

$$G_{pump} = \frac{Flow}{Speed} = \frac{Ke^{\theta s}}{\tau s + 1} \qquad [2.29]$$

where K is the gain, θ is the time delay and τ is the system time constant. Looking at several different step changes, and applying system identification techniques, these system parameters can be estimated. From the data in Figure 2-9 below, an estimated time constant, τ, of was selected of 1.35 sec using graphical methods (32). In a similar manner, the gain K was found to be 1.96. Finally, the dead time is easy to determine from inspection, and was found to be 2.0 sec.

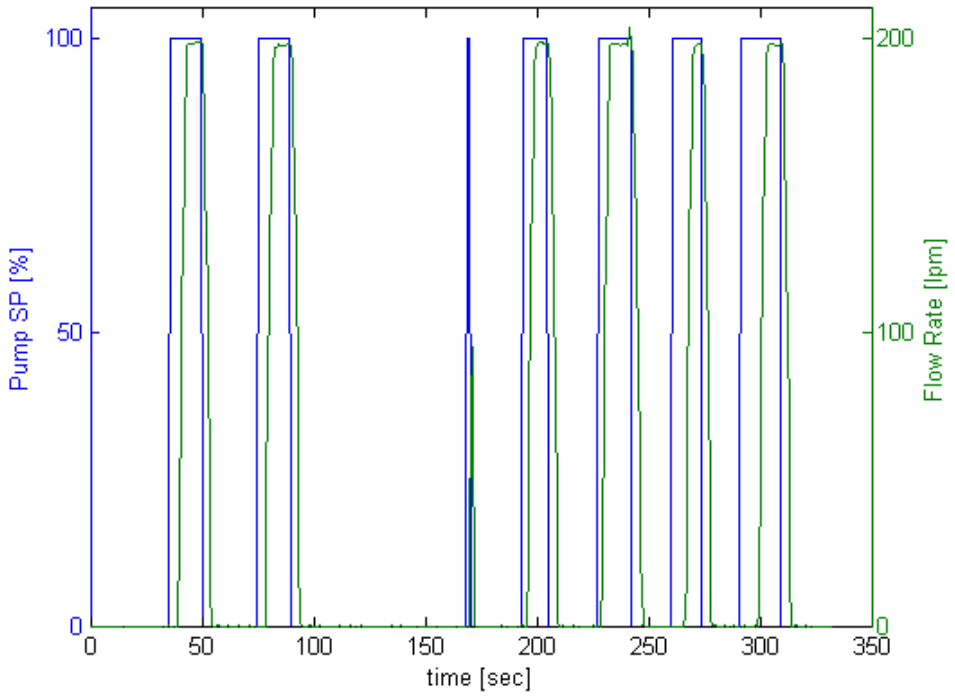

Figure 2-9 Pump Response Data

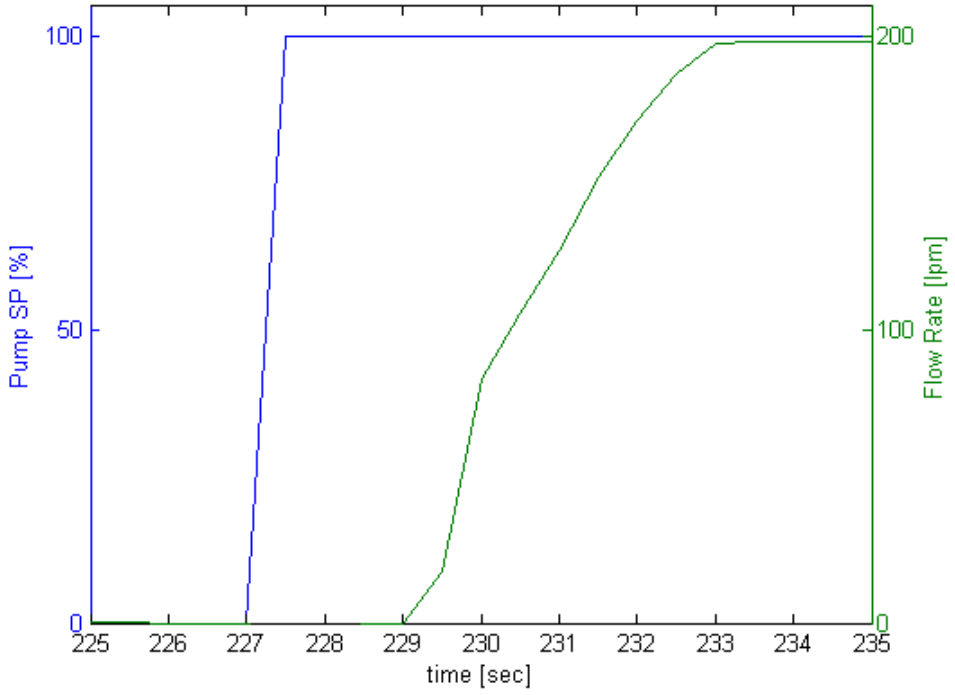

Figure 2-10 Pump Step Response

Admittedly, this method has some drawbacks, namely, it relies on system data to develop the model, so it is not useful for evaluating changes to the system's hardware. Additionally, the flow rate is only an approximation based on data, so fluctuations in system pressure that effect the coolant flow will not be captured. However, for the purpose of this research, these are acceptable trade-offs. Since the main goal is to evaluate the relative effectiveness of various coolant control schemes, exact representation of the pump dynamics is not critical. As long as the delay in flow changes due to a change in set point are modeled, the model serves its purpose. Pressure drop through the system is not the main concern, only the control of coolant flow and temperature. Figure 2-11 below shows a comparison between the actual flow feedback and the model flow feedback. From this figure it is apparent the model provides an acceptable representation of the actual system.

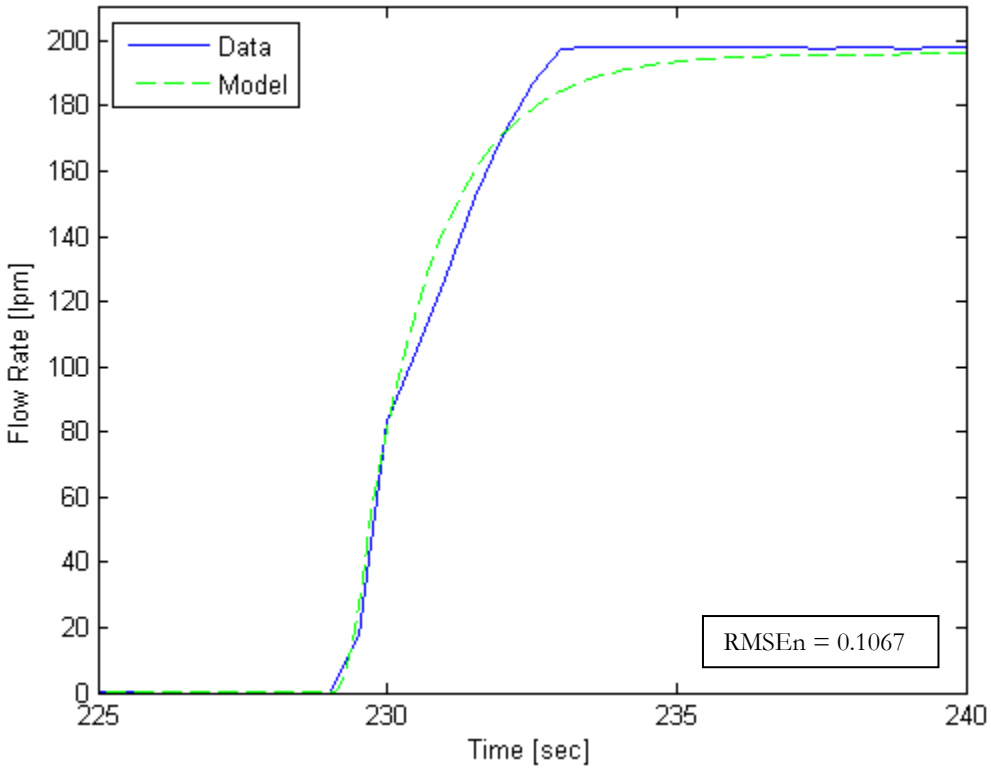

Figure 2-11 Coolant Pump Model Comparison

2.7 Cathode Intercooler

In the cathode subsystem, air is compressed and fed into the fuel cell using a compressor, which, by its nature, causes a temperature rise in the air. To lower the temperature of the incoming air to the stack operating condition of approximately 80 °C, the air passes through an air to water intercooler which uses the coolant on the water side. The effect on the coolant is a function of the air flow, which results from the power request of the system. The cathode flow required for the stack can be determined by the oxygen consumption (2):

$$\dot{m}_{O2} = \frac{I_s n}{4F} \qquad [2.30]$$

where I_s is the stack current, n is the number of cells and F is Faraday's constant. This equation gives the mass flow requirement in moles per second. Using the molar mass of oxygen, the equation can be represented in kg/s as:

$$\dot{m}_{O2} = 8.29x10^{-8} I_s n \qquad [2.31]$$

Since the oxygen is delivered as air, it needs to be converted to an air basis. Assuming the oxygen content of air is 21%, Equation [2.31] is converted to the air mass flow rate:

$$\dot{m}_a = 3.57x10^{-7} \lambda I_s n \qquad [2.32]$$

The stoichiometric ratio, λ, is included. For a ratio of 1, the exact amount of oxygen needed for the reaction is supplied to the stack, with no oxygen in the outlet stream. This is not practical because localized starvation can occur, which damages the membrane. More often, a ratio of 2 or higher is used (2). The temperature rise due to the compressor can be computed from (25):

$$T_{air,o} = T_{amb} + \frac{T_{amb}}{\eta_{cp}} \left(P_r^{\frac{\gamma-1}{\gamma}} - 1 \right) \qquad [2.33]$$

Where γ is the specific heat ratio, which is 1.4 for air, η_{cp} is the compressor efficiency, and P_r is the pressure ratio for the given mass flow. Using the compressor map supplied by the compressor manufacturer, look-up tables for efficiency and the pressure ratio can be constructed versus mass flow. From this data, Figure 2-12 shows the relationship between the stack current and inlet temperature, assuming an ambient temperature of 25 °C and a λ of 2. The unusual shape of the response is a function of the changing compressor efficiency at different flow rates and pressure ratios. As shown in the figure, at low loads the intercooler must supply heat to the incoming air to bring it up to stack operating temperature, and at high loads heat must be removed to bring the incoming air down to approximately 80 °C.

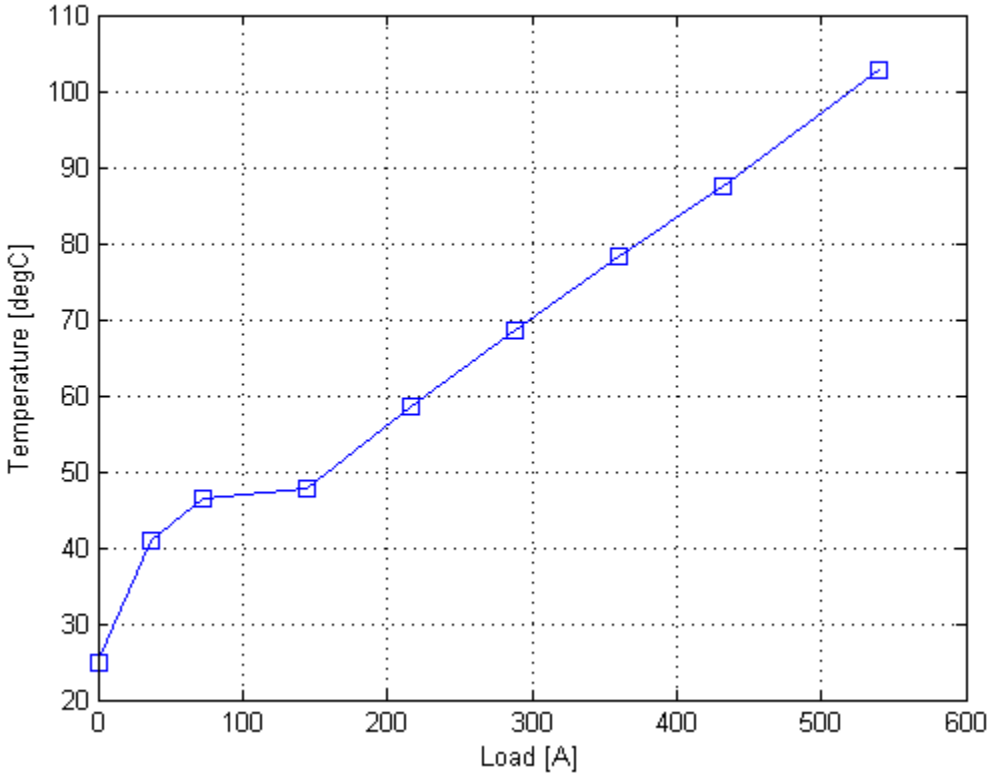

Figure 2-12 Compressor Outlet Temperature as a Function of Load

The temperature dynamics of the heat exchanger were modeled in a similar fashion to the stack thermal model. Performing an energy balance around the heat exchanger:

$$\dot{q}_{store} = \dot{q}_{in} - \dot{q}_{out} + \dot{q}_c \qquad [2.34]$$

where

$$\dot{q}_{store} = \frac{d}{dt}\left(\rho V c_p T_{c,o}\right) \quad [2.35]$$

$$\dot{q}_{in} = \dot{m}_s c_p T_{m,o} \quad [2.36]$$

$$\dot{q}_{out} = \dot{m}_s c_p T_{c,o} \quad [2.37]$$

Where $\dot{q}_{in}$ and $\dot{q}_{out}$ is the energy carried into and out of the heat exchanger by the coolant and $\dot{q}_{store}$ is the accumulation term. Assumed that the specific heat of the coolant is constant, and taking a control volume around the heat exchanger, Equation [2.35] becomes:

$$\frac{d}{dt}\left(\rho V c_p T_{c,o)}\right) = \dot{m}_s c_p \left(T_{m,o} - T_{c,o}\right) + \dot{q}_c \quad [2.38]$$

The generation term here is used to represent the heat transfer from the incoming air to the coolant. From the compressor outlet temperature and the coolant inlet temperature, the amount of energy transfer to the coolant can be estimated (33):

$$\dot{q}_c = \varepsilon \dot{m}_a c_{p,air}\left(T_{air,o} - T_{m,o}\right) \quad [2.39]$$

Where ε is the effectiveness of the heat exchanger. From an analysis of the heat exchanger provided by the manufacturer, the effectiveness can be reasonably approximated as 1 for all operating conditions. Combining Equations [2.38] and [2.39] yields the first-order, nonlinear heat exchanger model:

$$\frac{d}{dt}\left(\rho V c_p T_{c,o)}\right) = \dot{m}_s c_p \left(T_{m,o} - T_{c,o}\right) + \dot{m}_a c_{p,air}\left(T_{air,o} - T_{m,o}\right) \quad [2.40]$$

Taking the coolant density and coolant volume to be constant, Equation [2.40] reduces to:

$$\dot{T}_{c,o} = \frac{\dot{m}_s}{\rho V}\left(T_{m,o} - T_{c,o}\right) + \frac{\dot{m}_a c_{p,air}}{\rho V c_p}\left(T_{air,o} - T_{m,o}\right) \qquad [2.41]$$

Figure 2-14 below shows the simulated heat exchanger coolant outlet temperature compared to the actual outlet temperature. From the figure it is clear there is good agreement between the simulated and actual temperatures, with the exception of some deviation between 1000 and 1500 seconds where the model underestimates the actual coolant temperature.

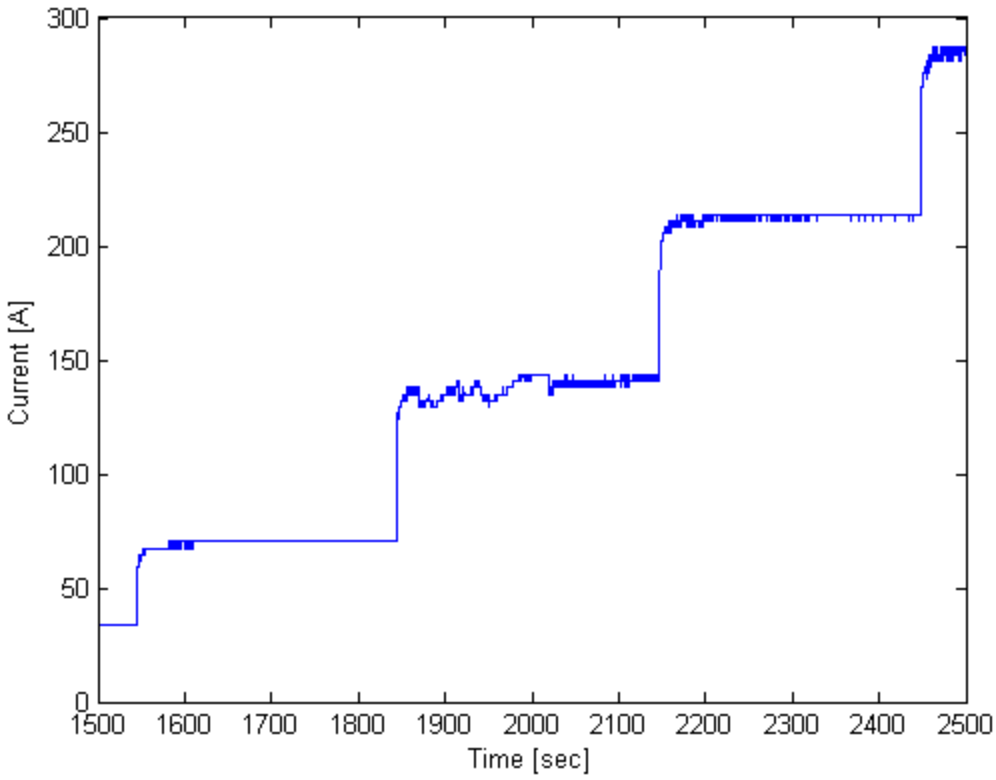

Figure 2-13 Heat Exchanger Verification Load Profile

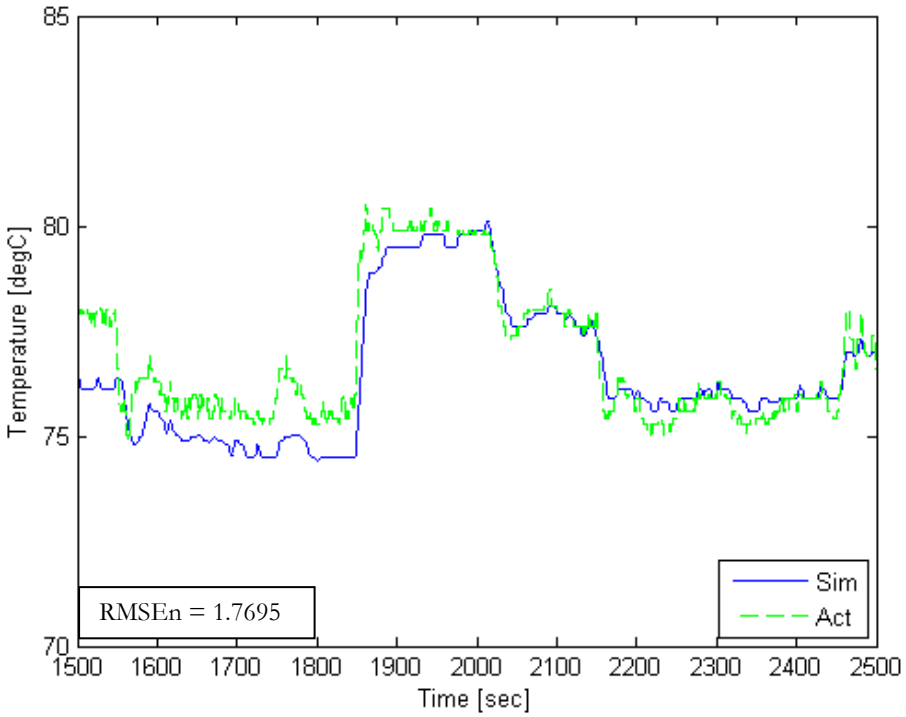

Figure 2-14 Cathode Heat Exchanger Coolant Outlet Temperature

2.8 Anode Heat Exchanger

The onboard storage system stores gaseous hydrogen in a tank and controls the flow of the hydrogen into the stack using a regulating control valve. Due to the high pressure of the gas in the tank and the expansion it undergoes as it passes through the valve, the temperature of the incoming gas is very low. Injecting this cold hydrogen has a negative impact on the stack performance by changing the relative humidity of the membranes near the anode inlet, so it is necessary to preheat the hydrogen before it enters the stack. To accomplish this, an air-to-water heat exchanger is used which utilized the coolant to warm the hydrogen. This heat exchanger is a shell and tube type, with the coolant as the shell fluid and the hydrogen as the tube fluid. At high power, the flow of hydrogen is significant and can cause an additional disturbance to the coolant control. At low power, the flow of hydrogen is small, and as such this heat exchanger does not affect the coolant temperature very much. A simplified modeling scheme is used for the anode heat exchanger as compared to the coolant radiator. Here a static effectiveness-NTU model is used due to the fact the heat exchanger itself is much smaller than the coolant heat

exchanger and it only acts as a disturbance on the coolant system. The heat transfer in the heat exchanger is given by:

$$\dot{q} = \varepsilon C_{min}(T_{c,o} - T_{H2,i}) \quad [2.42]$$

with

$$C_{min} = c_{p,H2}\dot{m}_{H2} \quad [2.43]$$

$\boldsymbol{\varepsilon}$ is the efficiency of the heat exchanger and is estimated from (33) to b 0.85 for a shell and tube heat exchanger with 2 tube passes, which closely approximates the anode heat exchanger. Using a lumped parameter assumption, the heat transfer from the coolant is given by:

$$\dot{q} = \dot{m}_s c_p(T_{c,o} - T_{a,o}) \quad [2.44]$$

Solving Equations [2.42] and [2.44] for the coolant outlet temperature yields:

$$T_{a,o} = T_{c,o} - \frac{\varepsilon c_{p,H2}\dot{m}_{H2}}{c_p \dot{m}_s}(T_{c,o} - T_{H2,in}) \quad [2.45]$$

The hydrogen mass flow rate can be calculated by the consumption rate based on the stack load (2). The hydrogen consumption for a single cell is:

$$\dot{m}_{H2} = \frac{I_s}{2F} \quad [2.46]$$

where I_s is the current and F is Faraday's constant. Multiplying by the number of cells in the stack and converting from mols/s to kg/s yields:

$$\dot{m}_{H2} = 1.05x10^{-8} I_s n \quad [2.47]$$

Taking this result and assuming the hydrogen inlet temperature is equal to the ambient temperature and letting $\alpha = 1.05x10^{-8}$ reduced equation to:

$$T_{a,o} = T_{c,o} - \frac{\varepsilon c_{p,H2} \alpha I_s n}{c_p \dot{m}_s} (T_{c,o} - T_{amb}) \quad [2.48]$$

2.9 System Equations and Assumptions

The final equations used to simulate the FCS are listed below:

$$\dot{T}_{s,o} = \frac{\dot{m}_c}{\rho V} (T_{s,i} - T_{s,o}) + \frac{1}{\rho V C_p} (1.25 - V_{avg}) * n * I_s \quad [2.8]$$

$$\dot{T}_{r,o} = \frac{\dot{m}_r c_p}{C} (T_{r,i} - T_{r,o}) + \frac{G}{C} (T_{r,w} - T_{r,o}) \quad [2.17]$$

$$\dot{T}_{r,w} = G(T_{r,o} - T_{r,w}) + cf_{QITD}(T_{r,i} - T_{amb}) \quad [2.20]$$

$$T_{m,o} = \frac{\dot{m}_{mp} T_{s,o} + \dot{m}_r T_{r,o}}{\dot{m}_{bp} + \dot{m}_r} \quad [2.28]$$

$$G_{pump} = \frac{K e^{\theta s}}{\tau s + 1} \quad [2.29]$$

$$\dot{T}_{c,o} = \frac{\dot{m}_s}{\rho V} (T_{m,o} - T_{c,o}) + \frac{\dot{m}_a c_{p,air}}{\rho V c_p} (T_{air,o} - T_{m,o}) \quad [2.41]$$

$$T_{a,o} = T_{c,o} - \frac{\varepsilon c_{p,H2} \alpha I_s n}{c_p \dot{m}_s} (T_{c,o} - T_{amb}) \quad [2.48]$$

Several assumptions were made in developing these models. First, it was assumed that there is no heat loss or gain to the ambient from piping. Second, any place where transport delays were neglected, it was assumed that the coolant volume between the components was small and any dynamics can be neglected. It was assumed that there was no temperature change in the coolant across the pump. Also, as stated before, pressure drops across components was neglected. This assumption limits this models ability to be used to evaluate component changes,

but since this work is only interested in evaluating different control schemes, this is an acceptable trade-off.

2.10 Model Validation

For the system model to have value for simulation and control design use, it must be validated. One common method to validate a model is to compare data from the physical system to model simulation data. System data taken from a polarization curve was used to validate the non-linear model developed in the previous sections. A polarization curve is a common test used to measure a FCS's performance. The test consists of a series of fixed load points representative of the operating range the system would be expected to see. The model developed for this work was validated against data from an automotive FCS. Figure 2-15 shows the load profile of the polarization curve used to validate the model and Figure 2-16 shows the commanded set points for the bypass valve and coolant pump from the physical system. Figures 2-17 and 2-18 show the stack outlet temperature and temperature differential, respectively, for both the physical system and the model and Figure 2-19 shows the error for the two variables on the same plot. The temperatures shown in Figure 2-17 have been normalized to protect unpublished intellectual property.

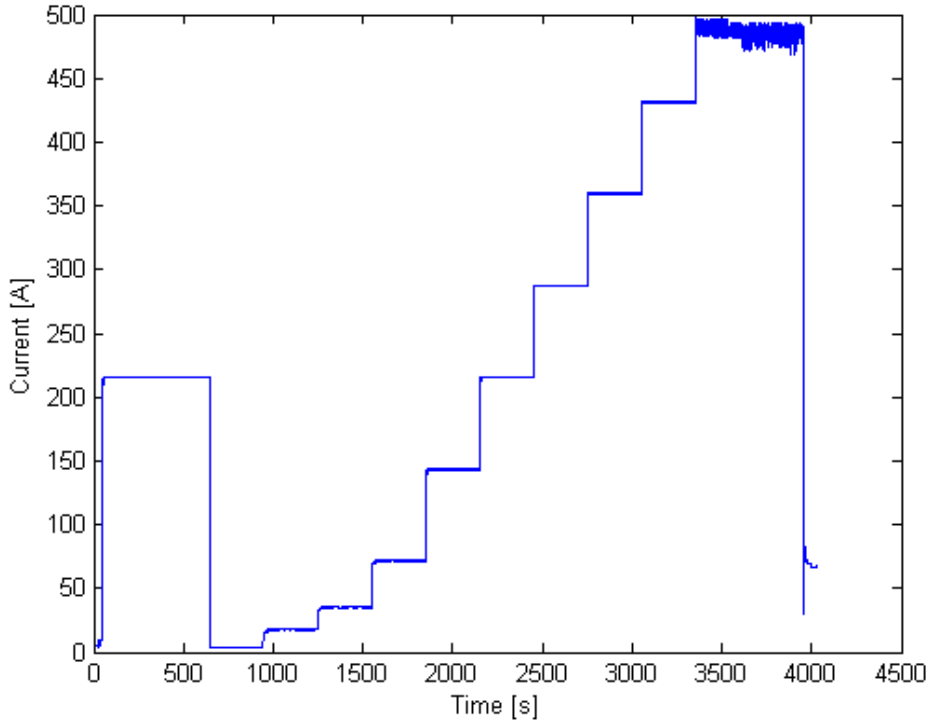

Figure 2-15 Model Validation Pol Curve Current Profile

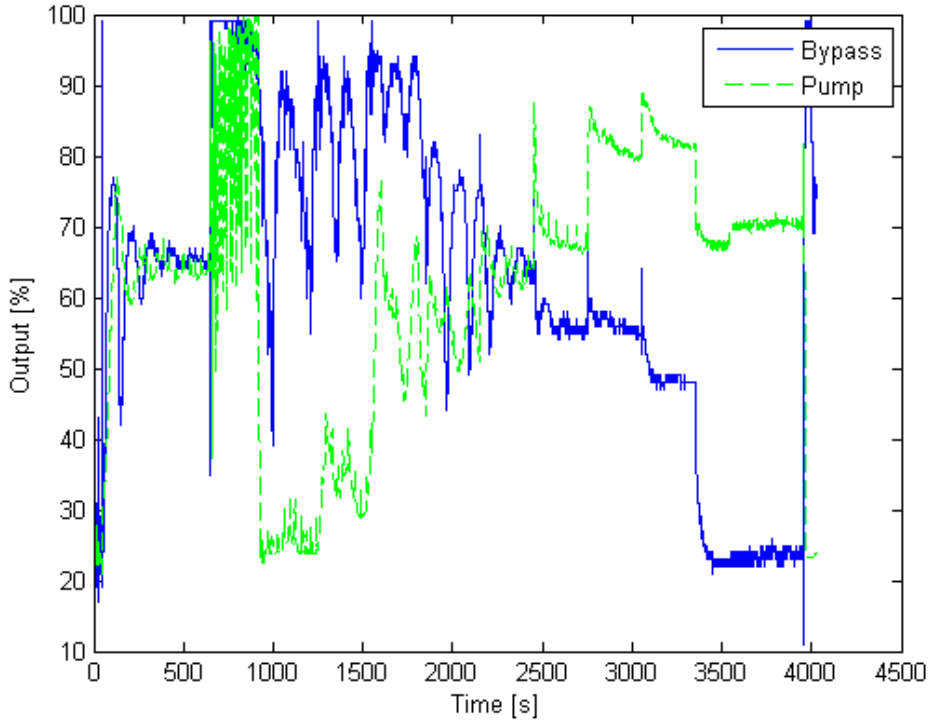

Figure 2-16 Model Validation Pol Curve Set Point Profiles

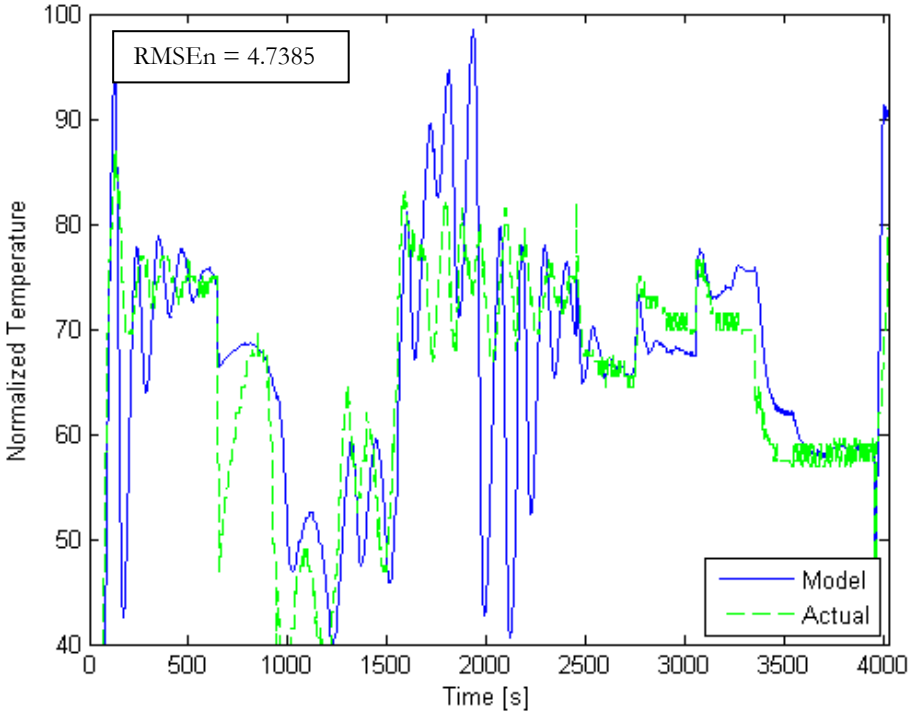

Figure 2-17 Model Validation: Stack Outlet Temperature

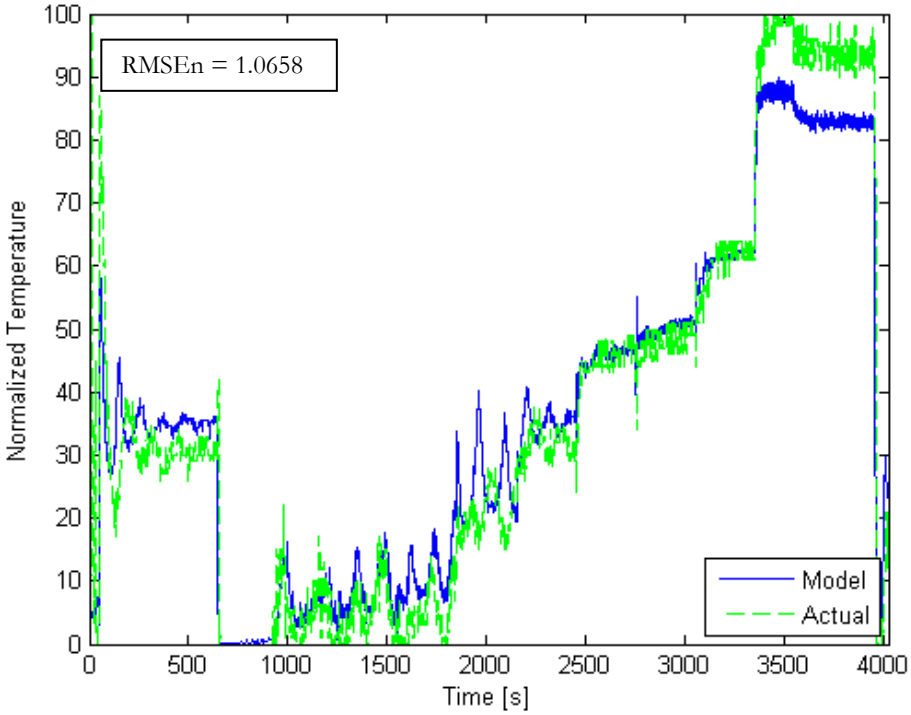

Figure 2-18 Model Validation: Stack ΔT

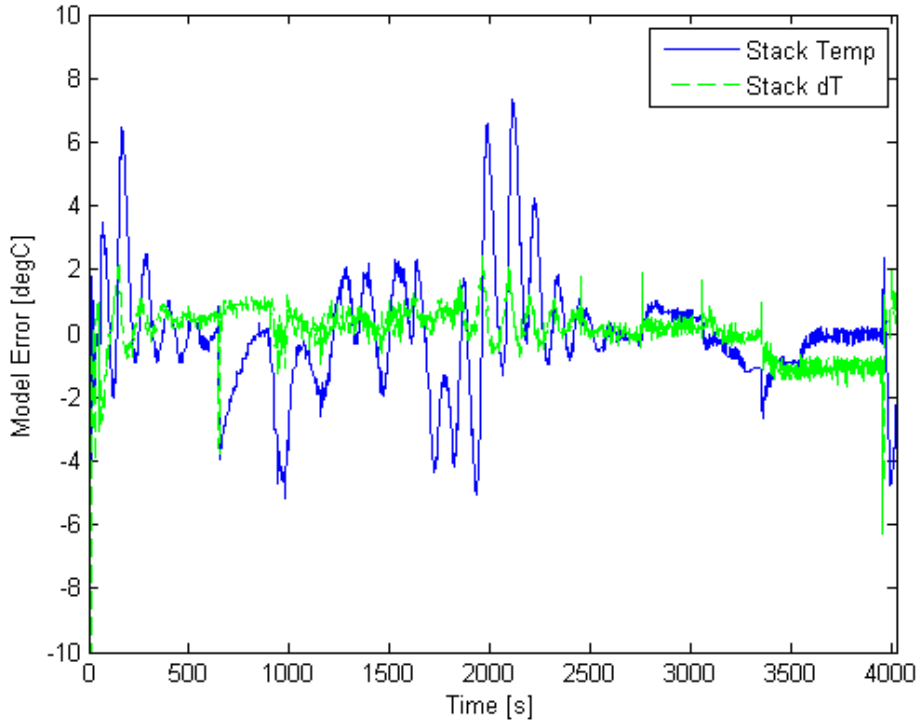

Figure 2-19 Model Validation: Model Error

The model shows good agreement for both stack temperature and temperature differential (ΔT). The normalize RMSE is 1.0658 for the coolant ΔT, which is extremely good since a value of zero would indicate a perfect fit. The RMSEn for the coolant temperature is 4.7385, which also indicates a very good fit. 2-17 shows that the model is more sensitive to changes in the bypass set point than the actual system, which exhibits more dampening. This can be explained by looking at some of the modeling assumptions used. Since pressure drops through the system were neglected, simplifications were made to the coolant pump and flow models. This tends to speed up the change in coolant flow through-out the system, resulting in a faster response to changes in the bypass valve position. This could be improved by adding lag to the bypass valve model; however the error does not degrade the model's performance to warrant the change. Additionally, both the pump and bypass valve set points, seen in Figure 2-16, are fairly noisy as a result of the decoupled PI controllers used when this data was taken. Since the goal of this work is to implement an optimal controller which will reduce controller interaction, this should not be a problem. The magnitude and shape of the transient response does show good agreement. Figure 2-20 shows a close-up of a transient for the coolant outlet temperature. The

coolant ΔT shows excellent agreement between the model and system. As Figure 2-19 shows, the differential error is within +/-1 deg over the entire test. The temperature error shows slightly more error, especially at some of the transients. Overall this model provides a very good representation of the physical system, both in terms of steady-state magnitude and also transient response characteristics.

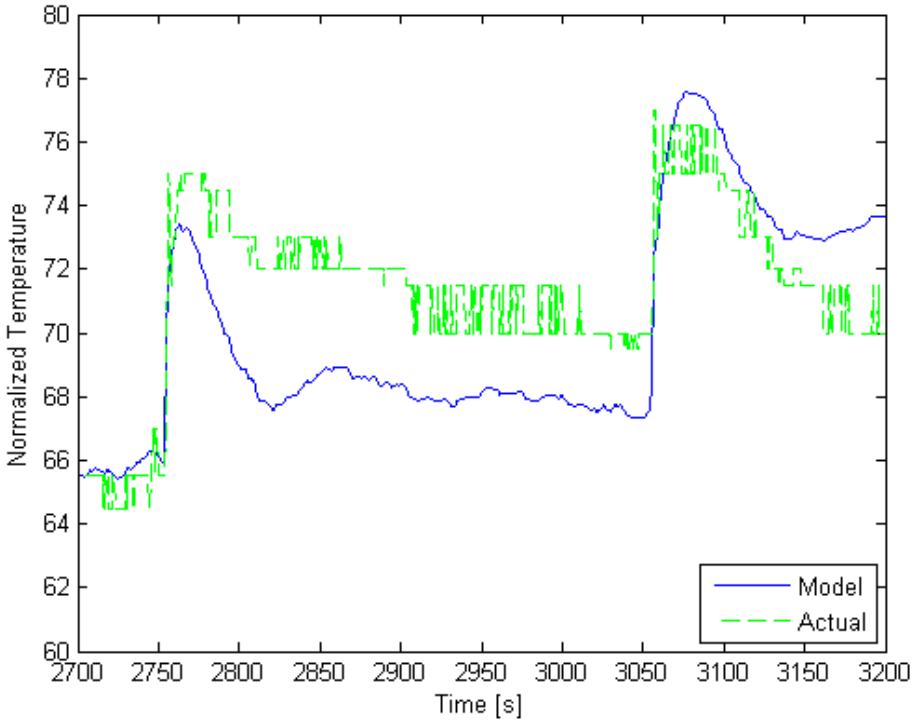

Figure 2-20 Model Validation: Stack Outlet Temperature Transient Response

Along with the validation of the outputs versus system data, the frequency response function (FRF) was generated for the system. The FRF is useful to evaluate the model, and the system response to different input signals. Additionally, the FRF can be used in some frequency design controller methods. The system FRF is generated in the following way. First, input-output data is generated using random, white-noise data for each input channel. To achieve adequate resolution at low frequencies, data must be collected for long periods of time. For this work, $1x10^6$ data points were collected at a sampling rate of 1 Hz. To smooth the data, it is broken up into several pieces, typically in powers of two since a Fourier transform will be taken, and windowed. Here, the data was broken into 32,768 (2^{15}) data-point sections and windowed using a Hanning window. Next, for each section of data the cross-correlation is taken between

each input pair and between each input-output pair. Then each correlation is averaged with that same correlation for the other sub-sets to obtain some degree of smoothing on the data. The Fourier transform is then taken on each of these averaged correlations and then arraigned into two three dimensional matrices. One matrix contains the input correlations and the other contains the input-output correlations. Finally, the FRF is calculated by multiplying the input-output matrix by the inverse of the input matrix at each frequency. This analysis was conducted around three different load cases; 0.2 A/cm^2, 0.6 A/cm^2 and 1.2 A/cm^2. These load cases were selected since they are good representations of a FCS at low, mid and high power. Figures 2-21 through 2-26 show the magnitude and phase response for the FRF at each load case.

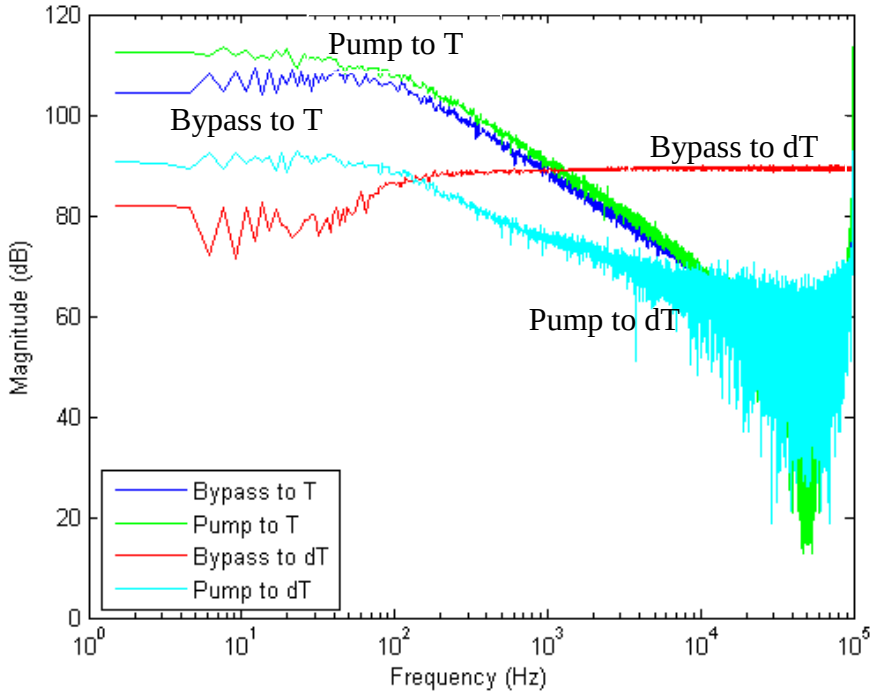

Figure 2-21 Magnitude Response at 0.2 A/cm^2

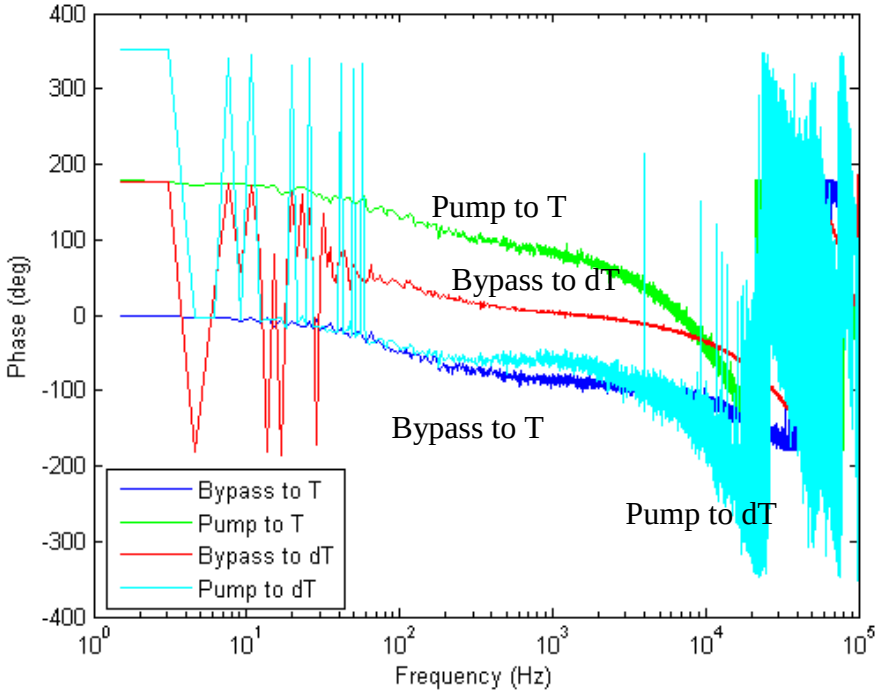

Figure 2-22 Phase Response at 0.2 A/cm²

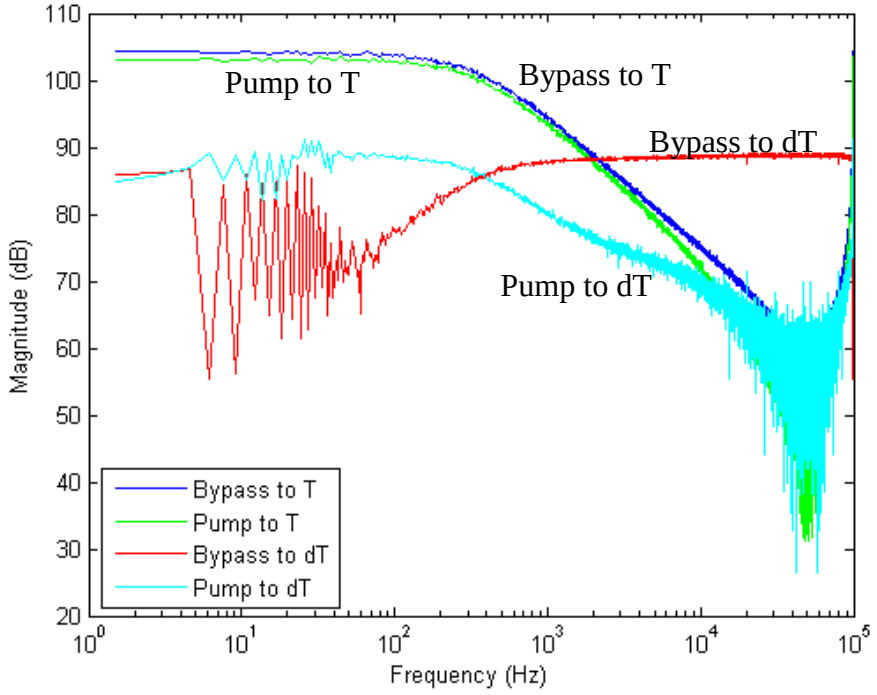

Figure 2-23 Magnitude Response at 0.6 A/cm²

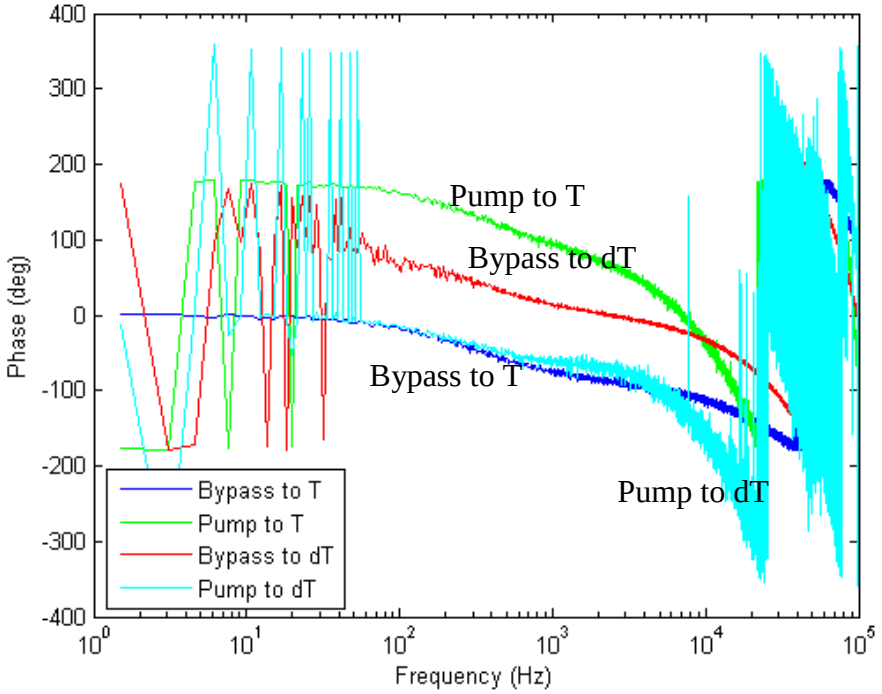

Figure 2-24 Phase Response at 0.6 A/cm²

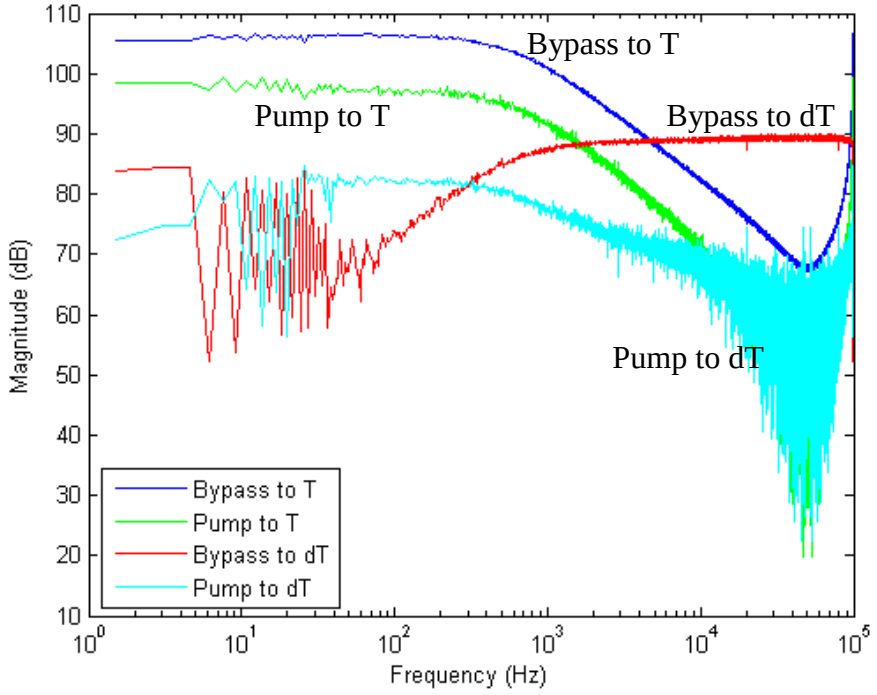

Figure 2-25 Magnitude Response at 1.2 A/cm²

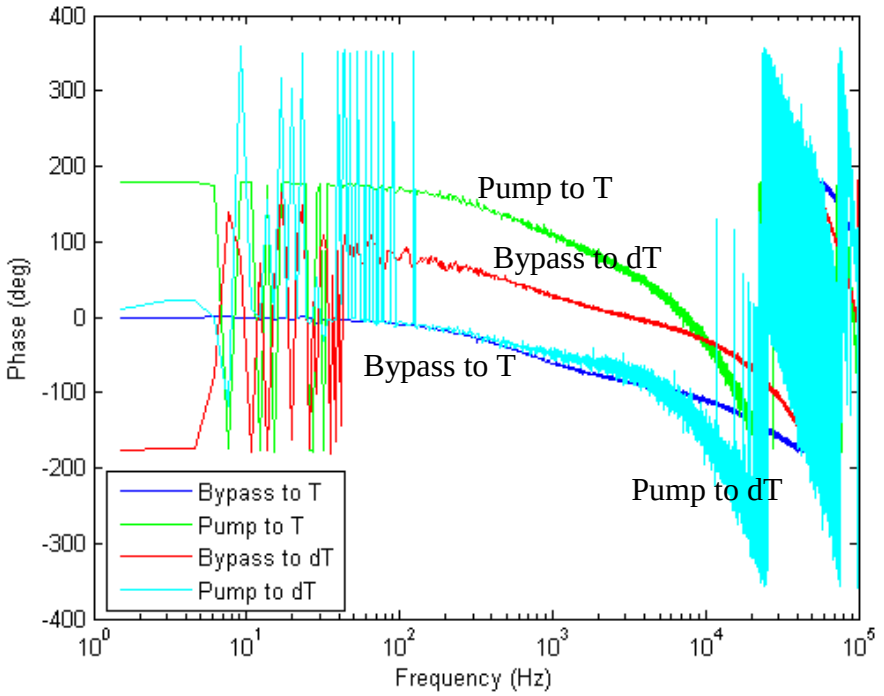

Figure 2-26 Phase Response at 1.2 A/cm^2

An analysis of these plot yields some important information about the system. At all three load cases, the highest static gain is between the bypass valve and the stack outlet temperature(Pair 1), followed by the pump and the stack outlet temperature (Pair 2), the pump and the temperature differential (Pair 4) and finally the bypass valve and the stack temperature differential (Pair 3). Pairs 1, 2 and 4 all exhibit a classic first order response with a roll-off starting around 200 Hz. The fourth pairing's response is more interesting, with a magnitude response similar to a non-minimum phase system. The plots also give us a sense of the non-linearity of the system. By comparing the three different magnitude plots, the non-linearity is more in terms of magnitude than behavior. All three plots show similar forms, but with varying low frequency magnitudes. Pairs 3 and 4, which relate to the stack temperature differential, both show some fluctuation in their responses in the 8 to 60 Hz range, especially in the 0.6 A/cm^2 and 1.2 A/cm^2 load cases. These results also highlight one of the difficulties in controlling this system. The stack coolant outlet temperature has higher gain from either of the actuators than does the coolant ΔT. This indicates both actuators have a stronger effect on the outlet temperature than they do the coolant ΔT. The strong coupling between actuator effort and outlet temperature means any attempt to regulate the ΔT will result in a change in the outlet temperature. This effect will be more fully explored in Chapter 3.

2.11 Reduced Order Model

The full non-linear model is an 8th order model that accurately represents the physical system. However, the higher order nature of the model makes it difficult to linearize and use for control design requiring full-state feedback. As such, it is desired to develop a reduced-order model for use in the control system design. The goal of the reduced order model is to still accurately represent the physical system, but to contain fewer states. Additionally, it is desirable if the reduced order models states are all physically realizable. Realizable states are ones that can be directly measured and do not need to be estimated. The components that contribute the most to the dynamic response of the thermal subsystem are the stack and the radiator. These two components have three states between them. The stack model has one state, the stack coolant outlet temperature. The radiator model has two states, the radiator coolant outlet temperature and the radiator wall temperature. These two components, along with the bypass valve and coolant mixer form the basis of the reduced order model. The pump dynamics are neglected for this model, with a fixed gain being used to convert the pump set point into a flow value. This model is desirable since it has only three states, two of which are easily measured. The third state, the radiator wall temperature is easily estimated from other available measurements.

To test the reduced order model, a simulation was run to compare the reduced order model against the full 8th order model using the familiar pol curve shown in Figure 2-15. The results of the simulation are found below in Figures 2-27 to 2-29. As figure 2-29 shows, the stack coolant ΔT agreement is almost exact between the two models, with a RMSEn of 0.0377, indicating a high degree of fit. The coolant outlet temperature of the reduced order model has a RMSEn of 2.2216, due to a 0.5 to 1 °C offset over most of the simulation, as shown in Figure 2-26. This is due to the fact that the reduced order model neglects the anode and cathode heat exchangers. Both of these components effect the coolant temperature entering the stack and by neglecting them the simulated temperature will vary from the full order model. The charge air cooler has a larger impact on the coolant, tending to raise the temperature which accounts for the negative offset of the reduced order model.

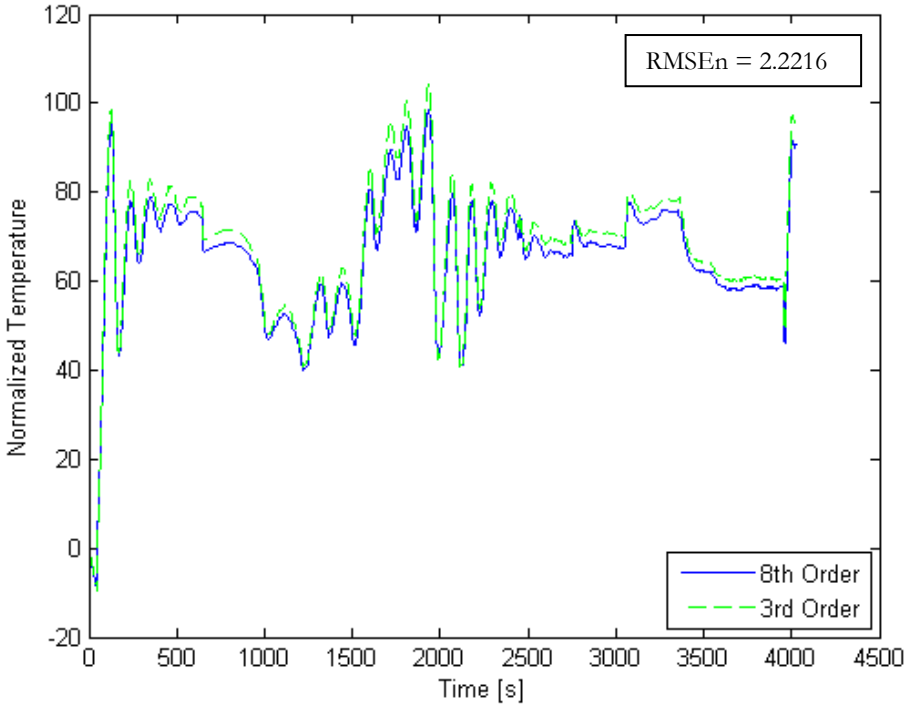

Figure 2-27 Stack Coolant Outlet Temperature Comparison

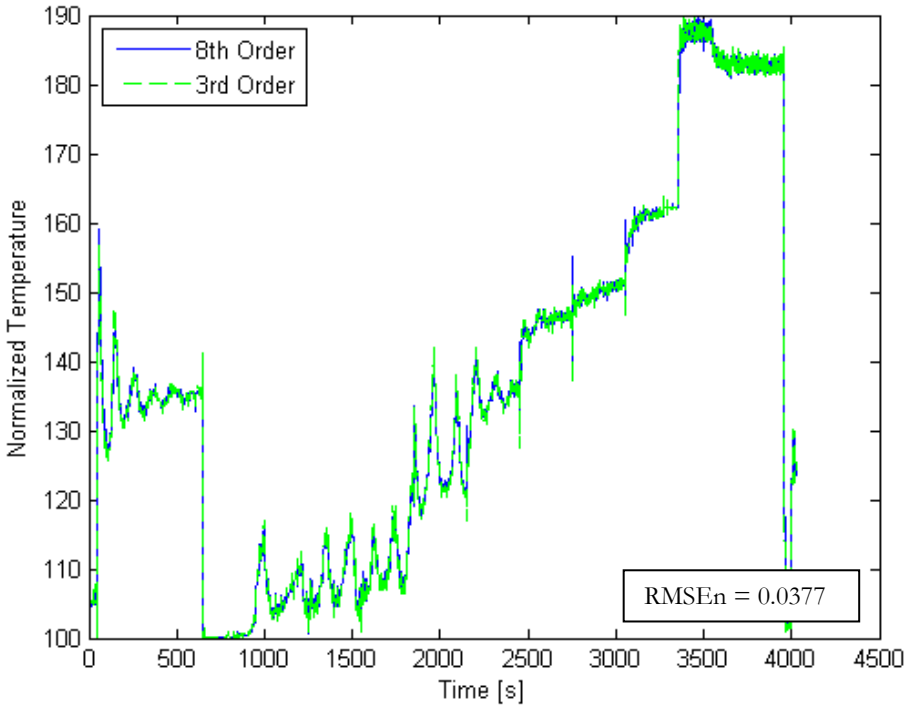

Figure 2-28 Stack Coolant ΔT Comparison

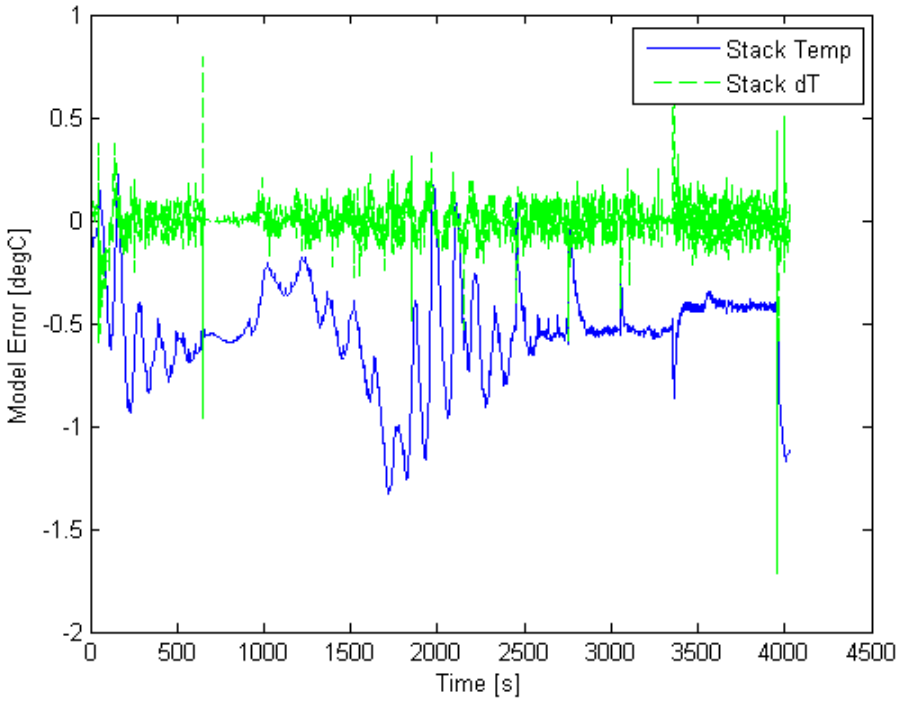

Figure 2-29 Reduced Order Model Error

To compare the frequency response of the reduced order model, the FRF was computed for the reduced order model and compared to the full order model. This was done using the same procedure used in Section 2.10 with the same three load cases: 0.2 A/cm^2, 0.6 A/cm^2 and 1.2 A/cm^2. Figure 2-30 through 2-32 show the magnitude response for the three cases for both models. All three load cases show very good agreement. At the 0.2 A/cm^2 case, there is a 1-2 decibel offset between the reduced order and full model at frequencies below 500 Hz, and then negligible offset above those frequencies. In Figure 2-31, the 0.6 A/cm^2 case again shows a slight offset at lower frequencies, but less than the first load case. In Figure 2-32, the 1.2 A/cm^2 case, there is virtually no offset at the low frequencies, and then some divergence above 1000 Hz. This is not a concern since this is outside the dynamic range of the system. Interestingly, the reduced order model displays the same instability in the 8 to 60 Hz range found in the full order model.

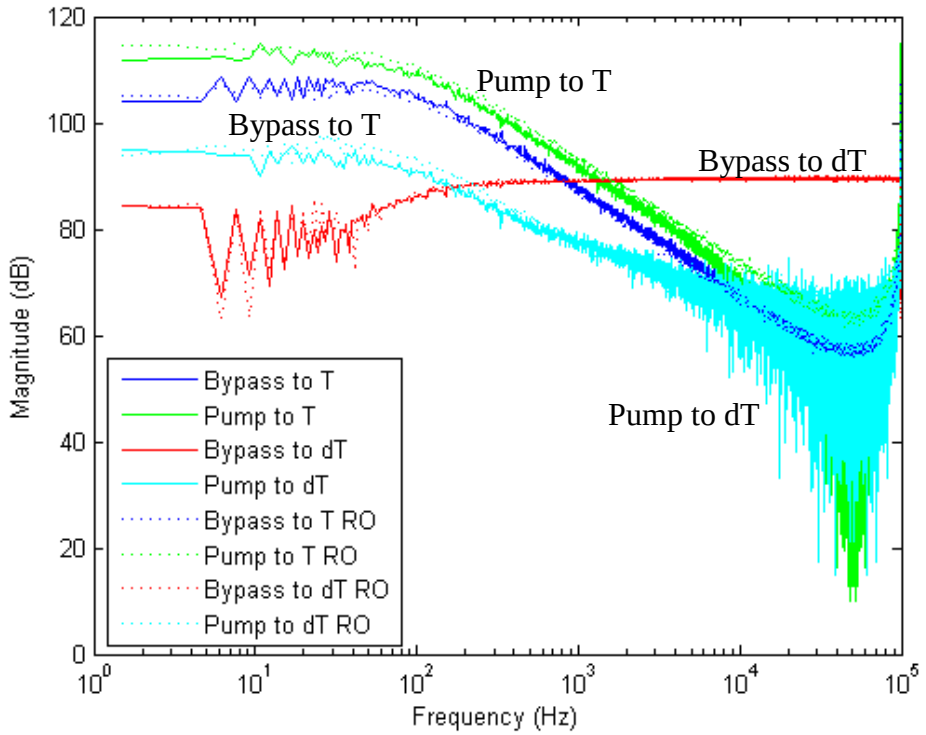

Figure 2-30 RO and Full Model FRF Comparison at 0.2 A/cm²

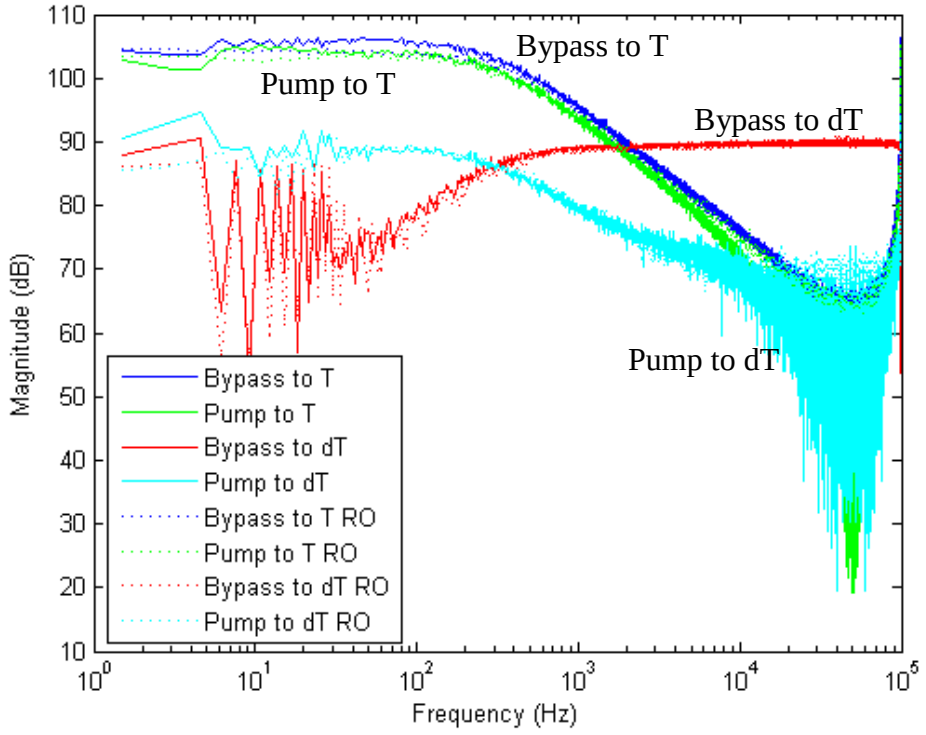

Figure 2-31 RO and Full Model FRF Comparison at 0.6 A/cm²

Bypass to T

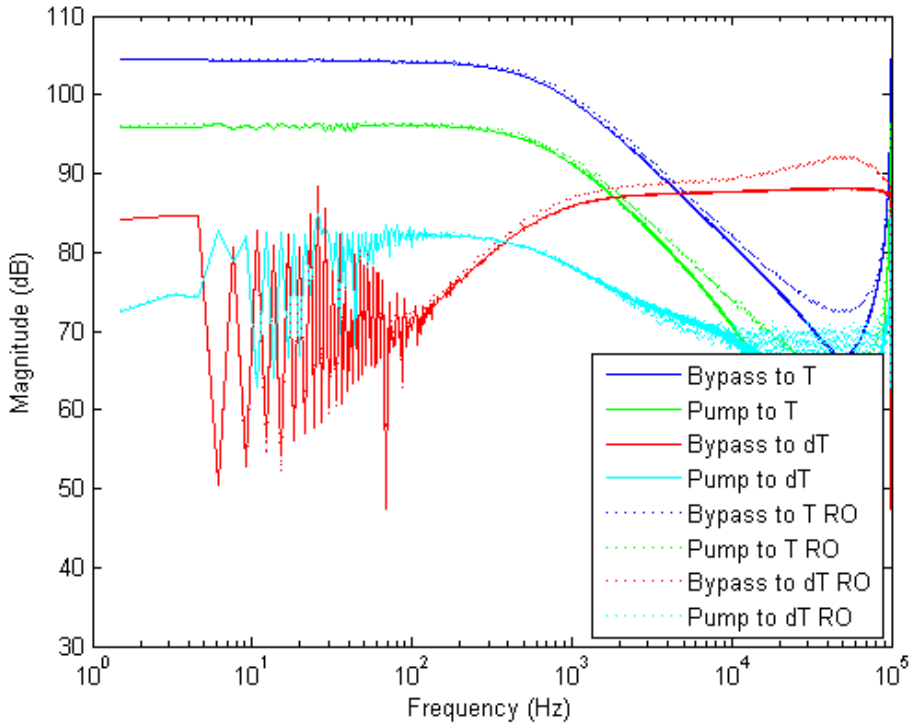

Figure 2-32 RO and Full Model FRF Comparison at 1.2 A/cm²

2.12 Model Linearization

The final step in the model development is to create linearized models based off of the reduced order model. Linear models are needed to design the optimal controller that is considered in Chapter 3. The goal of linearization is to obtain a first order, differential model of the form:

$$\dot{\bar{x}} = A\bar{x} + B\bar{u} \qquad [2.48]$$

$$\bar{y} = C\bar{x} + D\bar{u} \qquad [2.49]$$

where *x* is the state vector, *u* is the input vector and *y* is the output vector. The over-bar notation is used to indicate a vector.

For this work, the reduced order model was linearized at the three operating points considered previously: 0.2 A/cm^2, 0.6 A/cm^2 and 1.2 A/cm^2. The linearization was done using the linear analysis tool in the Control Design toolbox available in Simulink®. By specifying the

inputs and output to the model and the operating point, the tool determines a linear representation of the non-linear model. The method used by Simulink® to linearize the model is a block-by-block approach. For each block in the model, the software uses an analytic Jacobian at the operating point to exactly linearize that block. Since the model is linearized around operating points, the actual form of the model is :

$$\dot{\delta}x = A\delta x + B\delta u \qquad [2.50]$$

where δ is used to represent the deviation from the linearization operating point. δx is represented by:

$$\delta x = x - x_d \qquad [2.51]$$

Appendix A lists the results of the linearization for the three different load cases.

To verify the linear models, simulations were run at each load case while varying the inputs. The results were compared to the full 8th order, non-linear model. Figures 2-33 through 2-41 show the results of the simulations. The figures show that the linear model is very good at predicating the shape of the response for both outlet and ΔT, and has good accuracy in the ΔT magnitude. There is an offset between the two models in terms of outlet temperature, especially at the 0.2 A/cm^2 case. This error should not impact the models use in optimal control design. The 0.2 A/cm^2 results are shown in Figures 2-33 and 2-34, with the actuator inputs for this case shown in Figure 2-35. Figure 2-33 clearly shows the offset between the outlet temperatures of the two models, while both Figures show a divergence of the two models around 6000 seconds. This is the point where the pump set point goes to 20%, indicating that this operating point is most likely too far from the linearization point for this load case, and the linearized model is not valid for these conditions. Limiting operating conditions can be seen for the 0.6 A/cm^2 load case shown in Figures 2-36 to 2-38 when the bypass set point is 87% and when the pump set point is 21%. Interestingly, the coolant ΔT still shows good agreement when the bypass set point is at 87%, with only the outlet temperature showing a large divergence. For the 1.2 A/cm^2 load case, limiting operating conditions are only seen for the outlet temperature, shown in Figure 2-39,

when the bypass valve is at 86%. The coolant ΔT shows good agreement for all operating conditions simulated in Figure 2-40.

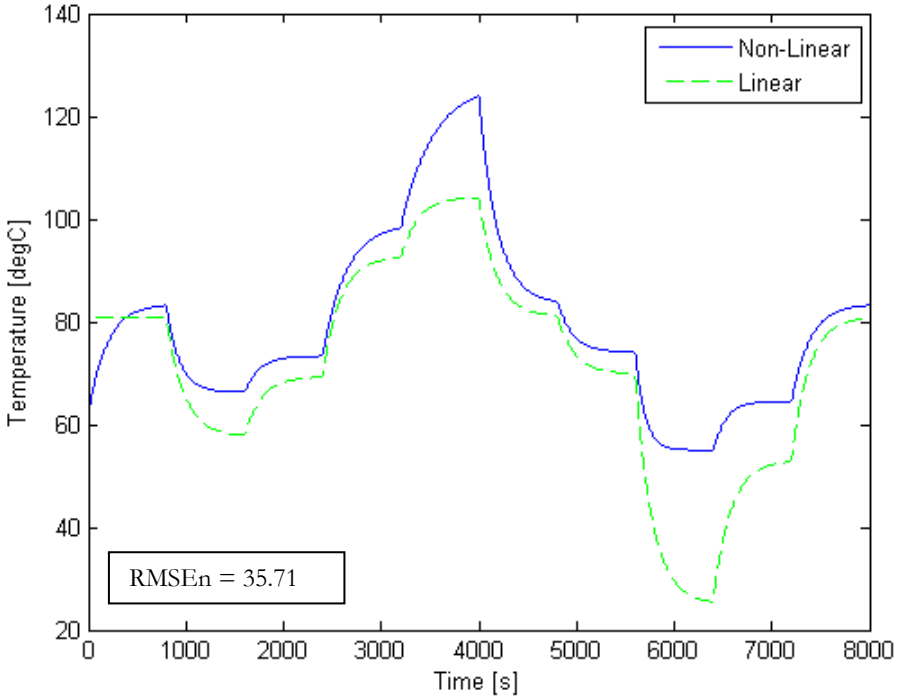

Figure 2-33 Stack Coolant Outlet Temperature at 0.2 A/cm^2

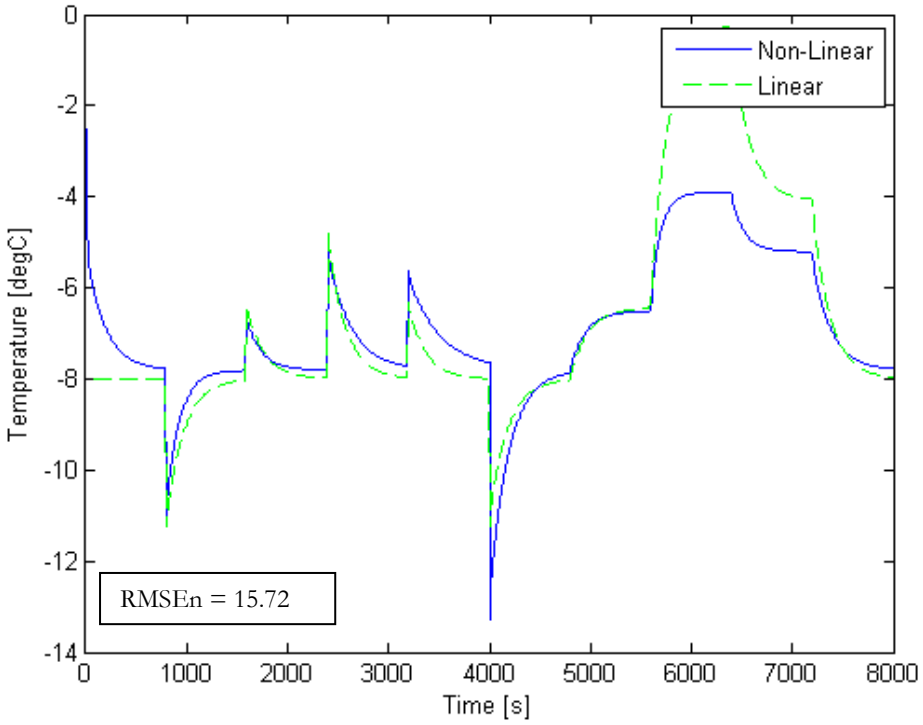

Figure 2-34 Stack Coolant delta T at 0.2 A/cm²

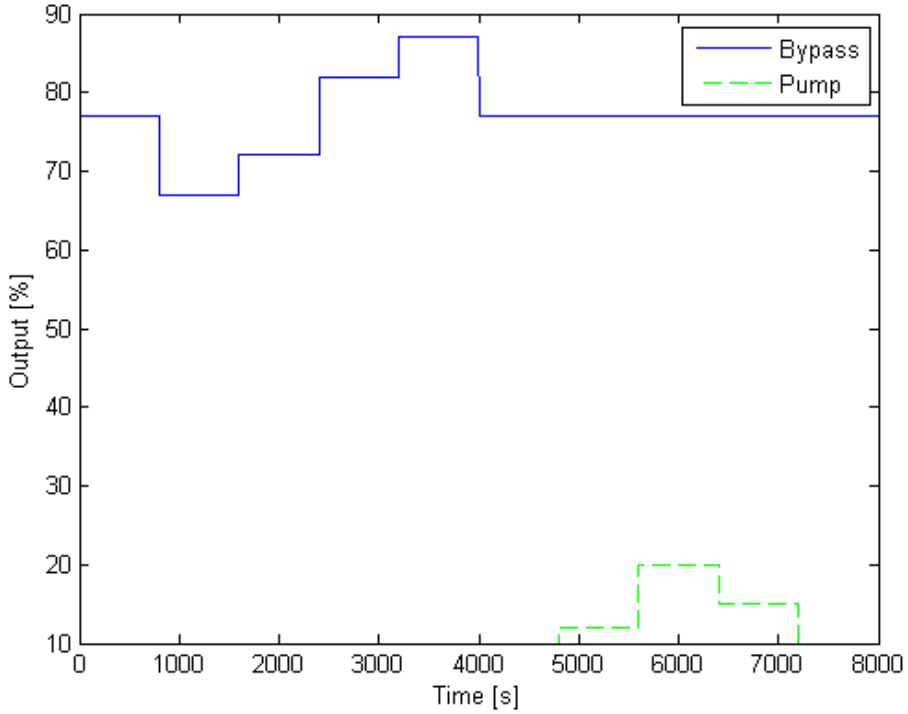

Figure 2-35 Actuator Positions at 0.2 A/cm²

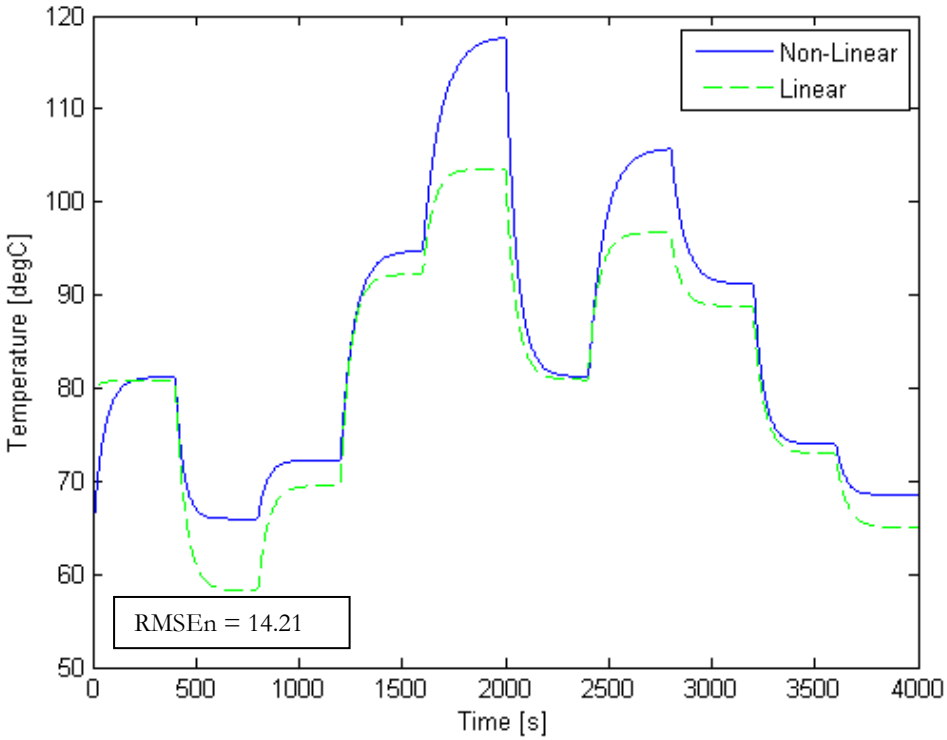

Figure 2-36 Stack Coolant Outlet Temperature at 0.6 A/cm²

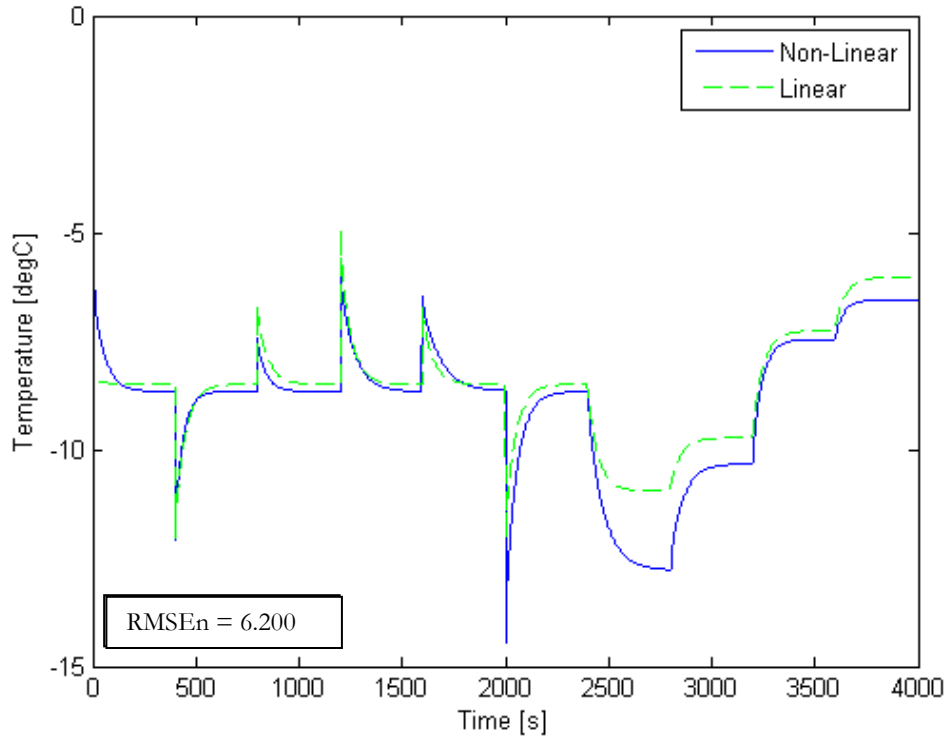

Figure 2-37 Stack Coolant delta T at 0.6 A/cm²

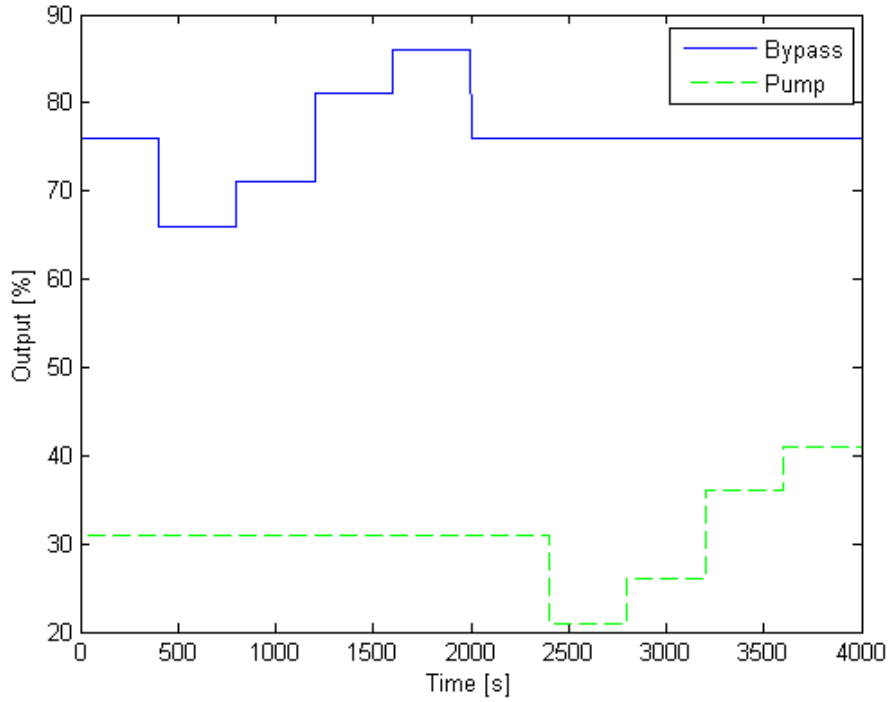

Figure 2-38 Actuator Positions at 0.6 A/cm²

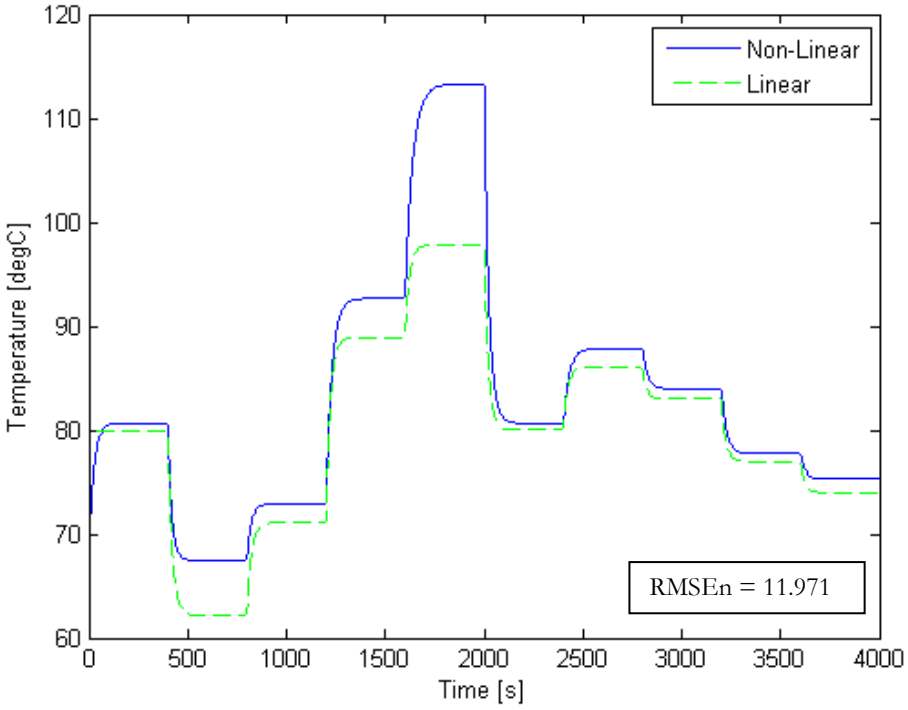

Figure 2-39 Stack Coolant Outlet Temperature at 1.2 A/cm²

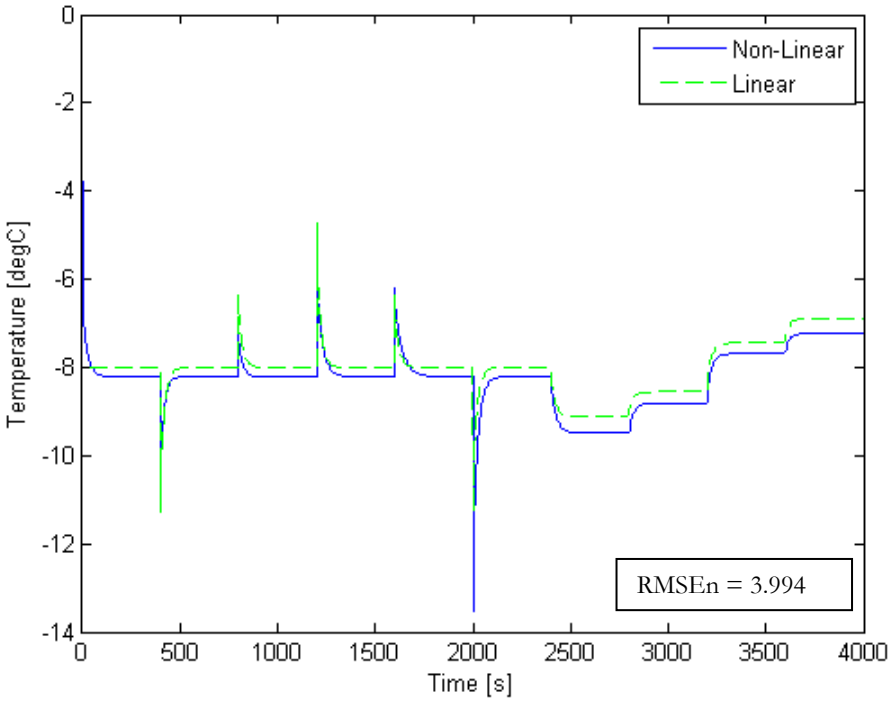

Figure 2-40 Stack Coolant delta T at 1.2 A/cm²

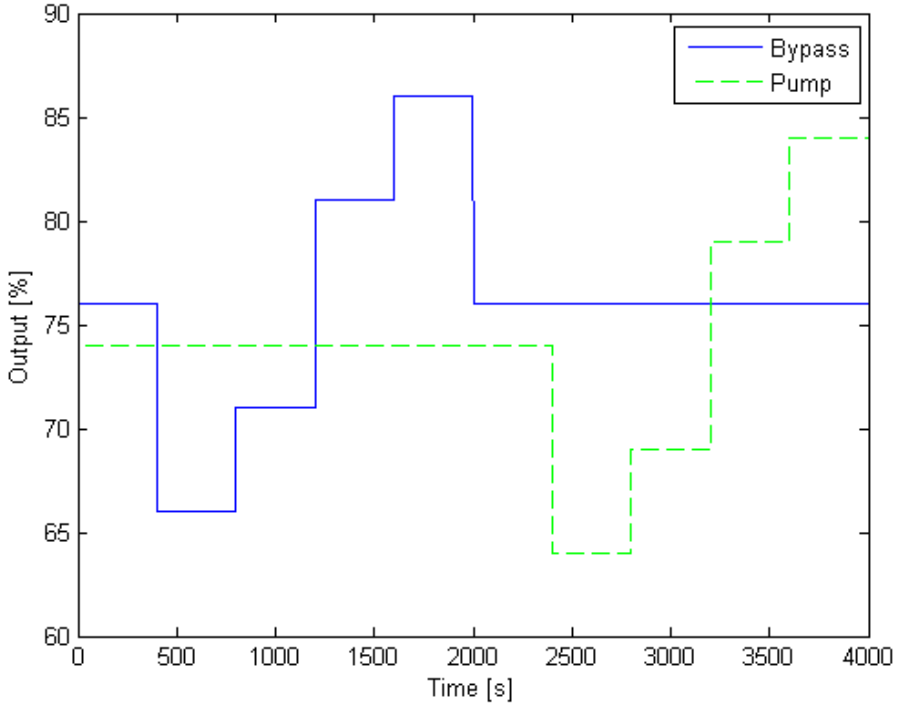

Figure 2-41 Actuator Positions at 1.2 A/cm²

If these models were going to be used for prediction, refinement should be considered. However, for control purposes, the accuracy of the shape of the response, along with reasonable magnitude accuracy are of greater importance, as long as the models are used near the linearization points.

To help understand the non-linear nature of the system, the eigenvaules of the three linear models were computed. These values are shown in Table 2-1 below. All off the eignevalues for the three cases are in the left hand plane (LHF), indicating a stabile system, which agrees with the time simulations of the non-linear model. Additionally, all three poles are real, which agrees with the first-order like response of the non-linear model as well. At each increasing load case, there is a leftward shift in the poles, which indicates the response will be faster. Again, this agrees with the non-linear model which shows faster system response at higher powers.

Table 2-1 Eigenvalues of Linear Models

0.2 A/cm^2	**0.6 A/cm^2**	**1.2 A/cm^2**
-9.045	-9.181	-9.505
-0.141	-0.436	-1.024
-0.006	-0.020	-0.047

The eigenvalues highlight a challenge of the fuel cell's thermal control, the system's response time. At the 0.2 A/cm^2 case, the dominate pole has a time constant of τ = 166 seconds, whileat the 1.2 A/cm^2 case, the dominate pole's time constant is τ = 21.3 seconds, an order of magnitude difference. These long system time constants make temperature control difficult since the system is so slow to respond to input changes. This is clearly illustrated in Figure 2-33, where the stack outlet temperature takes minutes to settle after step changes in the control inputs.

Differences in the thermal system's response at the different load cases can be seen by comparing the magnitude of the values in the input matrix from the linear model. The magnitude of the coefficients for the pump set point remains fairly constant for the three load cases, but there is a large difference in the magnitude of the bypass valve coefficients. This can be seen in Appendix A by looking at the B matrices for the three load cases. This indicates that at low power, the bypass set point has less influence on the system then it does at high power. Again, this agrees with the response of the non-linear system as shown in Figure 2-17. At the low power points, the bypass valve makes large swings in order to try and control the stack

temperature. At the high power points, however, there is much less actuator control effort needed to control the system.

Chapter 3 Controller Design

The objective of the controller for the thermal system is to regulate the stack coolant outlet temperature and temperature differential across the stack. This is necessary to prevent the stack from overheating and to control the relative humidity of the reactant gases. The controller must also effectively compensate for changes in external parameters such as stack current, ambient temperature and radiator effectiveness. In this chapter, the model developed in the previous section will be utilized in the development of the controller. First, the control problem with be formalized. Next, an analysis of the input-output coupling using the Relative Gain Array method will be presented. Two different PID controller schemes will be developed and analyzed. Using the linearized model developed in section 2-12, and LQR methods, a Multi-Input, Multi-Output (MIMO) state-feedback controller will be implemented. Finally, a comparison between the baseline PID and LQR controller will be presented.

3.1 Control Problem Formulation

Figure 3-1 below shows the basic control problem. The objective of the controller is to regulate the stack coolant outlet temperature and the stack differential temperature by manipulating the bypass valve and the coolant pump. Additionally, minimizing the control effort is desired to limit the energy use and prolong the life of the actuators. The actuator power is derived from the stack's power, so limiting this reduces the parasitic load on the stack and increases the system's efficiency. The manipulated variables in this problem are the coolant pump and the bypass valve. The external disturbances are the stack current, the ambient temperature and the airflow across the radiator.

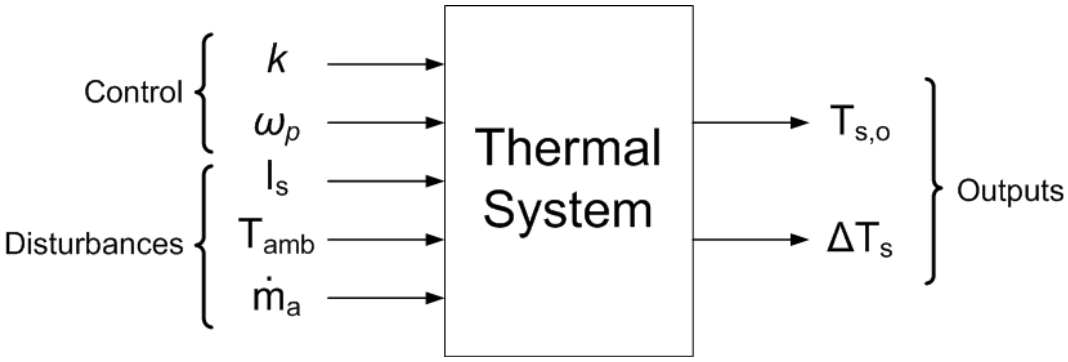

Figure 3-1 Control Problem

The control objectives is to maintain the stack coolant outlet temperature at $T_{s,o}$ = 80 °C and the coolant ΔT at ΔT_s = -8 °C. The measurements available are the stack coolant outlet temperature, $T_{s,o}$, stack coolant inlet temperature, $T_{s,i}$, the stack current, I_s, the ambient temperature, T_{amb}, and the vehicle speed, *v*, from which the radiator air flow, $\dot{m}_a$, can be determined.

3.2 Input-Output Pairing

To determine the relationship between the inputs and the outputs, a technique called the Relative Gain Array (RGA) is used. This method, used by Pukrushpan et. al. (25) indicates the degree of coupling between the inputs and the outputs. This information is used to select the best parings between the outputs and the controlled variables. To compute the RGA, step data was taken from the non-linear system model at the standard operating points: 0.2 A/cm^2, 0.6A/cm^2 and 1.2 A/cm^2. Using this data, first order transfer functions were constructed between each input-output pair. The transfer function gains, *K*, are then computed at frequencies ranging from 0 Hz, the static gain, up to 1000 Hz for each input-output pair. The gain array, *G*, is then constructed at each frequency using the transfer function gains.

$$G = \begin{bmatrix} K_{11} & K_{12} \\ K_{21} & K_{22} \end{bmatrix} \quad [3.1]$$

When in this case, K_{11} would be the gain between the outlet temperature and the pump, K_{12} would be the gain between the outlet temperature and the bypass valve and so on. The RGA is computed from the gain array by:

$$RGA(G) = G * (G^{-1})^T \quad [3.2]$$

The tables below list the static RGA for the three different load cases. The general rule of input-output pairing using the RGA is to pair control inputs with outputs whose relative gain in non-negative and close to unity. (25) These tables indicate that the ideal pairing is to pair the outlet temperature with the bypass valve and the temperature differential with the pump.

Table 3-1 RGA at 0.2 A/cm^2

	Pump SP	Bypass Valve SP
Outlet Temp	0.031	0.967
ΔT	0.967	0.031

Table 3-2 RGA at 0.6 A/cm^2

	Pump SP	Bypass Valve SP
Outlet Temp	0.025	0.975
ΔT	0.975	0.025

Table 3-3 RGA at 1.2 A/cm^2

	Pump SP	Bypass Valve SP
Outlet Temp	0.238	0.861
ΔT	0.861	0.238

Figure 3-2 shows the effect of frequency on the RGA for the three different load cases at different frequencies. While the static RGA indicates the pairings above are the best choice, the figure below shows the problem with only considering the static gains. At several frequencies, there is a reversal in the optimal pairings. For example, at ~ 4 Hz at the 1.2 A/cm^2 load case, the optimal pairing is the pump with the outlet temperature and the ΔT with the bypass valve. This is also the case for the other load cases at 10.2 Hz. This illustrates one of the problems with

independent control schemes. A controller designed for the optimal pairings at the static gains may not be optimal at different input frequencies.

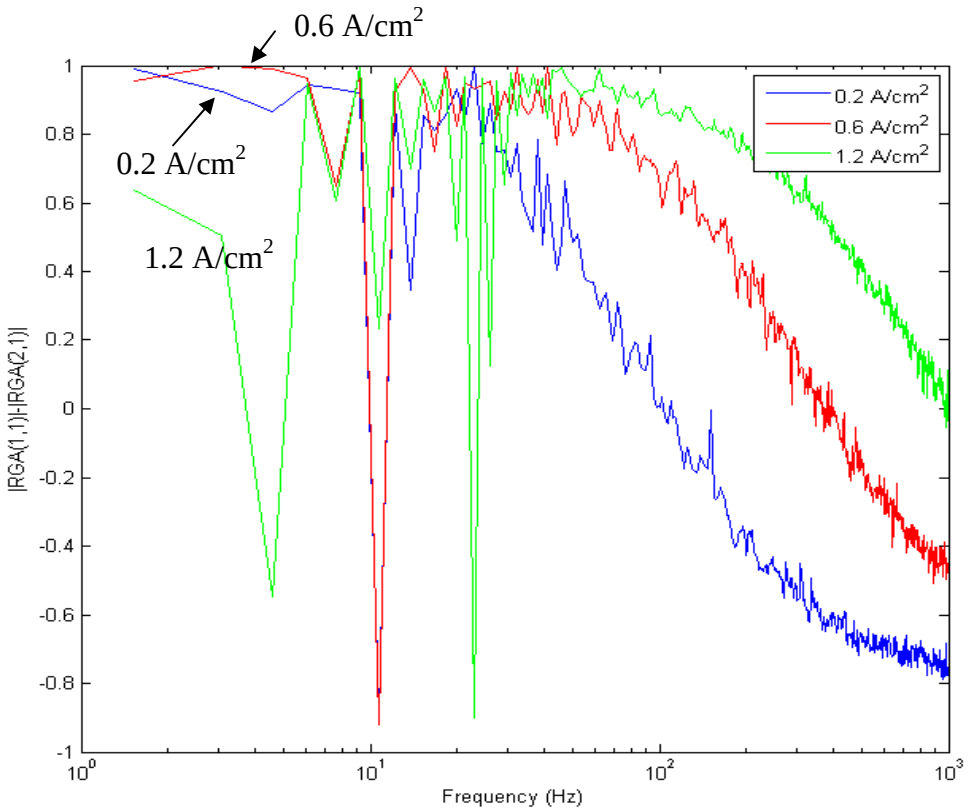

Figure 3-2 Relative Gains as a function of Frequency

3.3 PI Control

Proportional-Integral (PI) control is one of the most commonly used, and often first applied, control schemes. Due to its ease of implementation and relative robustness, it can be found in all but the most complex control systems. The PI controller's ease of use is enhanced by the fact that an accurate process model is not needed to design the controller, although it can be used to improve performance if one available. A process model can be utilized to optimally select the controller gains, as is done in this work. Without a process model, adequate estimates of model parameters can be made to determine gains for the PI controller using open-loop step response data.

For this work, two separate PI control schemes were examined. The first utilized a single PI control loop controlling the stack outlet temperature and the second utilized two PI control loops, controlling both stack coolant outlet temperature and coolant ΔT. For the first case, a PI

controller is implemented to control the stack outlet temperature using the bypass valve as shown below in Figure 3-3. The coolant flow is computed as a function of stack current and cell voltage.

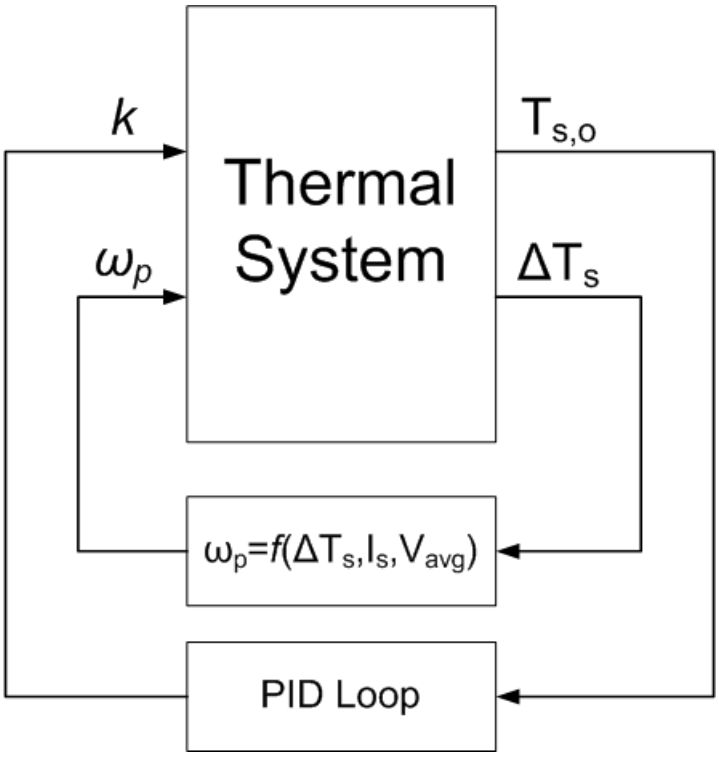

Figure 3-3 Single PI Control Loop

The function is based on an energy balance around the stack. The energy generated in the stack must equal the energy carried away by the coolant to maintain a constant temperature. Starting with Equation [2.7] developed in Section 2.1:

$$\frac{d}{dt}\left(\rho V C_p T_{s,o)}\right) = \dot{m}_s C_p\left(T_{s,\imath} - T_{s,o}\right) + \left(1.25 - V_{avg}\right) * n * I_s q_{gen} = \dot{q}_{cool} \qquad [2.7]$$

and setting the left hand side of the equation equal to zero to represent steady-state conditions yields Equation [3.3]:

$$\left(1.23 - V_{avg}\right) * n * I_s = \dot{m}_s * c_p * \Delta T_s \qquad [3.3]$$

Solving for the coolant mass flow yields Equation [3.4] for flow as a function of stack coolant ΔT, stack current and cell voltage.

$$\dot{m}_s = \frac{(1.23 - V_{avg)} * n * I_s}{c_p * \Delta T_s} \quad [3.4]$$

The pump set point is them related to the mass flow using the data from the pump modeling in Section 2.6. The stack voltage is determined for each current in the stack polarization curve presented in Section 2.10 for model validation. Taking these values and a target ΔT_s of 8 °C, the coolant flow set point was calculated. The goal of this control scheme is to control the bypass valve based on the error in the stack coolant outlet temperature from the desired value, 80 °C. To select the PI gains, an optimization routine was constructed utilizing the fminsearch function in Matlab®. This function attempts to find a local minimum of a cost function by varying the P and I gains. The function runs successive iterations of the system model and computes the value of the cost function for each simulation. Between each simulation, the values of P and I are changed in an attempt to minimize the value of the cost function. The cost function used is:

$$J = \int (q * error^2 + r * u^2) dt \quad [3.5]$$

where *error* is the difference between the desired stack outlet temperature and the actual and *u* is the bypass valve set point. Weighting factors *q* and *r* were varied to achieve the desired dynamic response. By increasing the value of *q* relative to *r*, the importance of the temperature error is increased in the cost function, and gains will be selected which minimize error. The opposite is true if *r* is larger than *q*, in that large control efforts will bias the cost function. After several iterations, *q* was chosen to be 2 and *r* was chosen to be 1. This lead to good temperature performance without excessive actuator control effort. Using these values, the final PI gains were Kp = 8.10 and Ki = 1.95. The system was then simulated using the standard pol curve, with the results shown below in Figures 3-4 and 3-5. To improve the readability of the results, only a portion of the pol curve is shown in the figures below.

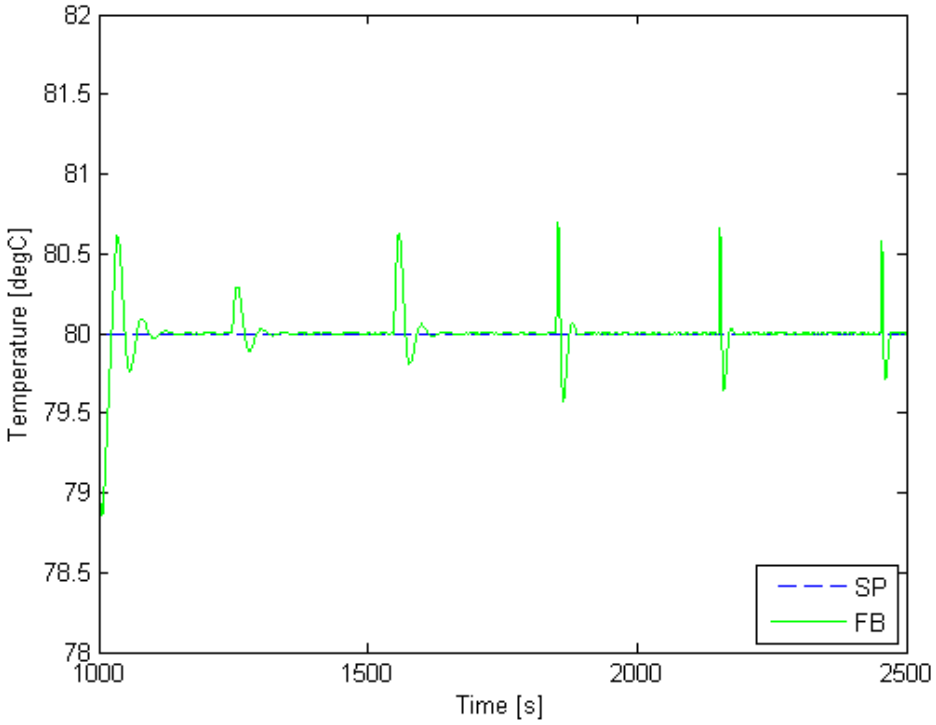

Figure 3-4 Stack Coolant Outlet Temperature: PI Control

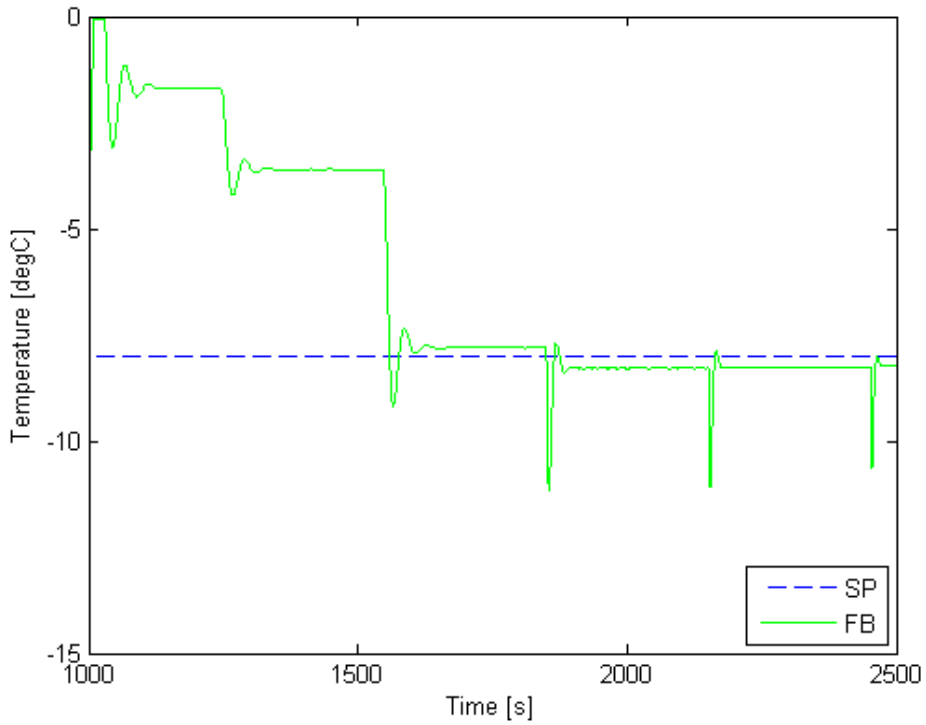

Figure 3-5 Stack Coolant ΔT: PI Control

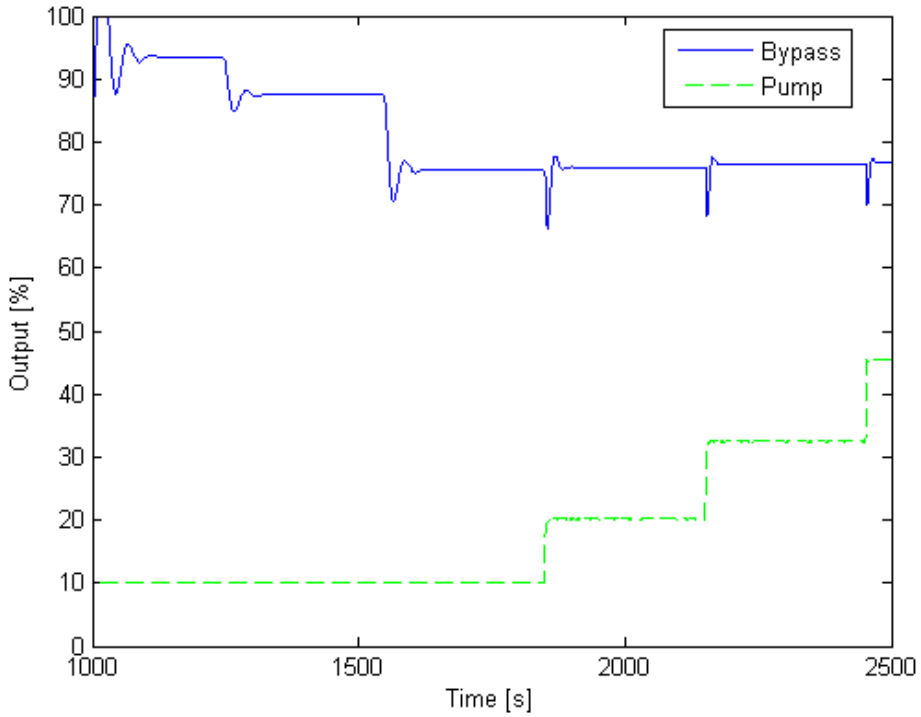

Figure 3-6 Actuator Effort: PI Control

Looking at the figures above, the temperature shows excellent performance during the simulation, with overshoots at current step changes typically around +/- 1°C. The steady state error in Figure 3-5 is one byproduct of using the function to control the coolant flow. Without any feedback in the system, there is no way to compensate for this error. The control effort shown in Figure 3-6 for this control scheme is acceptable, indicating the gains are not so high as to cause excessive actuator effort or chatter, but still maintain good performance. Figures 3-5 and 3-6 clearly show the interaction in the system. Between t = 1000 and t = 1700 seconds, the pump set point doesn't change, yet the ΔT fluctuates every time the bypass valve changes position. If the system did not have interaction, it would be expected that the coolant ΔT would remain constant when the bypass valve changes position.

Figure 3-7 is zoomed in on the start-up and shows the performance of the controller when the coolant is initially at ambient temperature. Here one of the downsides of PI control is evident. Due to the large error, the controller winds-up due to the integral term and overshoots the temperature set point by 15 °C. This level of overshoot could be potentially damaging to the fuel cell stack. While there are many ways to deal with the integrator wind-up, these methods

only serve to add complexity to the controller and negate the PI controller's advantage of simplicity.

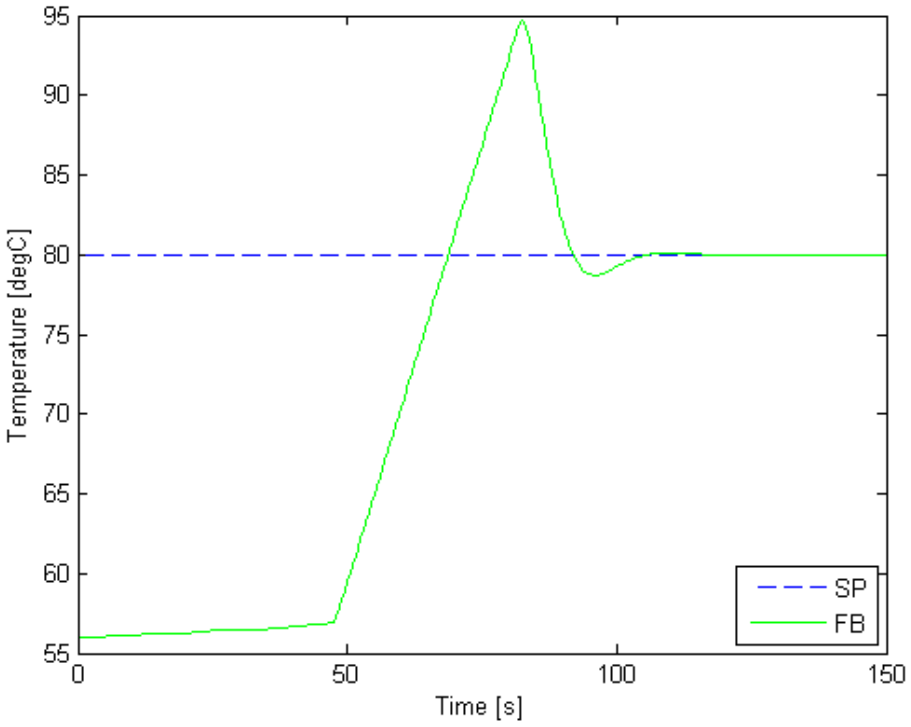

Figure 3-7 Coolant Outlet Temperature during Start-up Conditions

The next control scheme investigated was to use two independent PI control loops, as shown in Figure 3-8 below. The first loop is the one developed above for controlling outlet temperature and a second loop to control the stack ΔT in place of the function found in Equation [3.4].

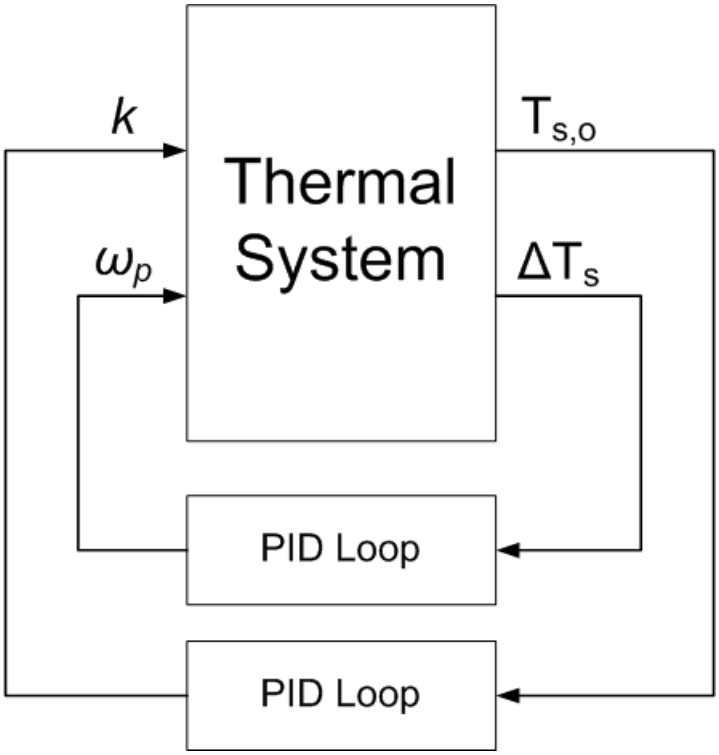

Figure 3-8 Independent PI Control

Gains for this controller were determined using the same cost function. For this optimization, q was set to 25 and r was set to 1 and Kp was found to be 4.2348 and Ki to be 0.2357. Figures 3-9 through 3-11 show the controller performance when simulated using the standard pol curve. Good performance is observed throughout, with a 2-3 °C error in stack delta T at current changes. This could be improved by adding a feed forward term to the ΔT controller based on Equation [3.4]. This would allow the controller to anticipate the effect changes in current will have on the ΔT and start reacting the pump to minimize the disturbance.

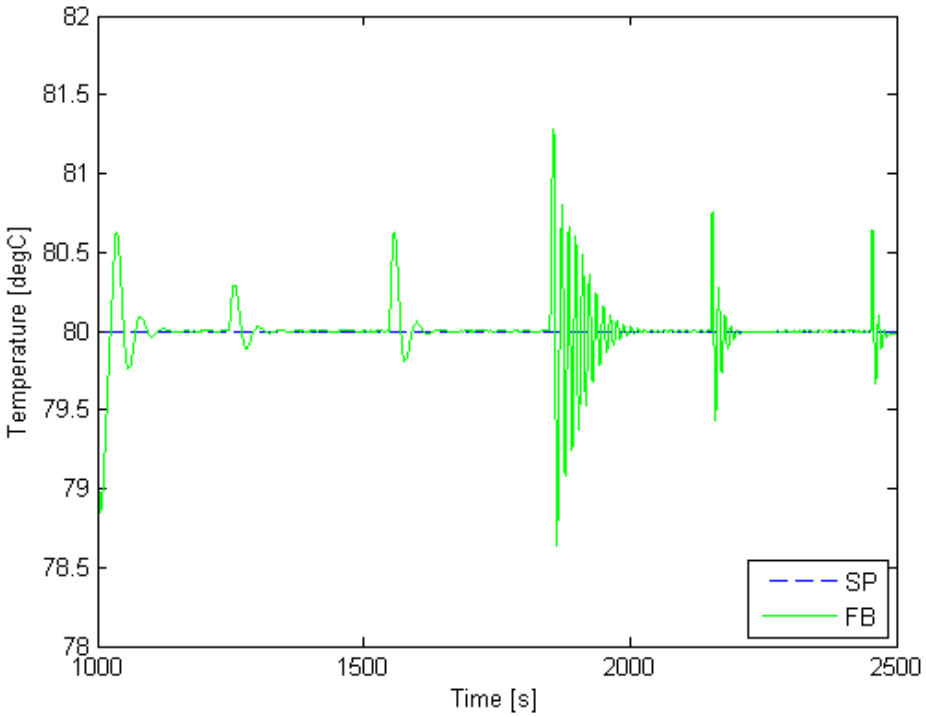

Figure 3-9 Stack Coolant Outlet Temperature: Independent PI Control

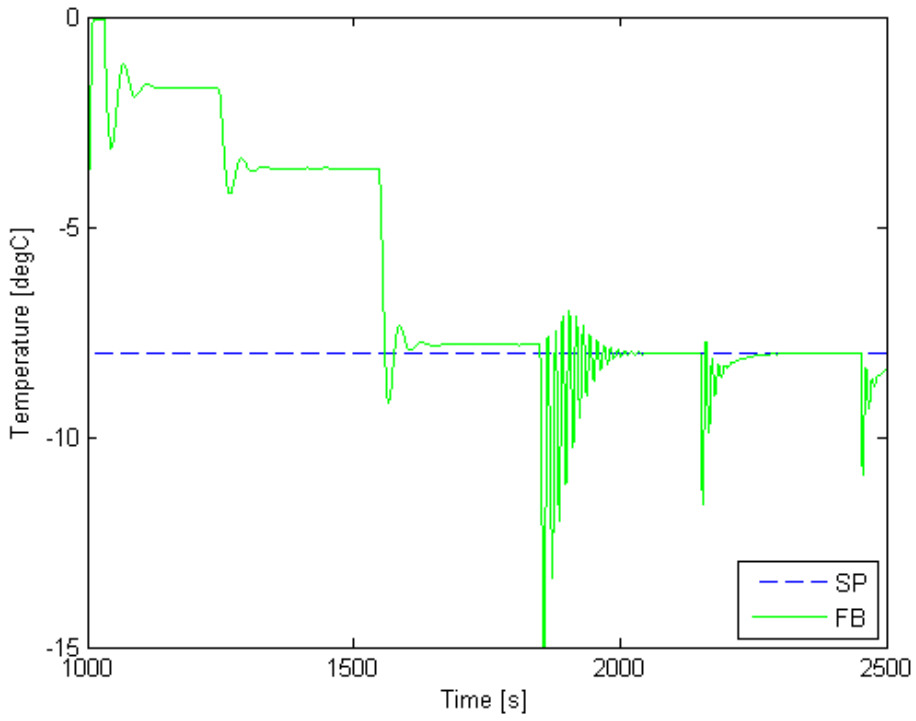

Figure 3-10 Stack Coolant ΔT: Independent PI Control

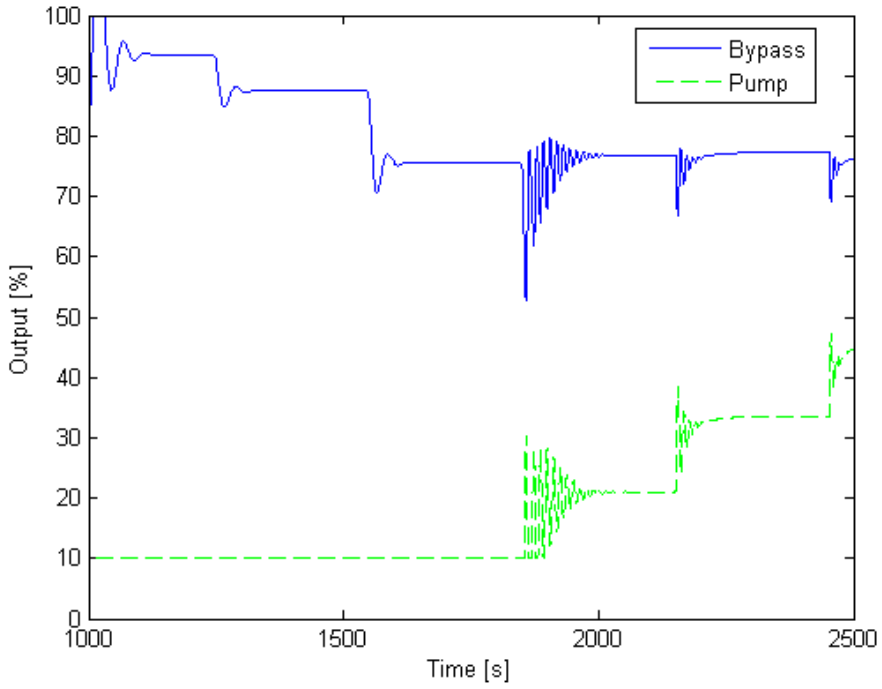

Figure 3-11 Actuator Effort: Independent PI Control

Figure 3-9 shows one of the downsides to using an independent control scheme such as this. With two independent controllers in a system and interaction between the controlled variables, a change in actuator effort for one input-output pair results in a change in the other output variable. This can result in the controllers fighting each other. This can be seen clearly at t=1840, when the current steps from 0.2 A/cm^2 to 0.4 A/cm^2. Figure 3-12 shows a close up of this region. Both controllers attempt to act on their manipulated variable, but this action effects the other manipulated variable as well. The two controllers end up oscillating against each other, out of phase, until the oscillations die out and a new steady state value is reached. This results in the oscillations in temperature seen in Figures 3-9 and 3-10. By comparison, Figure 3-13 shows the same transition for the first case, where only the outlet temperature is controlled by a PI controller. Here there transition is much smoother since there is just one control loop.

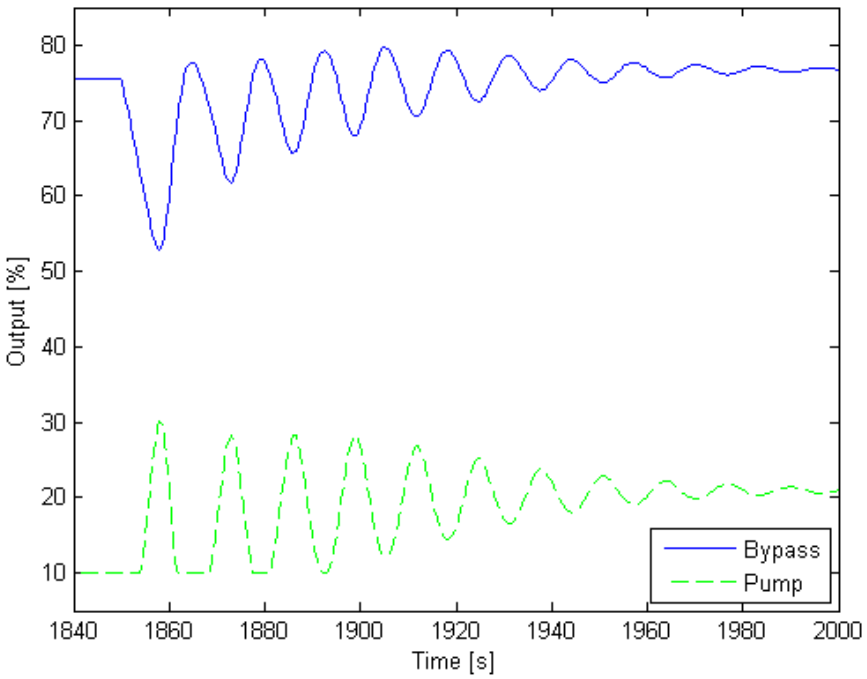

Figure 3-12 Controller Response for Step Change in Current from 0.2 A/cm to 0.4 A/cm²: Independent PI Control

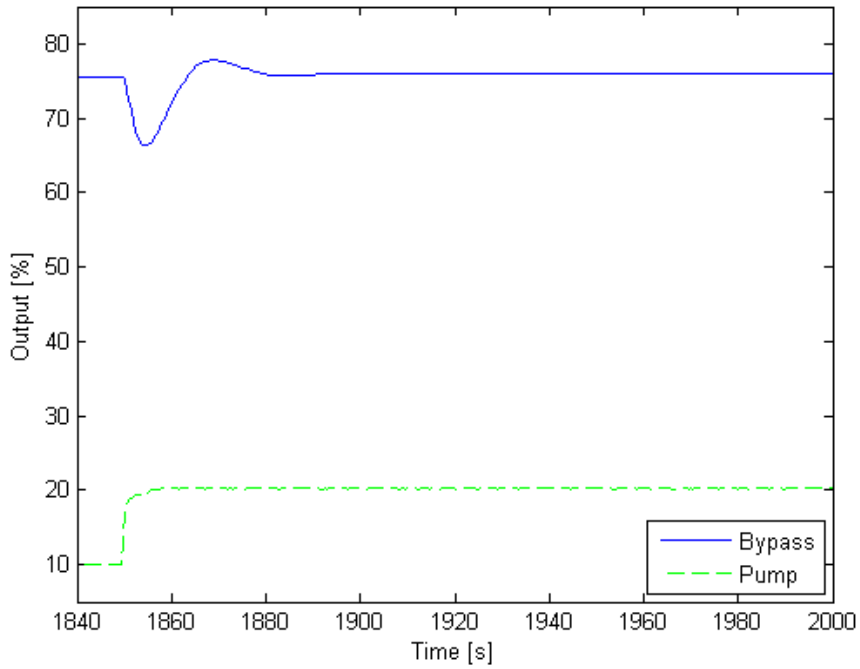

Figure 3-13 Controller Response for Step Change in Current from 0.2 A/cm² to 0.4 A/cm²: PI Control w/ sFF

In an effort to quantify the controller performance and facilitate comparisons between different controllers, several performance metrics were established. The first metric is used to evaluate the tracking performance of the controller using the mean-squared error between temperature set point and feedback. Also, the integral of the controller effort was calculated to gauge the amount of control action used. There is no target value for either of these numbers, however, taken together they represent how effectively a given controller can track the temperature set point relative to the amount of control effort needed.

Table 3-4 Comparison of PI Controller Performance

Case	Tracking Performance	Control Effort
1 PI w/sFF	1.55×10^5	9.54×10^5
2 PI Loops	1.61×10^5	9.60×10^5

Table 3-4 shows an interesting result in that the single PI case actually provided better performance, with 3.9% better tracking while using 0.6% less control effort. However, the single PI case lacks robustness compared to the two PI case since it cannot correct for steady state error in ΔT. The single PI case would only make sense if the confidence in the model was very high and there was no chance for any time dependency of the plant.

3.4 MIMO Control

In an attempt to improve on the performance of the PI control schemes, a multi-input, multi-output (MIMO) control scheme is investigated. The goal of a MIMO controller is to reduce the controller fighting common in a strongly coupled system. There are many MIMO control strategies, but the one selected for this work is a linear quadratic regulator (LQR). A LQR controller is a state regulating controller, which means it acts on error in the system's internal states as opposed to the system's outputs. The controller is designed to drive the system's states to zero by minimizing the cost function:

$$J = \int_0^\infty x^T Q\, x + u^T R\mathrm{u} \qquad [3.6]$$

The weighting matrices used to tune the controller are *Q* and *R*. Increasing *Q* relative to *R* will result in better state tracking at the expense of control effort. Increasing *R* relative to *Q* will more heavily penalize control effort at the expense of state tracking. LQR control assumes a linear system of the form:

$$\dot{\bar{x}} = A\bar{x} + B\bar{u} \quad [3.7]$$

$$\bar{y} = C\bar{x} + D\bar{u} \quad [3.8]$$

where *x* is the state vector, *u* is the input vector and *y* is the output vector. The over-bar notation is used to indicate a vector. The control law, by definition, is:

$$\bar{u} = -K\bar{x} \quad [3.9]$$

where *K* is the gain matrix. The states were computed in section 2.11, and are the stack outlet temperature, $T_{s,o}$, the radiator coolant outlet temperature, $T_{r,o}$, and the radiator wall temperature, $T_{r,w}$. The gain matrix *K* is computed by:

$$K = R^{-1}B^T X \quad [3.10]$$

where *R* is the same as in Equation [3.6] and *X* is the solution to the Algebraic Riccati Equation (ARE). The ARE is given by:

$$XA + A^T X - XBR^{-1}B^T X + Q = 0 \quad [3.11]$$

A more thorough explanation of LQR and sub-optimal control can be found in Lewis. (34) LQR control typically involves selecting a time interval over which the controller acts. The ARE is then solved recursively, which leads to a time variant gain matrix. The gain matrix converges to a steady state value, so to simplify the controller, this steady state value is usually chosen for the gain matrix to make it time invariant. This results in sub-optimal control, but the decrease in controller performance is typically minimal. LQR control requires all of the system's states be available. Since the radiator wall temperature is not measurable, the control problem will be first

solved assuming it is measurable to prove the method. Later, an estimator will be added to measure the unmeasured state, the radiator wall temperature, and its performance will be validated against the full state measurement assumption. Figure 3-14 below shows the control scheme.

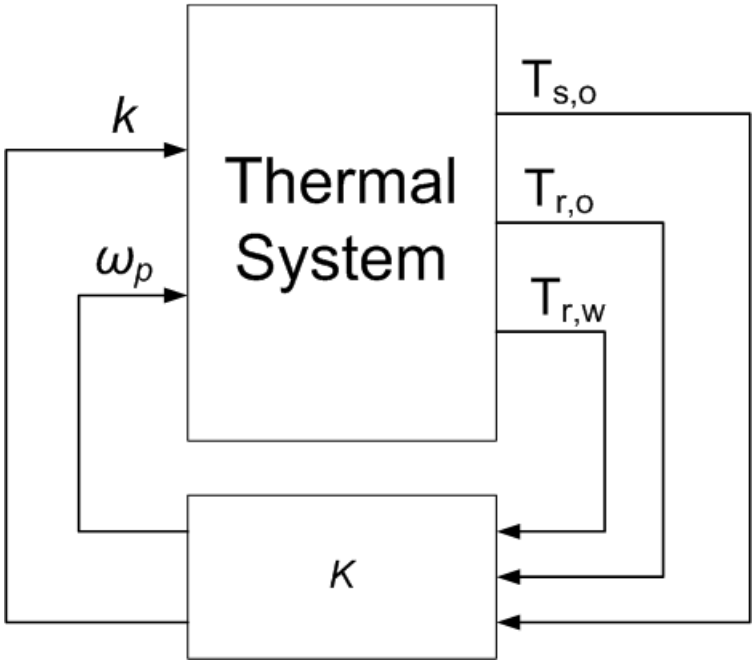

Figure 3-14 LQR Control

The first case considered in the mid-power 0.6 A/cm^2 load case. The gain matrix, *K*, was computed using the weighting matrices:

$$Q = \begin{bmatrix} 25 & 0 & 0 \\ 0 & 1 & 0 \\ 0 & 0 & 50 \end{bmatrix} \quad R = \begin{bmatrix} 0.5 & 0 \\ 0 & 0.5 \end{bmatrix} \qquad [3.12]$$

The values in the weighting matrices were determined experimentally and kept diagonal to simplify the process, since values on the main diagonal effect only one state, where as off-diagonal elements will effect two states. It was found during these simulation that *Q* must be much larger than *R* to obtain good tracking performance. Figures 3-15 to 3-18 show the response to step changes in load around the nominal 0.6 A/cm^2 condition. The performance of the controller is very good, especially in terms of eliminating the interaction found in the independent PI control scheme.

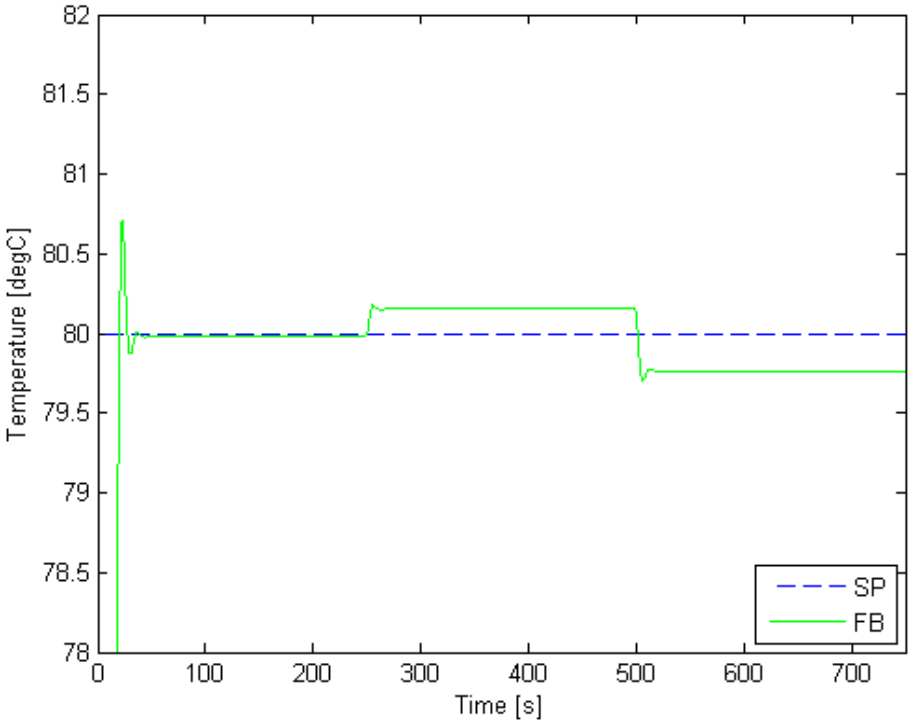

Figure 3-15 Stack Outlet Temperature: 0.6 A/cm²: State Feedback Control

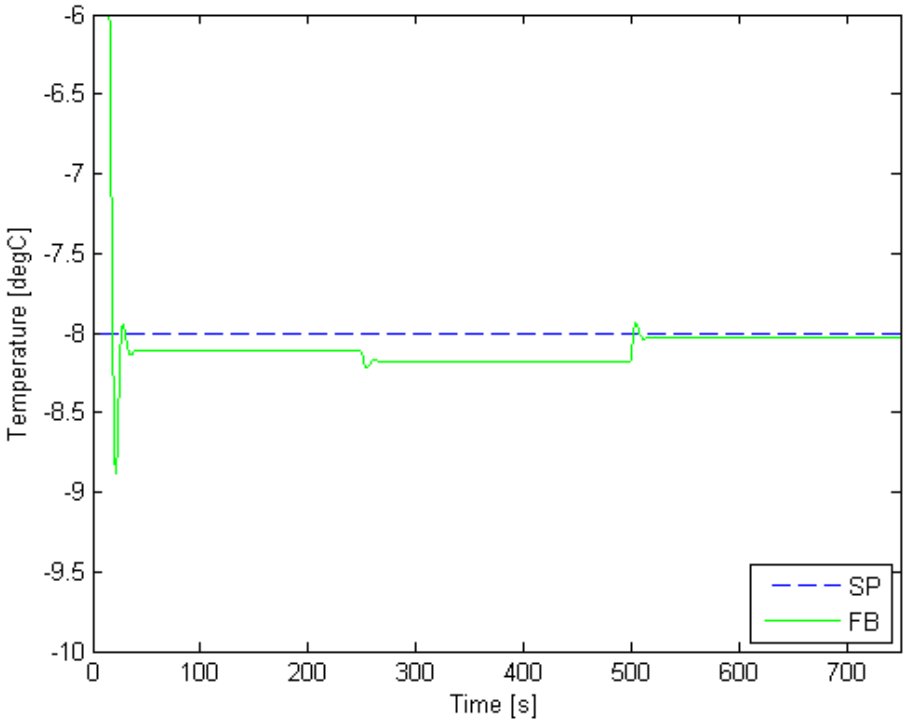

Figure 3-16 Stack ΔT: 0.6 A/cm²: State Feedback Control

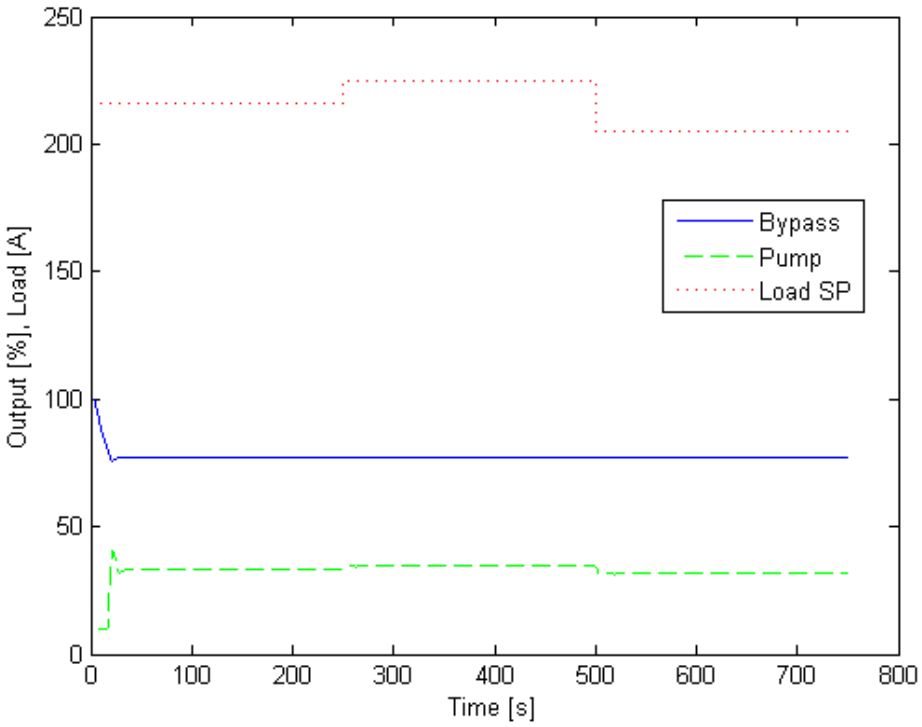

Figure 3-17 Controller Effort: 0.6 A/cm^2

The state feedback control does not exhibit any interaction, as expected. However, there is steady state error in both the temperature and ΔT, which are the outputs. This is due to errors in the estimation of the state set points, x_d, the nominal state set points, which is estimated from the linear model. Any error between the linear model states and the 8th order, non-linear model will cause this steady state error. This can be understood by looking at Figure 3-18, which shows the error in the states. The controller is driving the states to zero, but the zero states of the linearized model may not be the exact zero states of the 8th order, non-linear model. If the system were linear, then we would not expect any error in the outputs. Since the system is non-linear, steady state error in the outputs results.

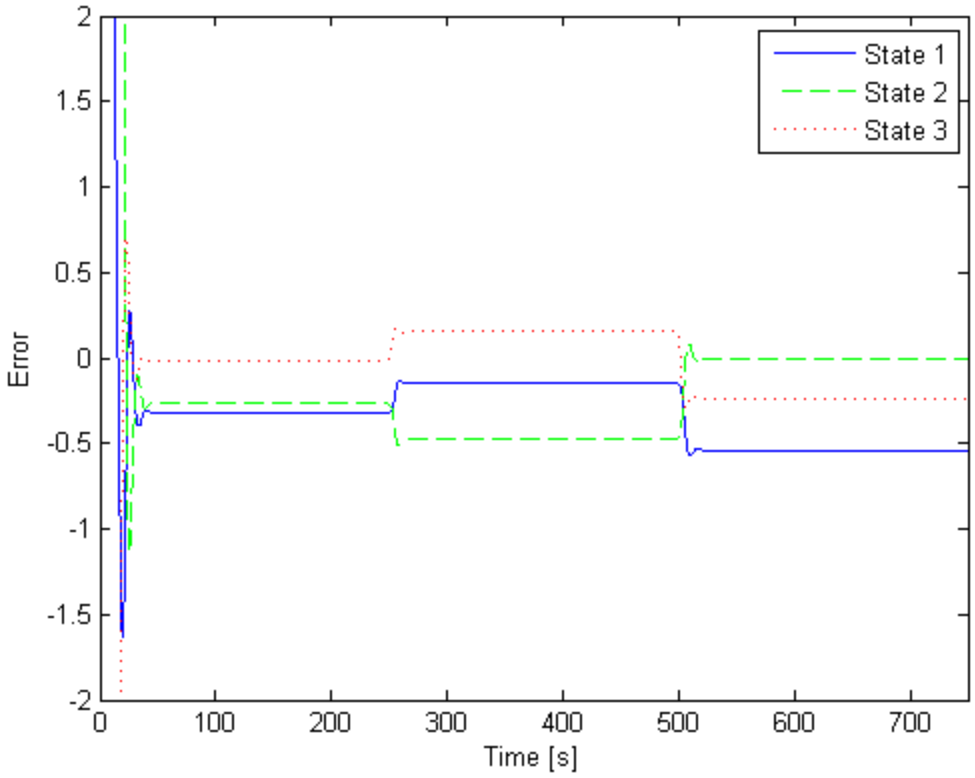

Figure 3-18 State Error: 0.6 A/cm²

One way to improve the steady state error is to include the output feedback error in the controller. (25) By modifying the controller to act on both the state error and the output error, the controller's performance can be improved. Figure 3-19 shows the modification to the original LQR controller:

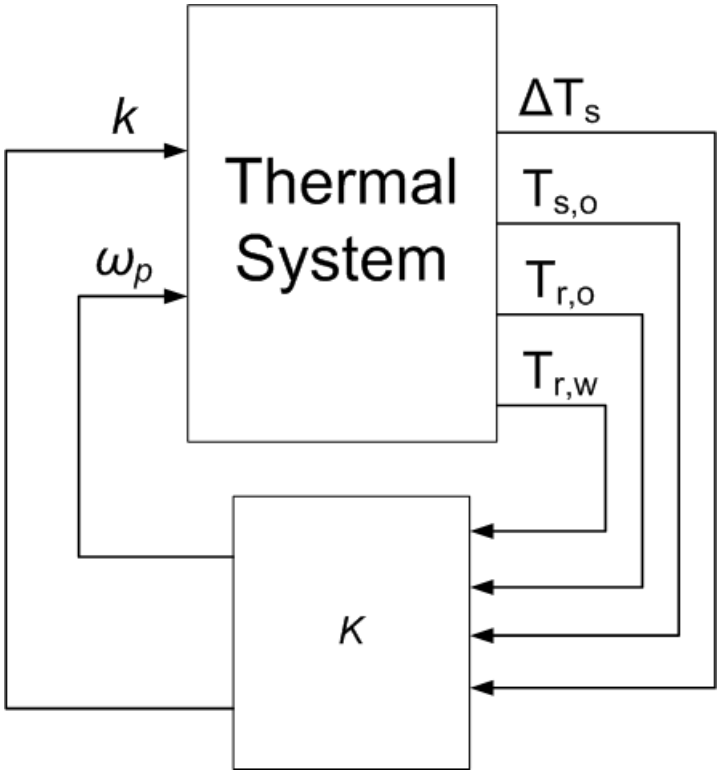

Figure 3-19 Augmented LQR Control with Output Feedback

where the coolant ΔT measurement is also fed back into the gain matrix, *K*. The linear plant is augmented by two additional states, q, which represents the error in the outputs.

$$\begin{bmatrix} q_1 \\ q_2 \end{bmatrix} = \begin{bmatrix} T_{stk\ out}^{ref} - T_{stk\ out} \\ \Delta T_{stk}^{ref} - \Delta T_{stk} \end{bmatrix} \quad [3.13]$$

The reference temperatures are the same as used in the previous sections: $T_{s,o}$= 80 °C and ΔT_s = -8 °C. The linear system is augmented by the new states q as follows:

$$\dot{x}_a = \begin{bmatrix} A & 0 \\ 0 & C \end{bmatrix} \begin{bmatrix} x \\ q \end{bmatrix} + \begin{bmatrix} B \\ D \end{bmatrix} u = A_a x_a + B_a u \quad [3.14]$$

The cost function given in Equation [3.6] is modified to be:

$$J = \int_0^\infty x_a^T \begin{bmatrix} C^T Q_x C & 0 \\ 0 & Q_y \end{bmatrix} x_a + u^T R\, u \quad [3.15]$$

where Q_x is the weighting matrix on the state variable error and Q_y is the weighting matrix on the output variable error. R is the same as before. Using the augmented system, the gain matrix is recomputed in the same manner as the original LQR problem. The weighting matrices used for the 0.6 A/cm^2 case are:

$$Q_x = \begin{bmatrix} 15 & 0 \\ 0 & 25 \end{bmatrix} Q_y = \begin{bmatrix} 5 & 0 \\ 0 & 10 \end{bmatrix} \; R = \begin{bmatrix} 1 & 0 \\ 0 & 1 \end{bmatrix} \qquad [3.16]$$

The results of the simulation with the augmented controller are found in Figures 3-20 and 3-21. The augmented LQR control exhibits slightly better steady state performance than the standard LQR controller. The RMSE for the augmented controller outlet temperature is 208.1, versus 239.8 for the original LQR controller, a 13% improvement. In the case of the ΔT control, the improvement was less than 1%. The augmented controller has the added benefit that the output variables error is part of the feedback, improving the system's robustness.

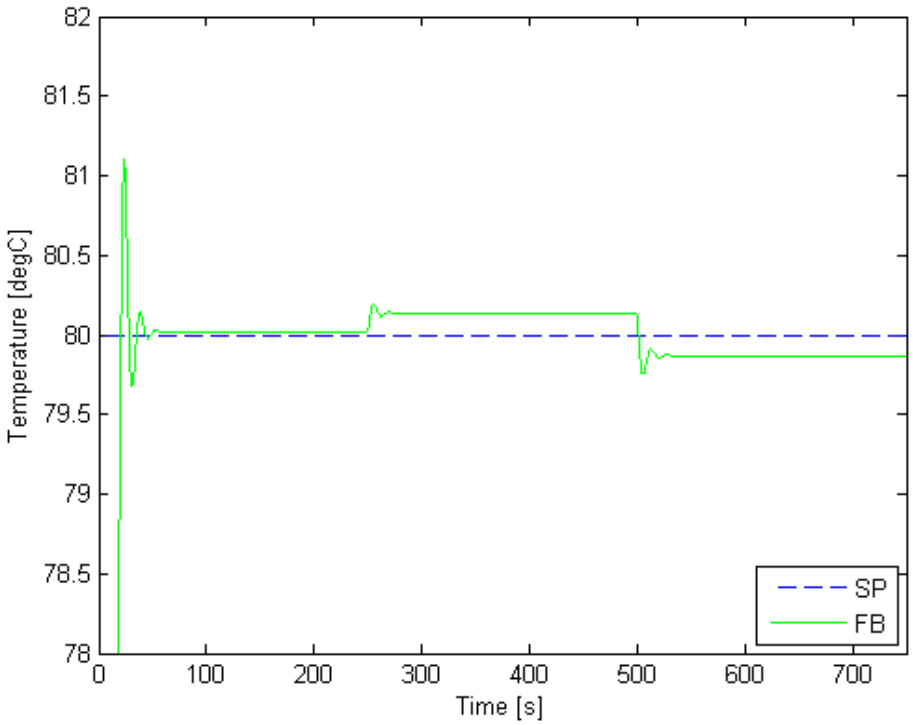

Figure 3-20 Stack Outlet Temperature: Augmented LQR Control

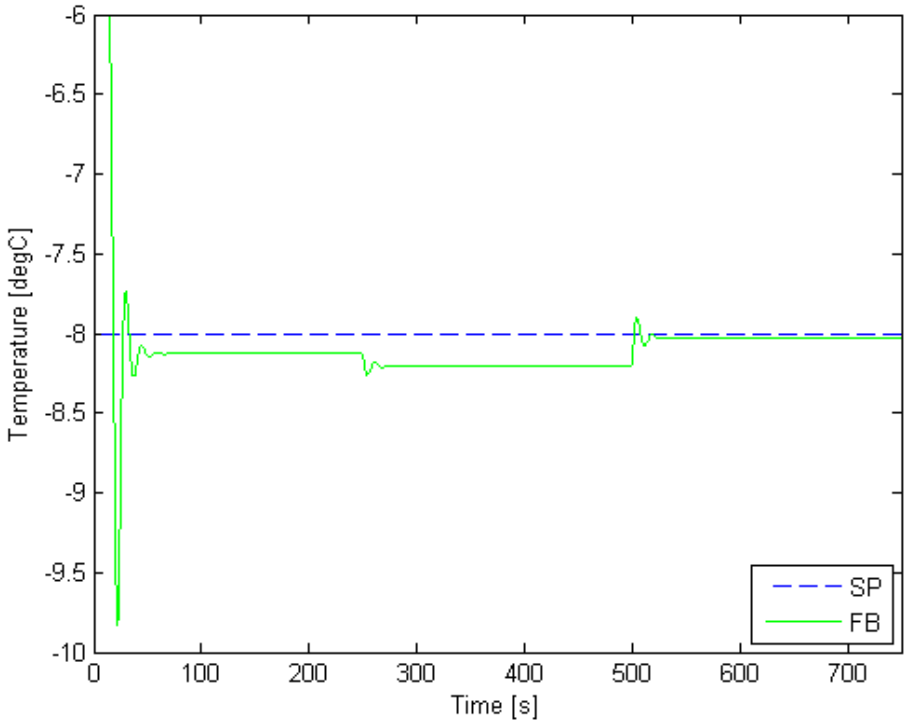

Figure 3-21 Stack ΔT: Augmented LQR Control

Controller gains were also computed for the 0.2 A/cm^2 and 1.2 A/cm^2 load cases using the same methods used in the 0.6 A/cm^2 case. The weighting matrices used can be found in Appendix B. Figures 3-22 through 3-25 show the results of the simulations for the two load cases. The 0.2 A/cm^2 case shows excellent performance in terms in stack outlet temperature, with very little steady state error. The errors in the coolant ΔT are a function of system limitations. Since the coolant pump has a minimum set point of 10% to maintain a minimum coolant flow, some of the load conditions do not generate enough heat to obtain a -8 °C delta at the minimum coolant flow. The 1.2 A/cm^2 load case also shows excellent stack outlet temperature control, but with steady state error in the stack ΔT, even with the augmented LQR controller. The offset is between 0.25 and 0.5 °C over the simulation.

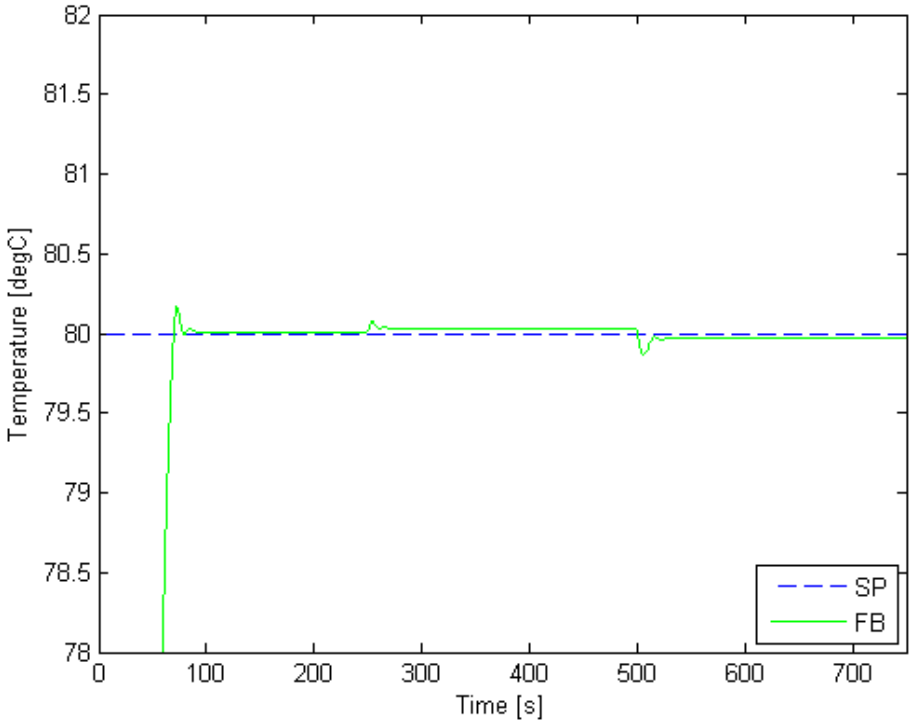

Figure 3-22 Stack Outlet Temperature: 0.2 A/cm2

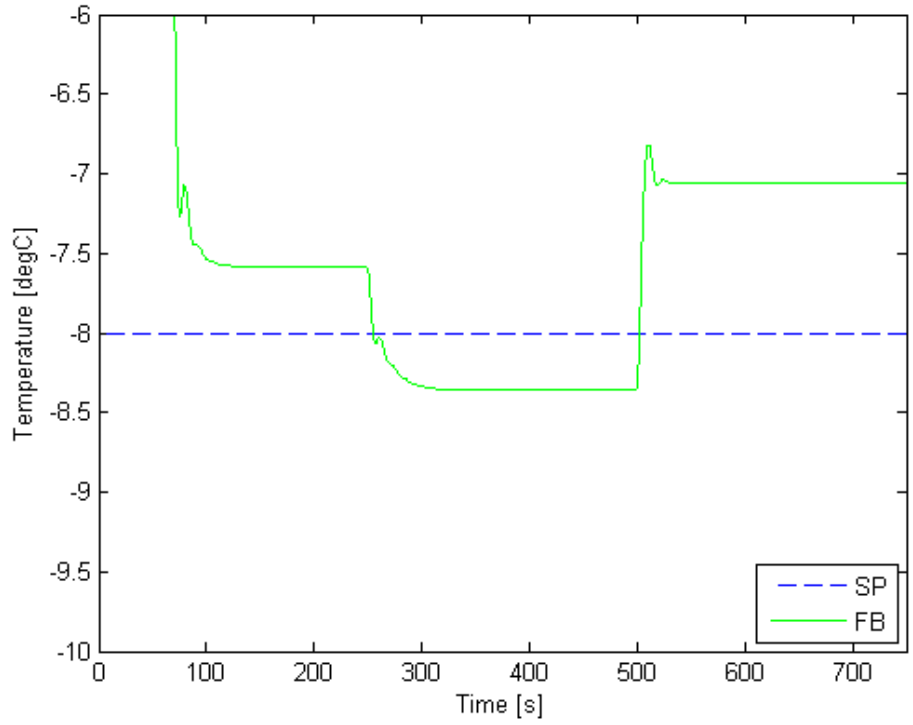

Figure 3-23 Stack delta T: 0.2 A/cm2

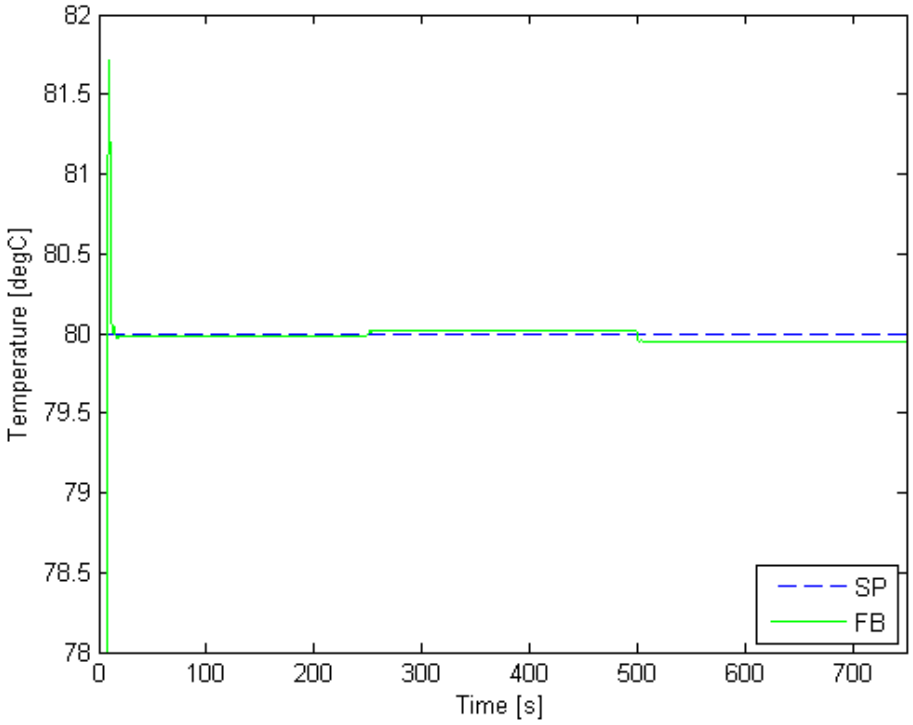

Figure 3-24 Stack Outlet Temperature: 1.2 A/cm2

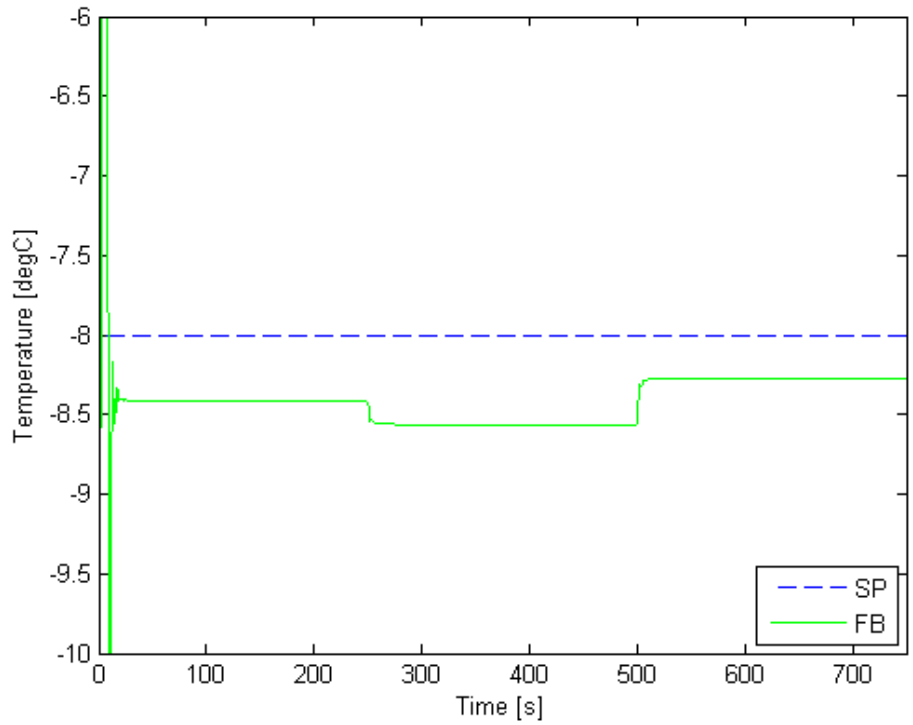

Figure 3-25 Stack delta T 1.2 A/cm2

Table 3.5 below shows a comparison of the state feedback and augmented state feedback cases using the same methodology used for Table 3.4. Augmenting the controller with the output feedback results in a 2% improvement in tracking performance with a negligible change in actuator effort.

Table 3-5 Comparison of State Feedback Controllers at 0.6 A/cm²

Case	Tracking Performance	Control Effort
State Feedback	$3.93x10^4$	$8.23x10^5$
Augmented State Feedback	$3.88x10^4$	$8.22x10^5$

The advantage of the state controller can be seen at the low power points. This is a difficult condition for a controller since minimal heat is generated by the stack and the system response is slow due to the low coolant flow. As seen in Section 3.2, the independent controllers struggle here with a lot of controller interaction. Figures 3-26 to 3-28 below show the improvement that comes from using the state feedback control.

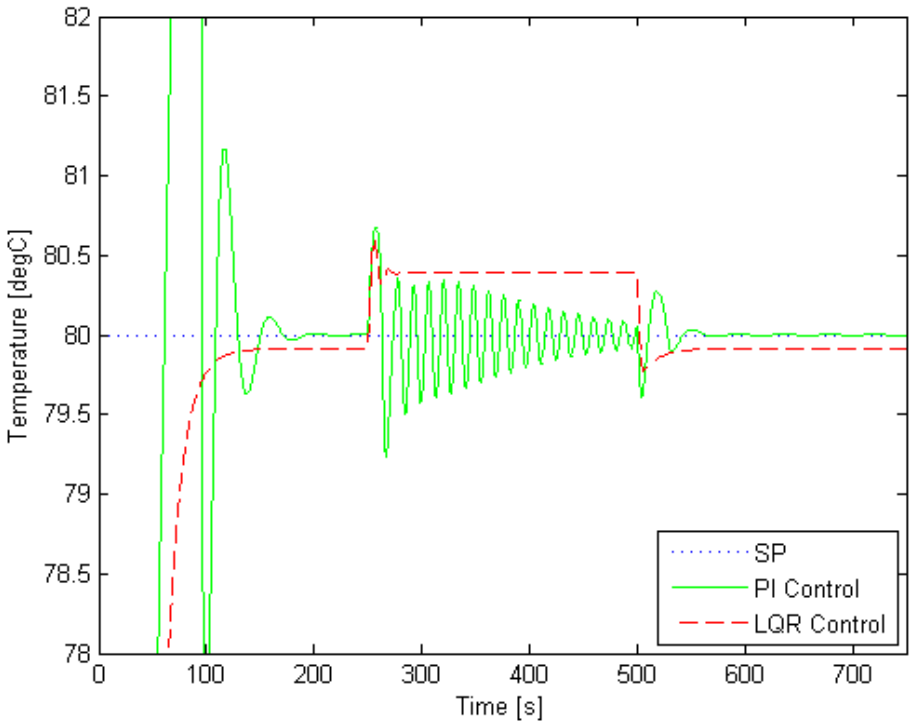

Figure 3-26 Stack Outlet Temperature Comparison

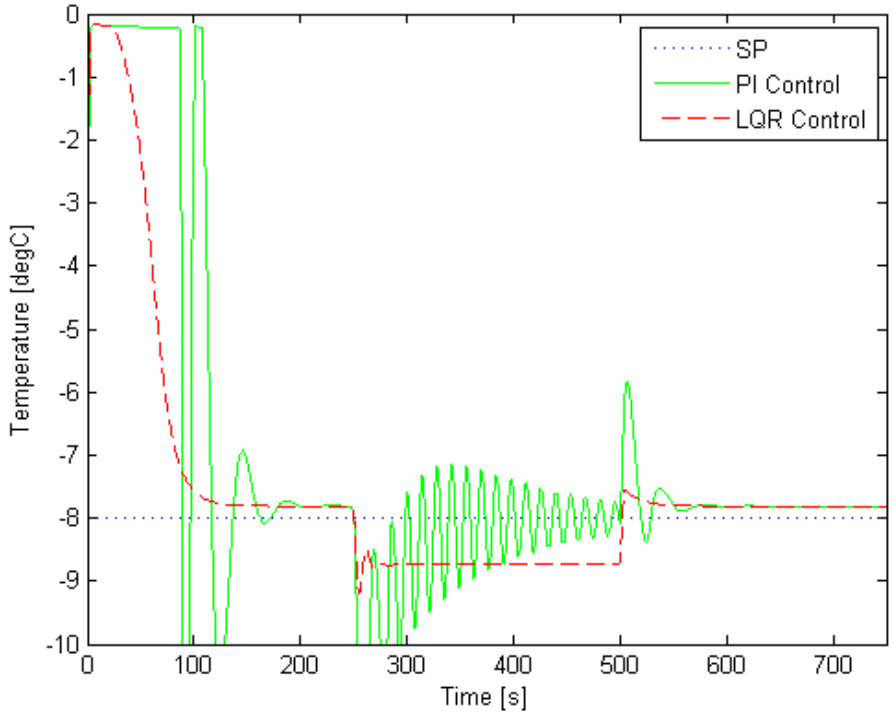

Figure 3-27 Stack ΔT Comparison

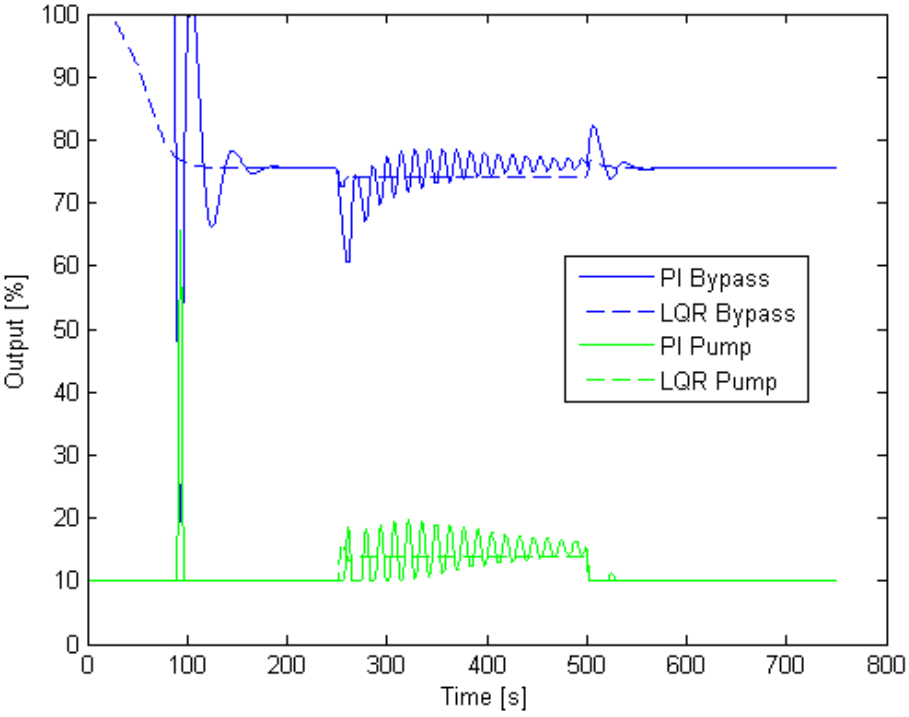

Figure 3-28 Control Effort Comparison

The interaction is partly a result of the PI gains. Since a single set of gains are used for the PI controller, the gains must be large enough to provide adequate control at the high power points, where the system responds much faster than at the low power points. With these high gains, there is a lot of interaction at the low power points. This performance can be improved by adding gain scheduling to the PI control. This would allow different gains for the different load cases. Figures 3-29 and 3-30 shows the same simulation as above with the PI controller optimized for the low power point. There is significantly less interaction between the two control variables, but the state feedback controller still shows a performance improvement over the PI controller. While there is some steady state error in the LQR response, this is a function of the state set point estimates from the linearized model. The important point is the speed of the response of the state feedback controller as compared to the PI control scheme and also the lack of controller interaction. In both of these measures, the state feedback control is superior.

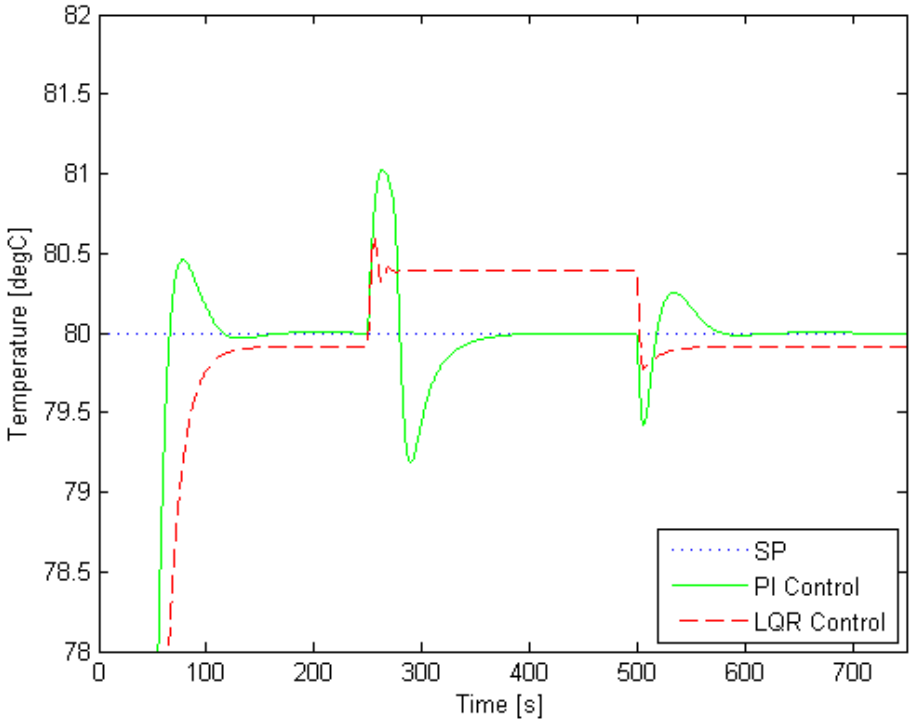

Figure 3-29 Stack Outlet Temperature: Revised PI Tuning

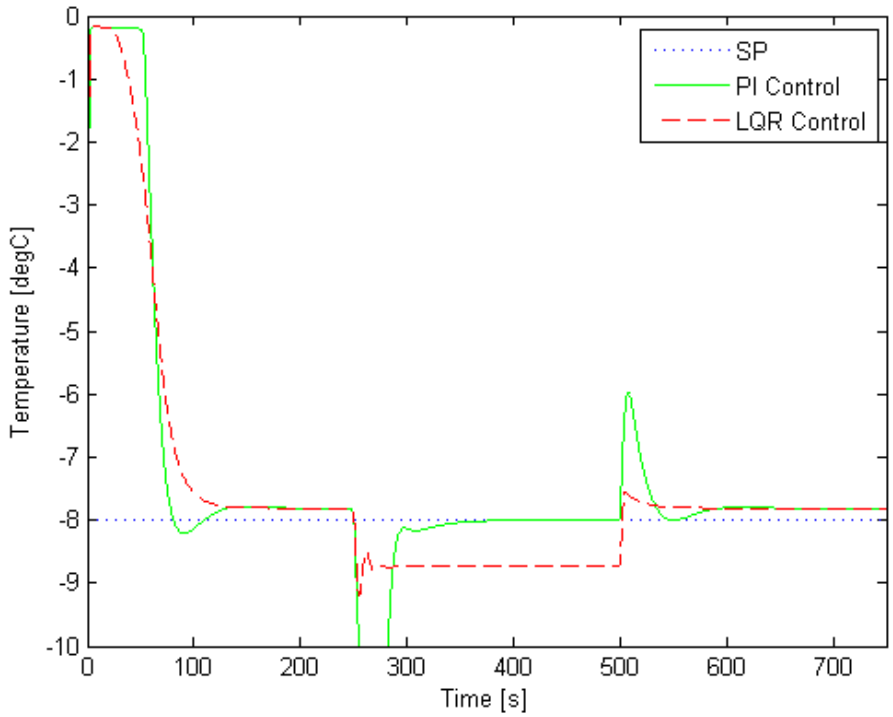

Figure 3-30 Stack delta T: Revised PI Tuning

Table 3.6 below shows the results of the simulations above tabulated using the same methodology used in Tables 3.4 and 3.5. From the table, it can be seen that even though the revised tuning of the PI controller improves the set point tracking and lowers the actuator effort when compared to the original PI controller, it is still not as good as the state feedback control. The LQR control provides 26% and 1.5% better tracking than the original and revised PI controllers, respectively.

Table 3-6 PI and LQR Controller Comparison

Case	Tracking Performance	Control Effort
PI Control	1.66×10^5	6.75×10^5
Revised PI Control	1.31×10^5	6.66×10^5
LQR Control	1.29×10^5	6.62×10^5

3.5 Estimator Design

Since only one of the states, the coolant outlet temperature, is measured, an estimator must be used to predict the other two states. An estimator takes advantage of the system models and the available measurements and predicts what the unmeasured state's values are. In this case, one of the states, the radiator coolant outlet temperature, is actually measurable. However, in a typical automotive system this is not measured to eliminate the sensor and its associated cost. The third state, the radiator wall temperature, is not easily measured and must be estimated.

The estimator used in this work is a Kalman estimator. (35) The Kalman estimator is based on a linear system of the form:

$$\dot{\bar{x}} = A\bar{x} + B\bar{u} + G\bar{w} \qquad [3.16]$$

$$\bar{y} = C\bar{x} + D\bar{u} \qquad [2.49]$$

Equation [3.16] is similar to Equation [2.48] with the addition of the $G\bar{w}$ term, where *w* is the process noise and *G* is the system gain on the process noise. For this work, *G* is assumed to zero, which neglects the effect of noise in the system. Since this work is simulation based, this is a reasonable first assumption. Before implementing this estimator in an actual system, revisiting this assumption would be warranted. The state equation of the estimator is:

$$\dot{x}_e = Ax_e + Bu + K_e(y - Cx_e - Du) \qquad [3.17]$$

where *u* and *y* are the control inputs and system outputs, respectively, of the actual system and x_e is the estimated states. Using these values and the estimator gain, K_e, estimates of the outputs and states are made. The estimator gain is found by solving the ARE:

$$\dot{P} = AP + PA^T + GQG^T - PC^TR^{-1}CP \qquad [3.18]$$

for P and taking the estimator gain to be, by definition:

$$K_e = PC^TR^{-1} \qquad [3.19]$$

Q and R in Equation [3.18] are gain matrices that can be used to tune the estimator. For this work, the gain matrices were identity. As will be seen in the following results, using the identity matrix resulted in very good state estimations, so further tuning was not needed.

The Kalman estimator is by its nature a linear estimate, since it makes use of the linear system matrices. Since different linear models are computed at the three load cases, a Kalman estimator is computed at each of the load cases as well. The following figures show the estimated states compared to the actual state values computed using the full, non-linear model at each load case. This is one advantage of using a validated system model. The value of states that are not measured in the physical system can be easily obtained from the model. This allows for a direct and easy comparison of the estimators performance. Plots of the stack coolant outlet temperature are included for completeness even though this state is measured and does not need to be estimated.

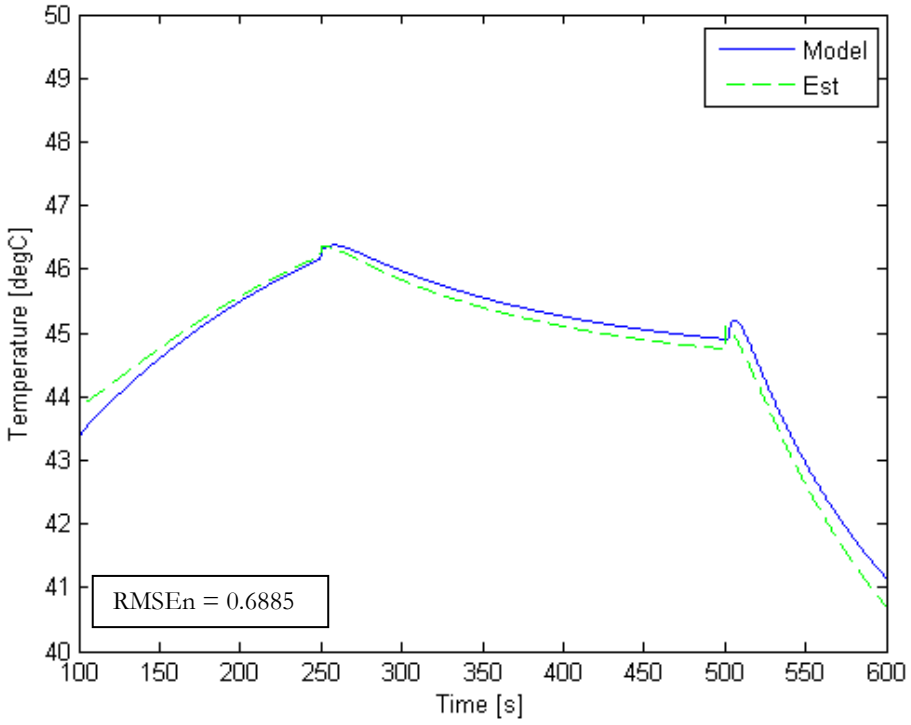

Figure 3-31 State 1: Radiator Coolant Outlet Temperature, 0.2 A/cm^2

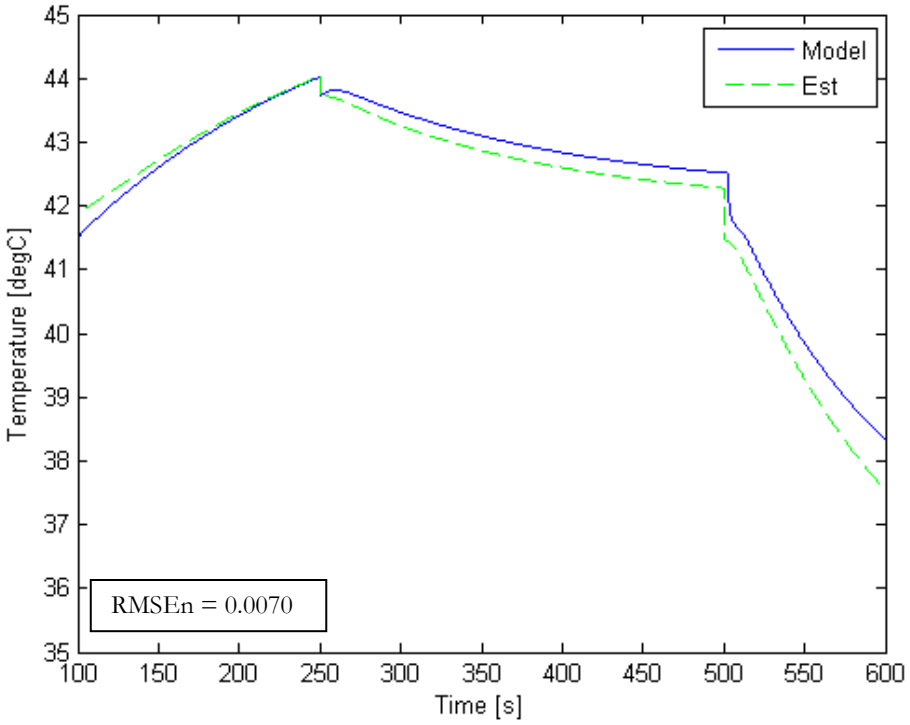

Figure 3-32 State 2: Radiator Wall Temperature, 0.2 A/cm2

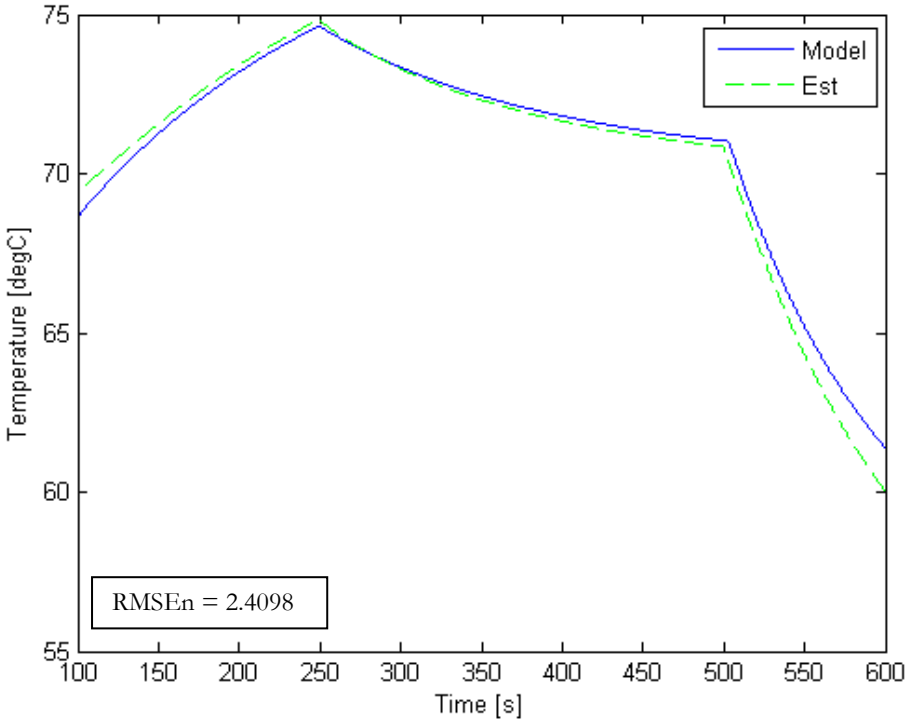

Figure 3-33 State 3: Stack Coolant Outlet Temperature, 0.2 A/cm2

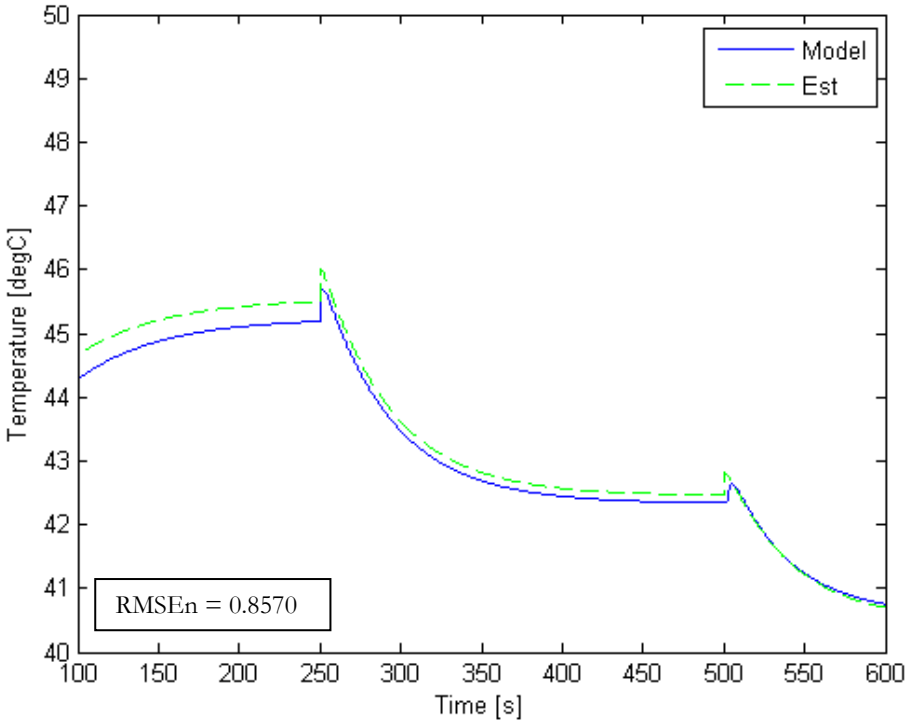

Figure 3-34 State 1: Radiator Coolant Outlet Temperature, 0.6 A/cm2

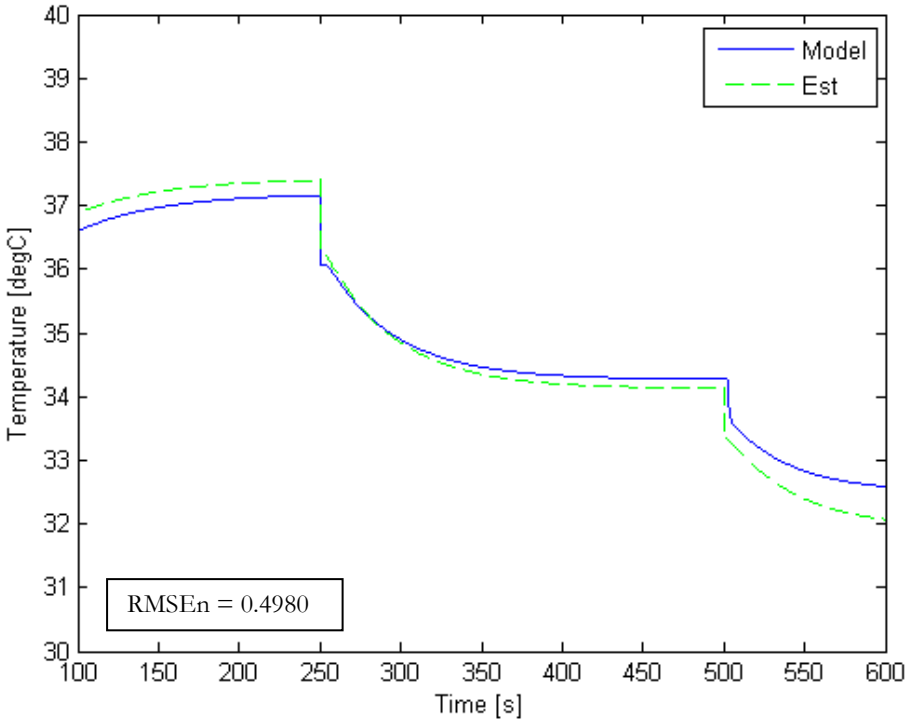

Figure 3-35 State 2: Radiator Wall Temperature, 0.6 A/cm2

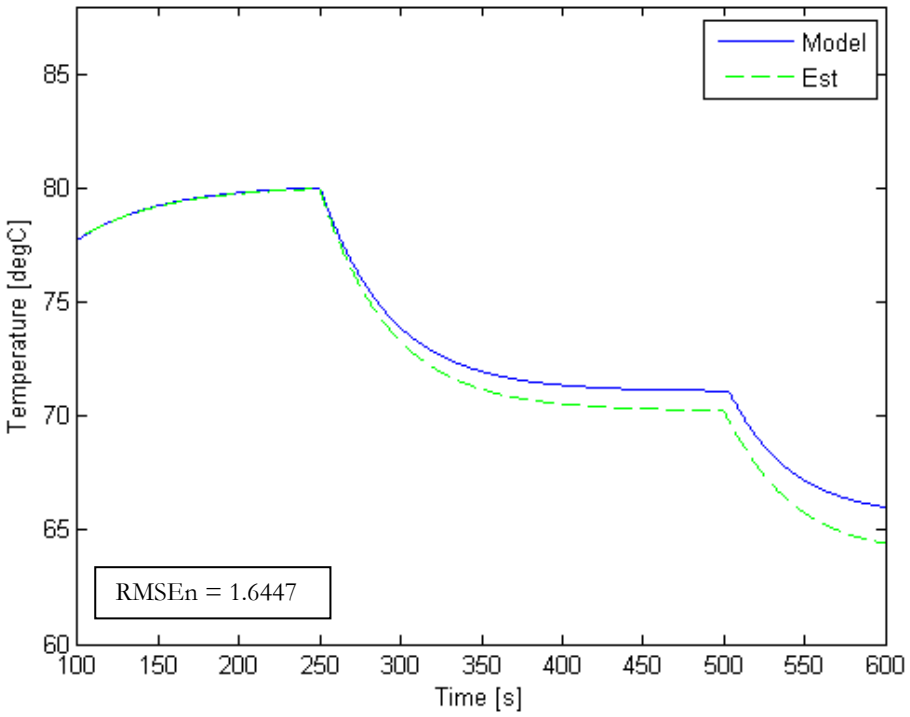

Figure 3-36 State 3: Stack Coolant Outlet Temperature, 0.6 A/cm2

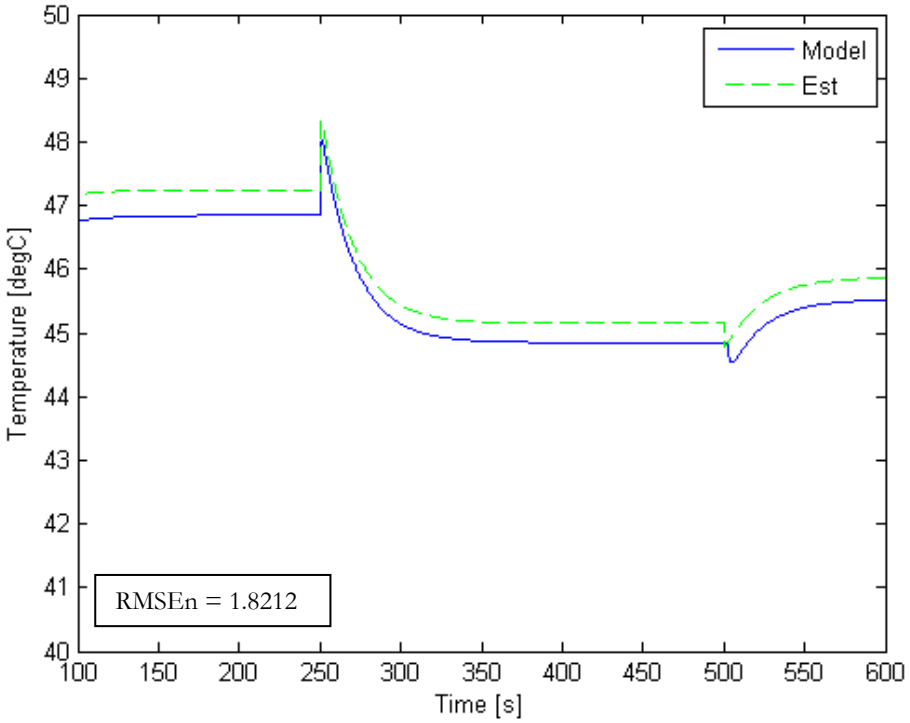

Figure 3-37 State 1: Radiator Coolant Outlet Temperature, 1.2 A/cm2

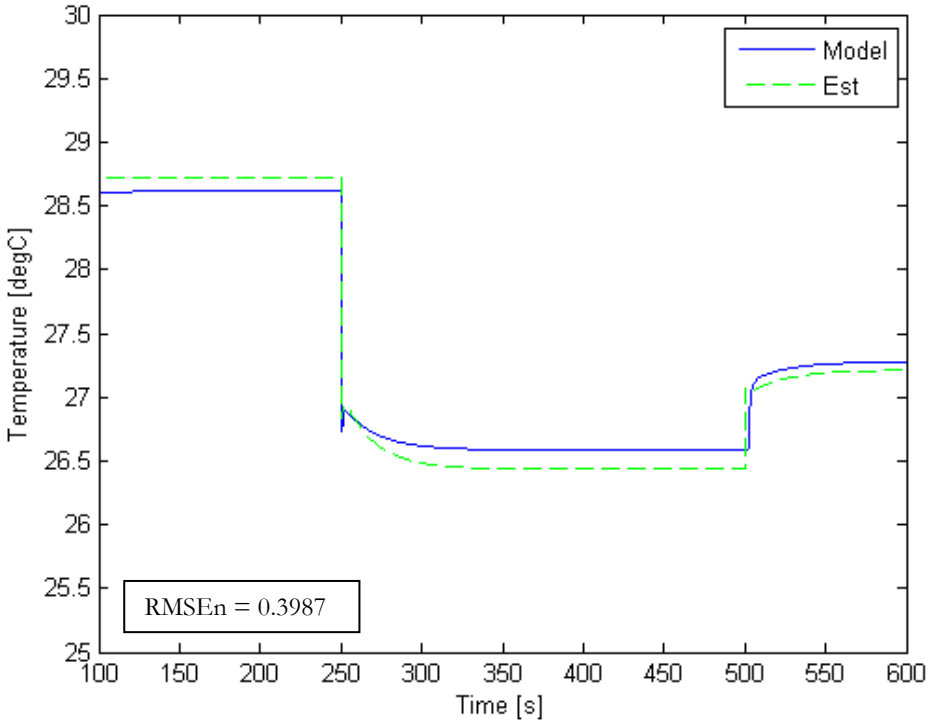

Figure 3-38 State 2: Radiator Wall Temperature, 1.2 A/cm2

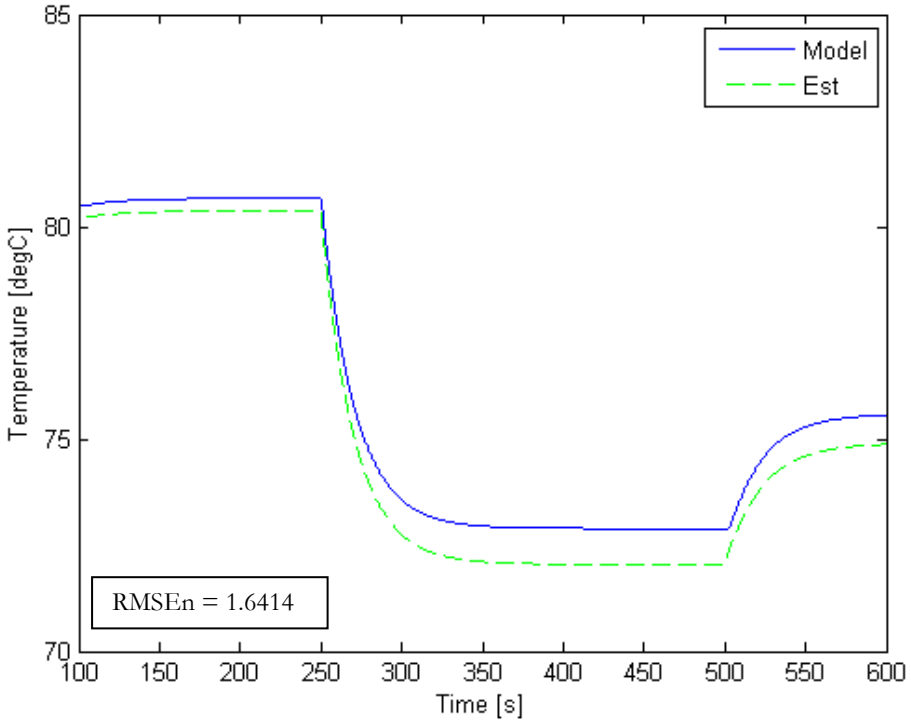

Figure 3-39 State 3: Stack Coolant Outlet Temperature, 1.2 A/cm2

Figures 3-31 through 3-39 show the estimator does a very good job of estimating the states. At the 0.6 A/cm^2 and 1.2 A/cm^2 load cases there is some steady state offset between the estimated and non-linear model values, and this is a function of using the linear models. Since the linear models are based on the reduced order non-linear system, which has error between it and the full, non-linear model, this error should be expected to appear on predictions based on these linear models.

The effect of these state estimation errors are shown in Figures 3-40 to 3-48, which show the performance of the augmented state feedback controller using both the states from the estimator and from the full, non-linear model. In general, the performance difference between the model and estimated state control is minimal. The largest differences can be seen at the 0.2 A/cm^2 load case, especially Figure 3-41 where the maximum ΔT is 1.15 °C. Figures 3-43 to 3-46 show the results for the 0.6 A/cm^2 and 1.2 A/cm^2 load cases, where the maximum difference between the responses of the two different controllers is less than 0.1 °C. This indicates the estimator does not negatively impact the augmented state feedback controller.

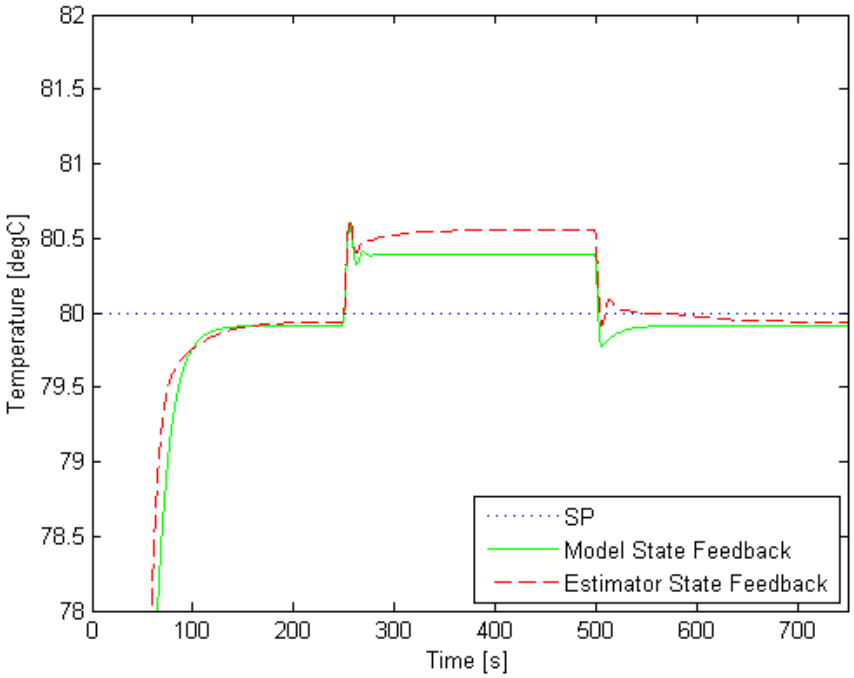

Figure 3-40 Stack Coolant Outlet Temperature: LQR Control with and without Estimator, 0.2 A/cm^2

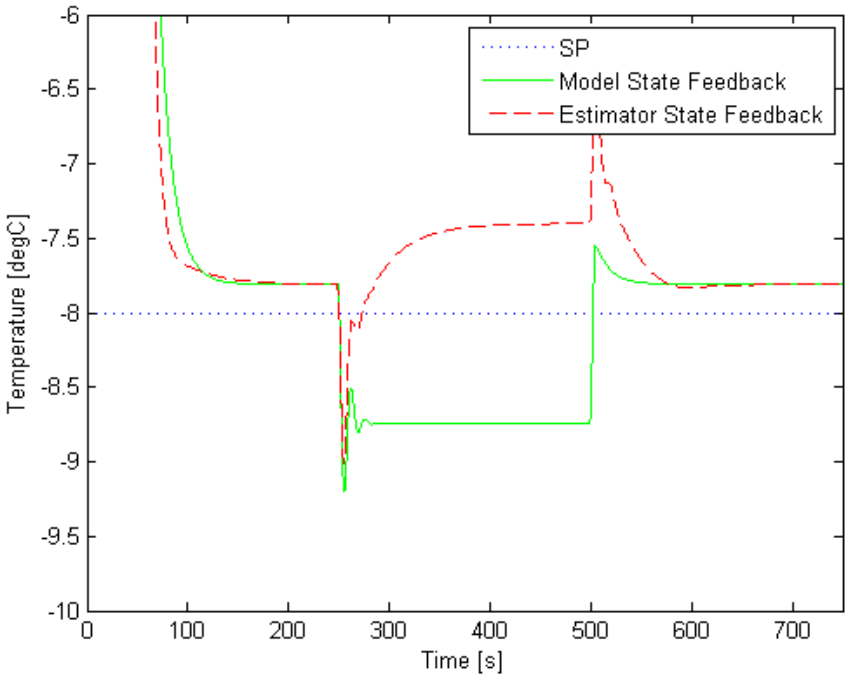

Figure 3-41 Stack Coolant ΔT: LQR Control with and without Estimator, 0.2 A/cm²

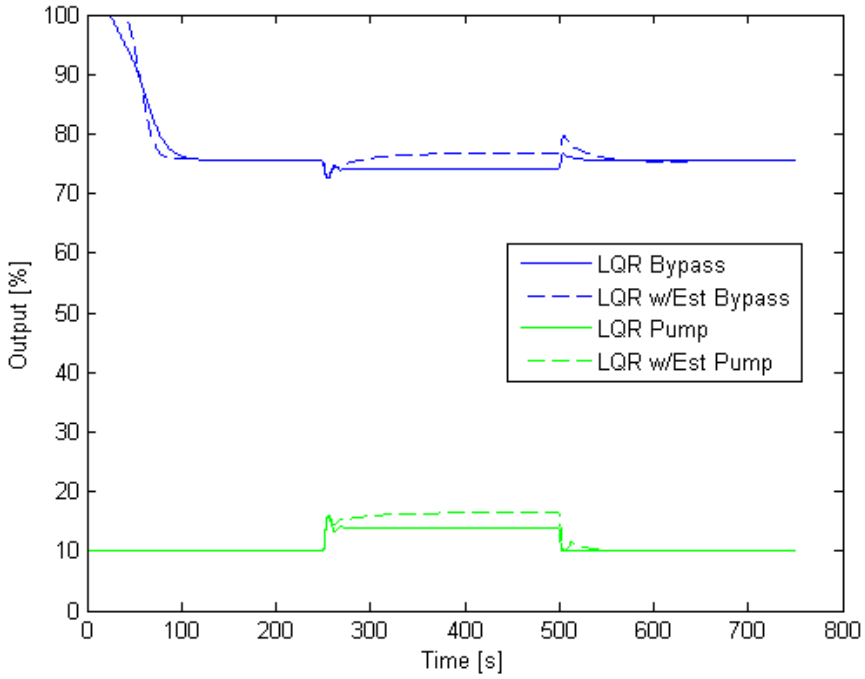

Figure 3-42 Control Effort: LQR Control with and without Estimator, 0.2 A/cm²

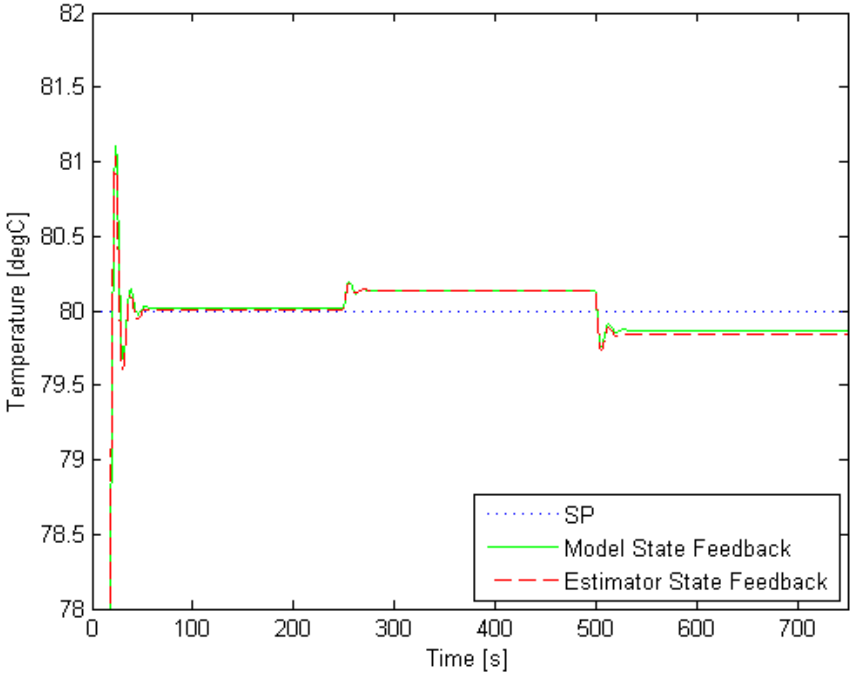

Figure 3-43 Stack Coolant Outlet Temperature: LQR Control with and without Estimator, 0.6 A/cm²

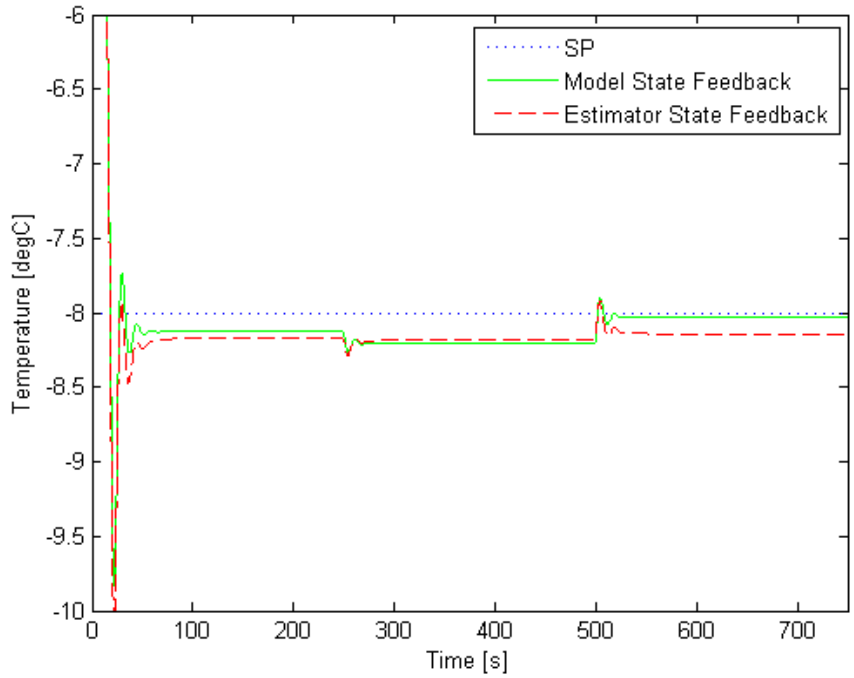

Figure 3-44 Stack Coolant ΔT: LQR Control with and without Estimator, 0.6 A/cm²

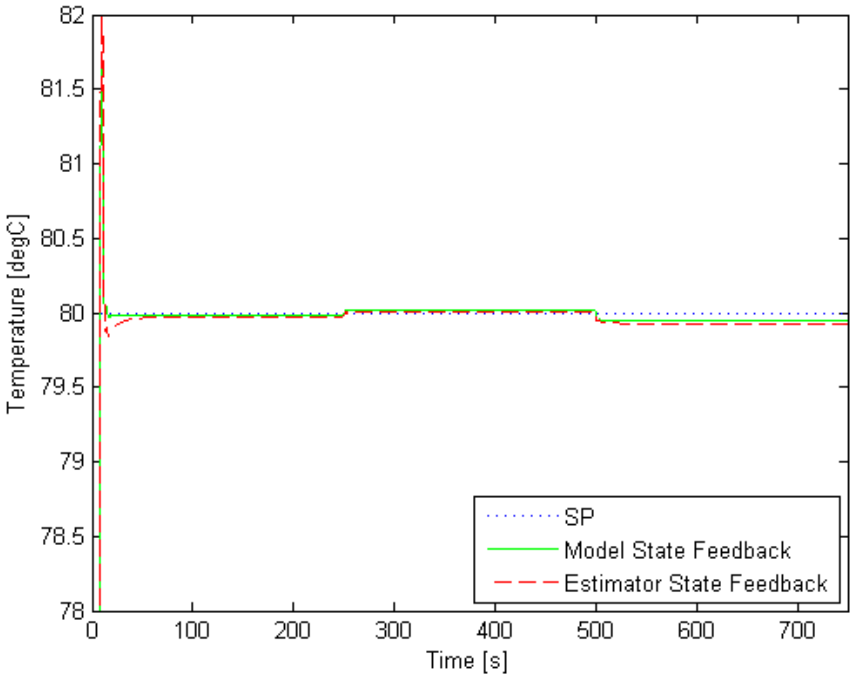

Figure 3-45 Stack Coolant Outlet Temperature: LQR Control with and without Estimator, 1.2 A/cm²

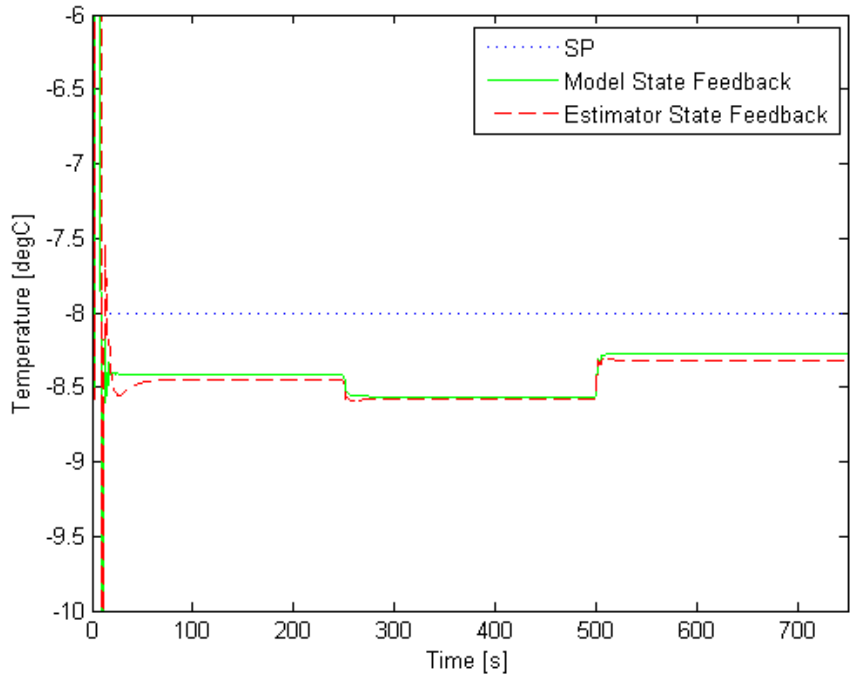

Figure 3-46 Stack Coolant ΔT: LQR Control with and without Estimator, 1.2 A/cm²

Table 3.7 presents the results of the previous simulations tabulated in the same manner as Tables 3-4 to 3-6. For the 0.2 A/cm^2, the worst case, the estimator results in a 6.2% decrease in tracking performance while increasing the actuator effort by 2%. For the 0.6 and 1.2 A/cm^2 cases, the performance decrease as a result of the estimator is 1.6% and 2.1%, respectively, with no appreciable change in actuator effort.

Table 3-7 Estimator Effect on LQR Control

Load Case	Controller	Tracking Performance	Actuator Effort
0.2 A/cm^2	LQR	$1.29x10^5$	$6.62x10^5$
	LQR w/ Est	$1.37x10^5$	$6.74x10^5$
0.6 A/cm^2	LQR	$3.88x10^4$	$8.22x10^5$
	LQR w/ Est	$3.93x10^4$	$8.20x10^5$
1.2 A/cm^2	LQR	$2.36x10^4$	$1.10x10^6$
	LQR w/ Est	$2.41x10^4$	$1.10x10^6$

Chapter 4 Conclusions and Further Work

This work has attempted to fill a gap in the published literature of a higher-order model of an automotive, PEM fuel cell thermal system. Chapter 1 developed the problem and motivation for the work. A survey of the existing literature was conducted and a need was found for a more representative system model which matched an actual fuel cell system. All of the literature reviewed used a simplified system model which neglected several components in the physical system. There was also a lack of validation of the models found in the literature against physical system data.

Chapter 2 presented the development and validation of this model. Each subsystem was modeled using first principal models where ever possible and validated using data from a physical system. An 8th order, non-linear model was developed and compared to physical system data. This model was shown to have very good agreement with the physical system, especially the stack coolant temperature delta. The frequency analysis of the full model was also conducted to gain a better understanding of the systems performance. Next, a reduced, 3rd order non-linear model was developed and compared to the full, non-linear model. This reduced order model was found to have very good transient agreement with the full model but did suffer from

steady state error. The reduced order model was then linearized at a low, mid and high power load case and again compared back to the full model.

Chapter 3 focused on the control of the fuel cell thermal system. Two different SISO control schemes were analyzed. Using the RGA technique, the optimal pairings between the input and output variables were found. It was determined that the stack coolant outlet temperature was most influenced by the bypass valve and the stack coolant temperature delta was most influenced by the coolant flow rate. Next, a single PI controller was implemented to control the stack coolant outlet temperature using the bypass valve, while the pump was controlled using a static feed forward term. Decoupled PI loops using the optimal pairings were next considered. In both cases the gains for the PI controllers were chosen using an optimization routine. It was found that the since PI control scheme with static feed forward control of the coolant pump performed better than the decoupled PI controllers, but with reduced robustness. The final control scheme considered was full-state feedback control. The gains for this control scheme were computed using the optimal LQR method. This control scheme was augmented to include output feedback as well in an effort to improve the steady-state performance. Finally, a state estimator was added to determine the values of the two unmeasured states. While the full state feedback controller showed improved performance versus the PI control schemes, it did suffer from steady state errors due to the state set points estimated from the linear model. The full state feedback controller had much less controller interaction than the PI controller, which was one of the goals of using that control schemes.

There are several areas in which this work could be expanded. One of the limiting factors to the full-state feedback controller was the state set points were determined off-line for each of the three load cases considered. The controller's performance could be improved by estimating these set points online in the controller. This would involve linearizing the reduced order model in real time. This can be computationally expensive, so work would be needed to optimize this process. This work also considered the three load cases separately for the full state feedback controller. The next step would be to simulate an entire pol curve and develop the transition methodology to switch between the different controller gains. Finally, the biggest assumption used in developing the system model was neglecting pressure changes within the system. In a typical automotive thermal system, these pressure drops can be significant, so the next revision of the model should include pressure drops for each component. This will roughly

double the number of states in the full, non-linear model, which is the reason this was not examined in this work.

Bibliography

1. *Coolant controls of a PEM fuel cell system.* **Ahn, Jong-Woo and Choe, Song-Yul.** 2007, Journal of Power Sources, Vol. 179, pp. 252-264.

2. **Larminie, James and Dicks, Andrew.** *Fuel Cell Systems Explained.* s.l. : Wiley, 2003.

3. **Kays, W M and London, A L.** *Compact Heat Exchangers.* New York : McGraw Hill, 1964.

4. *Radiator Characterization and Optimization.* **Kroger, D G.** Warrendale, PA : SAE International, 1984. 840380.

5. *Calculation and Design of Cooling Systems.* **Eichlseder, Wilfried and Raab, Gottfried.** Warrendale, PA : SAE International, 1993. 931088.

6. *Intercooler Model for Unsteady Flow in Engine Manifolds.* **Bromnick, P A, Pearson, R J and Winterbone, D E.** s.l. : Professional Engineering Publishing, 1998, Vol. 212.

7. **Jung, Dohoy and Assanis, Dennis N.** *Numerical Modeling of Cross Flow Compact Heat Exchangers with Louvered Fins using Thermal Resistance Concepts.* Warrendale, PA : SAE International, 2006. 2006-01-0726.

8. *Advances in Automotive Heat Exhcanger Technology.* **Shah, Ramesh K.** Warrendale, PA : SAE International, 2003. 2003-01-0533.

9. *Thermal Management Evolution and Controlled Coolant Flow.* **Allen, David J and Lasecki, Michael P.** Warrendale, PA : SAE International, 2001. 2001-01-1732.

10. **Melzer, Frank, et al.** *Thermomanagement.* Warrendale, PA : SAE International, 1999. 1999-01-0238.

11. **Cortona, Elena and Onder, Christopher.** *Engien Thermal Management with Electric Cooling Pump.* Warrendale, PA : SAE International, 2000. 2000-01-0965.

12. *Application of Controllable Electric Coolant Pump for Fuel Economy and Coolign Performance Improvement.* **Cho, Hoon, et al.** Anaheim : ASME, 2004. IMECE2004-61056.

13. *Advanced Engine Cooling Thermal Management System on a Dual Voltage 42V-14V Minivan.* **Chanfreau, Mattieu, et al.** Warrendale, PA : SAE International, 2001. 2001-01-1742.

14. **Fronk, Matthew H, et al.** *PEM Fuel Cell System Solutions for Transportation.* Warrendale, PA : Society of Automotive Engineers, 2000. 2000-01-0373.

15. *A Model PRedicting Transient Responses of Proton Exchange Membrane Fuel Cells.* **Amphlett, J C, et al.** 1996, Journal of Power Sources, pp. 183-188.

16. *Modeling Fuel Cell Stack Systems.* **Lee, J H and Lalk, T R.** s.l. : Journal of Power Sources, 1998, Vol. 73.

17. **Gurski, Daniel.** *Cold-start effect on performance and efficiency for vehicle fuel cell systems.* Blacksburg : Virginaia Polytechnic Institue and State University, 2002.

18. *Control Oriented Model for an Automotive PEM Fuel Cell System with Imbedded 1+1D Membrane Water Transport.* **Miotti, Alessandro, et al.**

19. *System Level Lumped-Parameter Dynamic Modeling of PEM Fuel Cell.* **Xue, X, et al.** s.l. : Journal of Power Sources, 2004, Vol. 133.

20. *A general formulation for a mathematical PEM fuel cell model.* **Baschuk, J J and Li, Xianguo.** s.l. : Journal of Power Sources, 2004, Vol. 142.

21. *Balancing Stack, Air Supply and Water/Thermal Management Demands for an Indirect Methanol PEM Fuel Cell System.* **Friedman, David J, et al.** Warrendale, PA : SAE International, 2001. 2001-01-0535.

22. *A model predicting performance of proton exchange membrane fuel cell stack thermal systems.* **Zhan, Yangjun, et al.** s.l. : Applied Thermal Engineering, 2004, Vol. 24.

23. *Thermal Dynamic Modeling and Nonlinear Control of a PEM Fuel Cell Stack.* **Kolodziej, Jason.** s.l. : ASME, 2007, Journal of Fuel Cell Science and Technology, Vol. 4.

24. **Mays, D Craig, et al.** *Control System Development for Automotive PEM Fuel Cell Vehicles.* Warrendale, PA : SAE International, 2001. 2001-01-2548.

25. **Pukrushpan, Jay T, Stefanopoulou, Anna G and Peng, Huei.** *Control of Fuel Cell Power Systems.* London : Springer, 2004.

26. **Bhat, Nikhil, et al.** *Adaptive Control of an Externally Controlled Engine Cooling Fan-Drive.* Warrendale, PA : SAE International, 2006. 2006-01-1036.

27. **Wendeker, Miroslaw, et al.** *Adaptive Airflow Control of the PEM Fuel Cell System.* Warrendale, PA : SAE International, 2007. 2007-01-2012.

28. *Modle-based Control of Fuel Cells: (1) Regulatory Control.* **Golbert, Joshua and Lewin, Daniel R.** s.l. : Journal of Power Sources, 2004, Vol. 135, pp. 135-151.

29. *System Design for Vehicle Applications: GM/Opel.* **Masten, D A and Bosco, A D.** 3, Chichester : John Wiley & Sons, 2003, Vol. 4.

30. **General Motors Co.** GM Fuel Cell Vehicles. [Online] http://www.chevrolet.com/experience/fuel-solutions/fuel-cell/.

31. **Front, Matthew H, et al.** *PEM Fuel Cell System Solutions for Transportation.* Detroit : Society of Automotive Engineers, 2000.

32. **Seborg, Dale E, Edgar, Thomas F and Mellichamp, Duncan A.** *Process Dynamics and Control.* New York : Wiley, 1989.

33. **Incropera, Frank P and DeWitt, David P.** *Fundamentals of Heat and Mass Transfer.* New York : Wiley, 2002.

34. **Lewis, Frank L.** *Optimal Control.* New York : Wiley, 1986.

35. —. *Optimal Estimation.* New York : John Wiley & Sons, 1986.

36. *Mathematical Modeling of Proton Exchange Membrane Fuel Cell Stacks.* **Thirumalai, Dwanwa and White, Ralph E.** 5, s.l. : Journal of the Electrochemical Society, 1997, Vol. 144.

37. *An Integrated SOFC Plant Dynamic Model for Power System Simulations.* **Padulles, J, Ault, G W and McDonald, J R.** s.l. : Journal of Power Sources, 2000, Vol. 86.

38. *System level lumped-parameter dynamic modeling of PEM fuel cell.* **Xue, X, et al.** s.l. : Journal of Power Sources, 2004, Vol. 133.

39. *Analysis of the water and thermal management in proton exchange membrane fuel cell systems.* **Bao, Cheng, Ouyang, Minggao and Yi, Baolian.** 2006, International Journal of Hydrogen Energy, Vol. 31, pp. 1040-1057.

40. **Franklin, Gene F, Powell, J David and Workman, M L.** *Digital Control of Dynamic Systems.* s.l. : Addison-Wesley, 1992.

Appendix A – Linearized Models

Load Case 1: 0.2 A/cm^2

$$A = \begin{bmatrix} -2.887 & 2.691 & 0.196 \\ 6.294 & -6.294 & -0.262 \\ 0.010 & 0 & -0.010 \end{bmatrix}$$

$$B = \begin{bmatrix} -0.266 & 0.636 \\ 0.609 & -1.462 \\ 0.014 & -0.036 \end{bmatrix}$$

$$C = \begin{bmatrix} 0 & 0 & 1 \\ 0.24 & 0 & -0.24 \end{bmatrix}$$

$$D = \begin{bmatrix} 0 & 0 \\ 0.325 & 0 \end{bmatrix}$$

Load Case 1: 0.6 A/cm^2

$$A = \begin{bmatrix} -3.311 & 2.691 & 0.620 \\ 6.294 & -6.294 & -0.918 \\ 0.033 & 0 & -0.033 \end{bmatrix}$$

$$B = \begin{bmatrix} -0.954 & 0.665 \\ 2.082 & -1.451 \\ 0.050 & -0.035 \end{bmatrix}$$

$$C = \begin{bmatrix} 0 & 0 & 1 \\ 0.23 & 0 & -0.23 \end{bmatrix}$$

$$D = \begin{bmatrix} 0 & 0 \\ 0.354 & 0 \end{bmatrix}$$

Load Case 1: 1.2 A/cm^2

$$A = \begin{bmatrix} -4.202 & 2.691 & 1.511 \\ 6.294 & -6.294 & -2.131 \\ 0.080 & 0 & -0.080 \end{bmatrix}$$

$$B = \begin{bmatrix} -1.98 & 0.671 \\ 3.795 & -1.282 \\ 0.105 & -0.035 \end{bmatrix}$$

$$C = \begin{bmatrix} 0 & 0 & 1 \\ 0.25 & 0 & -0.25 \end{bmatrix}$$

$$D = \begin{bmatrix} 0 & 0 \\ 0.328 & 0 \end{bmatrix}$$

Appendix B – Weighting Gains

Load Case 1: 0.2 A/cm^2

$$Q_x = \begin{bmatrix} 15 & 0 \\ 0 & 25 \end{bmatrix} Q_y = \begin{bmatrix} 5 & 0 \\ 0 & 10 \end{bmatrix} \; R = \begin{bmatrix} 1 & 0 \\ 0 & 1 \end{bmatrix}$$

Load Case 2: 0.6 A/cm^2

$$Q_x = \begin{bmatrix} 15 & 0 \\ 0 & 25 \end{bmatrix} Q_y = \begin{bmatrix} 10 & 0 \\ 0 & 5 \end{bmatrix} \; R = \begin{bmatrix} 5 & 0 \\ 0 & 0.5 \end{bmatrix}$$

Load Case 3: 1.2 A/cm^2

$$Q_x = \begin{bmatrix} 5 & 0 \\ 0 & 15 \end{bmatrix} Q_y = \begin{bmatrix} 5 & 0 \\ 0 & 10 \end{bmatrix} \; R = \begin{bmatrix} 1 & 0 \\ 0 & 1 \end{bmatrix}$$